

ALMA MATER STUDIORUM · UNIVERSITÀ DI
BOLOGNA

SCUOLA DI SCIENZE
Dipartimento di Fisica e Astronomia
Corso di Laurea in Astrofisica e Cosmologia

**STRUCTURE FORMATION
SIMULATIONS WITH SCATTERING
BETWEEN DARK ENERGY AND
BARYONS**

Relatore:
Prof. Marco Baldi

Candidato:
Fulvio Ferlito

Sessione I
Anno Accademico 2020/2021

Abstract

Our Universe is full of unknowns, among them one of the most mysterious is, no doubt, dark energy (DE), the entity responsible for cosmic acceleration. We still do not even know its intrinsic nature, and in investigating its properties we can not exclude the possibility of an interaction between DE and the other components of the Universe.

In recent times, a new class of interacting DE models have been proposed in the literature. These assume that the interaction between DE and matter could be well approximated by a pure momentum exchange between the two components. The efficiency of the process is then described by the interaction cross section.

These models have been investigated by means of N-body simulations in the case of scattering between DE and dark matter, discovering that the nonlinear effects can be more significant than the linear ones. More recently such scenario has been extended to a scattering between DE and baryons, asking whether it would be possible to detect its effects through direct cosmological observations. A linear analysis lead to the conclusion that, even for extremely large values of the interaction cross section, the impact of DE-baryon scattering on the CMB temperature power spectrum and the matter power spectrum would be undetectable, at least on linear scales.

Therefore, the only yet unexplored field that leaves an opportunity to put cosmological constraints on such interaction remains the nonlinear regime of structure formation, which can be properly studied only through N-body numerical simulations. In this work we modify the `GADGET-3` code in order to perform, for the first time in the literature, structure formation multi-particle simulations which implement DE-baryon scattering.

We focus on the effects of such interaction on major cosmological observables: the power spectrum, the halo mass function, the halo density profiles and the halo baryon fraction profiles. We find that the nonlinear effects of DE-baryon scattering can significantly affect these observables, thus paving the way to the future constraining of this interaction by means of cosmological observations.

Sommario

Il nostro Universo è pieno di incognite, tra le più misteriose vi è senza dubbio l'energia oscura (dark energy o DE), l'entità responsabile dell'accelerazione cosmica. La sua natura intrinseca ci è ancora sconosciuta e nell'investigarne le proprietà non possiamo escludere la possibilità di un'interazione tra la DE e le altre componenti dell'Universo.

In tempi recenti, è stata proposta nella letteratura una nuova classe di modelli di DE interagente. Tali modelli assumono che l'interazione tra DE e materia possa essere ben approssimata dall'esclusivo scambio di impulso tra le due componenti. In tal caso si ha che l'efficienza di tale processo di scattering è descritta dalla sezione d'urto.

Questi modelli sono stati investigati tramite simulazioni a N-corpi nel caso dello scattering tra DE e materia oscura, scoprendo che gli effetti nonlineari possono essere più significativi di quelli lineari. Più recentemente tale scenario è stato esteso allo scattering tra DE e barioni (DE-baryon scattering), con l'obiettivo di scoprire se sia possibile rilevare tale interazione per mezzo di osservazioni cosmologiche. Un'analisi lineare ha portato alla conclusione che, anche per valori estremamente alti della sezione d'urto, l'impatto del DE-baryon scattering sarebbe comunque impossibile da rilevare nello spettro angolare della radiazione cosmica di fondo e nello spettro di potenza delle fluttuazioni di densità della materia, almeno su scale lineari.

Si ha dunque che l'unico campo, tuttora inesplorato, che potrebbe permetterci di porre vincoli cosmologici su tale interazione è il regime nonlineare della formazione delle strutture cosmiche, questo può essere opportunamente studiato solo per mezzo di simulazioni a N-corpi. Nel presente lavoro di tesi modifichiamo il codice `GADGET-3` al fine di eseguire, per la prima volta nella letteratura, simulazioni cosmologiche multiparticellari che implementano lo scattering tra DE e barioni.

Poniamo la nostra attenzione sugli effetti che tale interazione ha sulle principali osservabili cosmologiche: lo spettro di potenza, la funzione di massa degli aloni nonché i profili di densità e di frazione barionica di questi. Dalla nostra analisi emerge che gli effetti nonlineari del DE-baryon scattering possono alterare in modo significativo queste osservabili, aprendo dunque la strada a futuri vincoli che sarà possibile porre per mezzo di osservazioni cosmologiche.

Contents

1	Introduction	1
1.1	Fundamentals of Modern Cosmology	1
1.1.1	Cosmological Principle and Friedmann Equations	1
1.1.2	Different Energy Components of the Universe	4
1.1.3	Redshift and Cosmic Distances	4
1.1.4	Observational Evidence of Dark Energy	6
1.1.5	Cosmological Constant and the Λ CDM Model	10
1.2	Problems of the Λ CDM Model	12
1.2.1	The Fine Tuning Problem	12
1.2.2	The Coincidence Problem	13
1.2.3	The Hubble and the σ_8 Tension	14
1.3	Cosmological Perturbation Theory	14
1.3.1	Perturbing the Einstein Equation	15
1.3.2	Equations for a Single Fluid	16
1.3.3	Evolution of Perturbations	17
2	Cosmological Observables	21
2.1	Power Spectrum	21
2.2	Mass Function	24
2.3	Halo Profiles	26
3	Dark Energy	29
3.1	Quintessence	29
3.2	Coupled Quintessence	31
3.2.1	Background Evolution	31
3.2.2	Linear Perturbations	32
3.2.3	Consequences of Coupling	34
3.3	Dark Scattering	34
3.3.1	Linear Perturbations	36
3.3.2	Dark Scattering Simulations	37
3.4	DE-Baryon Scattering	38
3.4.1	Linear Perturbations	38
3.4.2	Screening the Interaction at Small Scales	41

4	Numerical Implementation	43
4.1	The GADGET Code	43
4.1.1	Collisionless Dynamics	43
4.1.2	The Tree Algorithm	44
4.1.3	The Particle Mesh (PM) Method	45
4.1.4	The TreePM Algorithm	46
4.1.5	Parallelization strategies	49
4.2	Implementation of DE-Baryon Scattering	49
4.2.1	Constant Terms	50
4.2.2	Time dependent Terms	50
4.2.3	Updating the Acceleration	51
4.2.4	A Note on Efficiency	51
4.3	The Simulations	51
4.3.1	Initial Conditions and Cosmological Setup	51
4.3.2	Main Features	52
4.3.3	Computational Resources	53
5	Analysis of the Simulations	55
5.1	Large Scale Density Distribution	55
5.2	Power Spectrum	57
5.3	Halo Mass Function	62
5.4	Halo Profiles	65
5.5	Halo Baryon Fraction	69
6	Conclusions and Future Prospects	73
6.1	Cosmological Background	73
6.2	Our Work and Results	75
6.3	Future Prospects	77

Chapter 1

Introduction

1.1 Fundamentals of Modern Cosmology

Cosmology is the branch of physics that investigates the properties and the evolution of the Universe as a whole. The starting point of modern cosmology is Einstein's General Relativity, that together with the Cosmological Principle, leads us to the Friedmann equations. These allow to describe the expansion of the Universe over time in terms of its intrinsic curvature and its components, modeled as perfect fluids. In this chapter we are going to derive the Friedmann equations, describe the different components making up our Universe according to the Standard Model of Cosmology and then explain the most crucial open questions of such model.

1.1.1 Cosmological Principle and Friedmann Equations

The Cosmological Principle states the following:

The Universe is homogeneous and isotropic at sufficiently large scales.

It is supported by different observations, the most important concerning the photons of the Cosmic Microwave Background (CMB), which reach us from every direction with pretty much the same temperature.

On the other hand, at sufficiently large scales, the only force that governs the Universe is gravity, which is described by Einstein's General Relativity (GR) [1] in terms of spacetime geometry. Since we want the Cosmological Principle to hold, we consider the line-element of a 4-dimensional homogeneous and isotropic spacetime, which is called Friedmann–Lemaître–Robertson–Walker (FLRW) spacetime and is given by:

$$ds^2 = g_{\mu\nu} dx^\mu dx^\nu = -c^2 dt^2 + a^2(t) d\sigma^2. \quad (1.1)$$

In the above equation, some very important quantities have been introduced:

- $g_{\mu\nu}$ is the *metric tensor*, which determines all the geometrical properties of the spacetime described by the system of coordinates x^μ .
- $a(t)$ is the *scale factor*, a parameter with the dimensions of a length used to account for the expansion of the Universe. In practice $a(t)$ modulates the physical distances between objects as the Universe evolves. It is conventional to set its present day value to $a_0 = 1$.
- $d\sigma$ is the time-independent metric of the 3-dimensional space

$$d\sigma^2 = \gamma_{ij} dx^i dx^j = \frac{dr^2}{1 - Kr^2} + r^2(d\theta^2 + \sin^2\theta d\phi^2). \quad (1.2)$$

In the previous equation K is the *curvature constant*, describing the intrinsic geometry of the Universe: $K = +1, -1, 0$ corresponds respectively to *closed*, *open* and *flat* geometries.

We stress that we are following Einstein's notation, according to which we are summing over the terms with the same upper and lower indices. The Greek indices μ and ν run from 0 to 3, while the Latin indices i and j run from 1 to 3. Once we defined our metric, we want to find the dynamical equations of motion, i.e. the equations that describe the time evolution of the only dynamical quantity appearing in the metric: the scale factor $a(t)$. This is when GR comes into play. We start by calculating the Christoffel symbols from the metric tensor $g_{\mu\nu}$:

$$\Gamma_{\nu\lambda}^\mu = \frac{1}{2}g^{\mu\alpha}(g_{\alpha\nu,\lambda} + g_{\alpha\lambda,\nu} - g_{\nu\lambda,\alpha}), \quad (1.3)$$

where $g_{\alpha\nu,\lambda} \equiv \partial g_{\alpha\nu}/\partial x^\lambda$. From the Christoffel symbols we can then calculate the Ricci tensor:

$$R_{\mu\nu} = \Gamma_{\mu\nu,\alpha}^\alpha - \Gamma_{\mu\alpha,\nu}^\alpha + \Gamma_{\mu\nu}^\alpha \Gamma_{\alpha\beta}^\beta - \Gamma_{\mu\beta}^\alpha \Gamma_{\alpha\nu}^\beta. \quad (1.4)$$

The contraction of this tensor, gives the Ricci scalar:

$$R = g^{\mu\nu} R_{\mu\nu}. \quad (1.5)$$

We can now write the Einstein equations, in units where¹ $c = 1$, whose solution will describe the cosmological dynamics we are looking for:

$$G_{\mu\nu} \equiv R_{\mu\nu} - \frac{1}{2}g_{\mu\nu}R = 8\pi GT_{\mu\nu}, \quad (1.6)$$

where $G_{\mu\nu}$ is the so-called Einstein tensor and T_ν^μ is the energy-momentum tensor. In the FLRW spacetime, T_ν^μ takes the perfect fluid form:

$$T_\nu^\mu = (\rho + P)u^\mu u_\nu + P\delta_\nu^\mu, \quad (1.7)$$

¹From now on we will work in a unit system in which $c = 1$.

where δ_ν^μ is the Kronecker delta, $u^\mu = (-1, 0, 0, 0)$ is the four-velocity in comoving coordinates and ρ and P are the energy and pressure densities, respectively, since the (00) and (ij) components of T_ν^μ are $T_0^0 = -\rho$ and $T_j^i = P\delta_j^i$.

We now define one fundamental quantity of cosmology, the *Hubble parameter* (the overdot represents the derivative with respect to t):

$$H \equiv \frac{\dot{a}}{a}. \quad (1.8)$$

It describes the rate at which the Universe is expanding at a certain cosmic time, and is typically expressed in units of km/s/Mpc. Its present value is estimated to be around $H_0 \approx 65$ km/s/Mpc, thus indicating an expansion, but, as we are going to see in section 1.2.3, it is characterized by some uncertainty and it is therefore conventional to take this into account by defining the dimensionless parameter $h \equiv H_0/(100 \text{ km/s/Mpc})$.

Coming back to our calculations we find that the non-vanishing Christoffel symbols in the FLRW spacetime lead us to the following equations for the Einstein tensor:

$$G_i^0 = G_0^i = 0, \quad (1.9)$$

$$G_j^i = -(3H^2 + 2\dot{H} + K/a^2)\delta_j^i, \quad (1.10)$$

$$G_0^0 = -3(H^2 + K/a^2), \quad (1.11)$$

where we used the relation $G_\nu^\mu = g^{\mu\alpha}G_{\alpha\nu}$. We then consider the (00) and (ij) components of the Einstein tensor given by (1.11) and (1.10) to obtain the two equations that completely describe the dynamics of a homogeneous and isotropic Universe, known as the Friedmann equations:

$$H^2 = \frac{8\pi G}{3}\rho - \frac{K}{a^2}, \quad (1.12)$$

$$3H^2 + 2\dot{H} = -8\pi GP - \frac{K}{a^2}. \quad (1.13)$$

Using the first equation, the second can be rewritten as:

$$\frac{\ddot{a}}{a} = -\frac{4\pi G}{3}(\rho + 3P). \quad (1.14)$$

Combining the equations (1.12) and (1.14) and differentiating, we get the continuity equation:

$$\dot{\rho} + 3H(\rho + P) = 0. \quad (1.15)$$

This can also be obtained by applying the Bianchi identities to the Einstein equation, which leads to a null covariant derivative² of the energy-momentum tensor:

²Given a vector V^ν , its *covariant derivative* is defined as $\nabla_\mu V^\nu = \partial_\mu V^\nu + \Gamma_{\mu\lambda}^\nu V^\lambda$. It is the sum of two terms: $\partial_\mu V^\nu$ is the partial derivative, while $\Gamma_{\mu\lambda}^\nu V^\lambda$ is a correction term which accounts for how the coordinates are changing. This definition can be easily extended to act on a general tensor of rank (m, n) . The covariant derivative has the remarkable property of transforming like a tensor.

$$\nabla_\mu T_\nu^\mu \equiv T_{\nu;\mu}^\mu = 0.$$

1.1.2 Different Energy Components of the Universe

The homogeneous Universe we are describing is made up of different components, and each one of them can be modeled as a perfect fluid, with its distinctive equation of state:

$$w \equiv \frac{P}{\rho}. \quad (1.16)$$

If we want to describe the evolution of a multi-component Universe, we must consider the contribution of every single component, the Friedmann equations then become:

$$H^2 = \frac{8\pi G}{3} \sum \rho_i - \frac{K}{a^2}, \quad (1.17)$$

$$\frac{\ddot{a}}{a} = -\frac{4\pi G}{3} \sum (\rho_i + 3P_i). \quad (1.18)$$

Moreover, we can combine equations (1.12) and (1.15) to get the density evolution of a single component as a function of the scale factor or time in the case a flat Universe is dominated by a single component:

$$\rho \propto a^{-3(1+w)}, \quad a \propto (t - t_i)^{\frac{2}{3(1+w)}}. \quad (1.19)$$

Since P and ρ , are positive definite quantities, we must require ordinary matter to have $w \geq 0$. Indeed from statistical mechanics we find that $w = 1/3$ for radiation as well for relativistic matter and $w = 0$ for non relativistic matter.

An important parameter related to each one of the species of the Universe is the *dimensionless density parameter*, which, for a generic component I is given by:

$$\Omega_I \equiv \frac{8\pi G \rho_I}{3H^2} = \frac{\rho_I}{\rho_{\text{crit}}}, \quad (1.20)$$

where we have introduced the *critical density*: $\rho_{\text{crit}} = 3H^2/(8\pi G)$.

1.1.3 Redshift and Cosmic Distances

Redshift

In an expanding Universe, light traveling through space is subject to a stretch of the wavelength in proportion to the scale factor. To take this effect into account it is usual to introduce the *redshift*:

$$z \equiv \frac{\lambda_0 - \lambda_e}{\lambda_e}, \quad (1.21)$$

where λ_e is the wavelength of radiation emitted by the source at t_e , and λ_0 is the wavelength of the same radiation as received by the observer at t_0 . One can show that it is possible to connect the redshift to the scale factor by means of the relativistic Doppler effect, obtaining a fundamental relation:

$$1 + z = \frac{a_0}{a} = \frac{1}{a}. \quad (1.22)$$

In this way, it is possible to interchangeably use a or z .

Proper and Comoving distance

In a cosmological context there is not a unique way to define the distance. The first one we are going to introduce is known as *proper distance*. We compute it assuming $dt = 0$ (i.e. time does not varies during our measurement) and, without loss of generality, that the observer is located at the center of the reference frame and $d\theta = d\phi = 0$ (i.e. the measurement is made keeping θ and ϕ constant). The proper distance is thus obtained by integrating the FRLW metric from the point $P_0 = (0, 0, 0)$ to the point $P = (r, 0, 0)$:

$$d_P = \int_0^r \frac{a dr'}{\sqrt{1 - Kr'^2}} = a(t)f(r). \quad (1.23)$$

Here $f(r)$ is the geometry-dependent term:

$$f(r) = \begin{cases} \sin^{-1} r & \text{for } K = +1 \\ r & \text{for } K = 0 \\ \sinh^{-1} r & \text{for } K = -1 \end{cases}. \quad (1.24)$$

It is interesting to note how the proper distance of a point with fixed r changes depending on the geometry of the Universe.

The *comoving distance* can be defined as the proper distance computed at the present time t_0 :

$$d_c = d_P(t_0) = a_0 f(r) = \frac{a_0}{a} d_P(t). \quad (1.25)$$

We see that d_c factors out from d_P the effects on distance induced by the expansion of the Universe (i.e. $a(t)$).

We now introduce two operational ways of defining the distance. These play a key role in observational cosmology, as we will see in the next section.

Luminosity distance

Let us consider a source emitting light, characterized by known luminosity L . This source has coordinate r at a time t (we are continuing to assume the observer located at the origin of the reference frame P_0 and $d\theta = d\phi = 0$). Let l be the

flux (i.e. the power received per unit area) at time t_0 by the observer. We can introduce the *luminosity distance* in the following way:

$$l = \frac{L}{4\pi d_L^2}. \quad (1.26)$$

We know that the area of a spherical surface centred on P and passing through P_0 at the time t_0 is given by $4\pi a_0^2 r^2$. The light received by the observer is redshifted by the expansion of the Universe by a factor a/a_0 . Also, it can be shown that due to the relativistic time dilation effect another factor a/a_0 has to be taken into account. We therefore have:

$$l = \frac{L}{4\pi a_0^2 r^2} \left(\frac{a}{a_0}\right)^2. \quad (1.27)$$

We then combine the two previous equations to obtain:

$$d_L = a_0^2 \frac{r}{a}. \quad (1.28)$$

Angular Diameter distance

Let us now consider an object with known proper length $D_P(t)$ placed at coordinate r at time t . Let $\Delta\theta$ be the angle subtended by this object, we then have:

$$D_P = ar\Delta\theta. \quad (1.29)$$

At this point we can define the *angular diameter distance* as:

$$d_A = \frac{D_P}{\Delta\theta} = ar. \quad (1.30)$$

We note that d_L and d_A are connected by the so-called *distance duality relation* [3]:

$$d_L = (1+z)^2 d_A. \quad (1.31)$$

1.1.4 Observational Evidence of Dark Energy

As we are going to see in this section, various independent probes indicate that our Universe is subject to a late-time accelerated expansion. We see from eq (1.18) that if we want a component to be responsible for such a positive acceleration, we must require it to have:

$$P < -\rho/3 \quad \Rightarrow \quad w < -1/3. \quad (1.32)$$

A component with this peculiar feature is called *Dark Energy* (DE). A particular kind of DE is the one with equation of state $w = -1$, in this case we refer to it as the *Cosmological Constant* Λ .

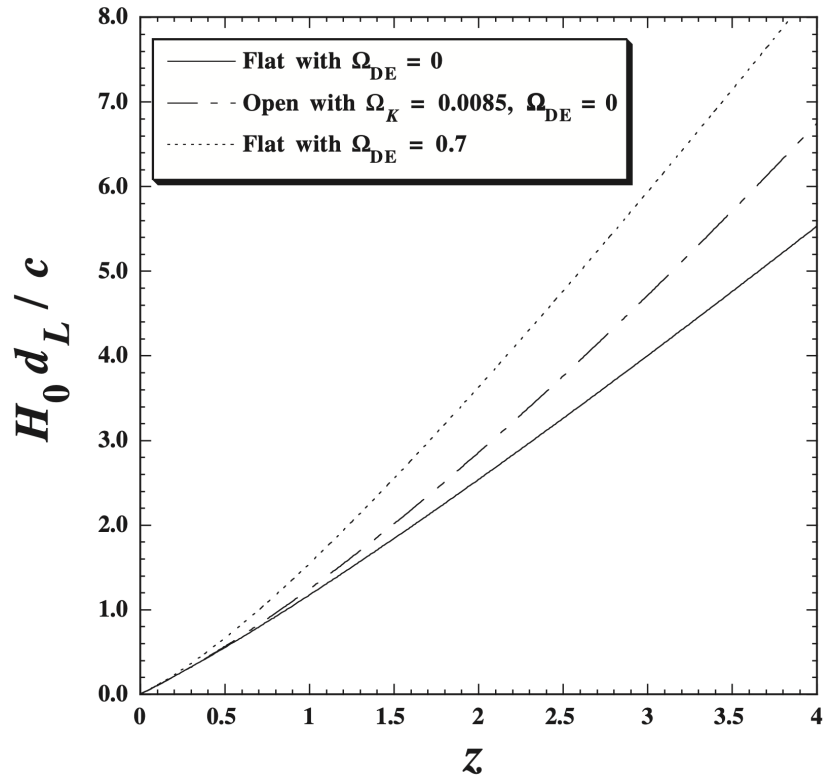


Figure 1.1: Luminosity distance d_L as a function of the redshift z in three different cases: flat Universe without DE (solid line), open Universe without DE (dash-dotted line) and flat Universe with DE (dotted line). The presence of DE results in greater d_L with respect to the case without it. This figure is taken from [36].

Supernova Observations

The first strong observational evidence of the accelerated expansion of the Universe came in 1998 thanks to the measurement of the distance-luminosity relation of type Ia supernovae (SN Ia) by two independent research groups: the High-redshift Supernova Search Team (HSST) [6] and the Supernova Cosmology Project (SCP) [7]. A SN Ia explosion takes place in a binary system in which a white dwarf³ accretes matter from the companion star (usually a red giant⁴, but it can be also a smaller star, even another white dwarf) until its mass exceeds the Chandrasekhar limit $M_{\text{Ch}} \approx 1.44 M_{\odot}$ [8]. A remarkable property of this phenomenon is that, since the Chandrasekhar limit mass is approximately constant, all the explosions have similar characteristics (such as the luminosity and the shape of the light curve). This makes the SN Ia a *standard candle*, i.e. an object with known absolute magnitude (in the case of SN Ia we have an absolute magnitude $M \approx -19$ at

³White dwarf stars are the remnants of low to intermediate mass stars. These compact objects balance the gravitational collapse with the electron degeneracy pressure, arising from quantum mechanical effects.

⁴Red giants stars are at an intermediate point of their evolution. They are characterized by large volumes, high luminosities, and outer atmospheres with low temperatures and densities.

the peak of brightness). In the late 1990s SN Ia became even more reliable as standard candles: thanks to a sample of high-quality data at low redshift it was possible to tightly connect brighter explosions with broader light curves [9]. This means that by measuring the apparent magnitude of a SN Ia and its light curve it is possible to predict its absolute magnitude. Let now cosmology come into play: we can compute the luminosity distance d_L of a SN Ia once we have measured its apparent magnitude m and we have estimated its absolute magnitude M :

$$m - M = 5 \log_{10} \left(\frac{d_L}{10 \text{ pc}} \right). \quad (1.33)$$

We can also compute its redshift from spectroscopy and then, from the observation of a sufficiently large number of SN Ia, we can obtain the dependence of the luminosity distance in terms of z . If we assume the Universe to be dominated by a non-relativistic fluid and dark energy with equation of state w_{DE} , Taylor-expanding d_L around $z = 0$, in the limit $z \ll 1$, we obtain:

$$d_L(z) = \frac{c}{H_0} \left[z + \frac{1}{4} (1 - 3w_{\text{DE}}\Omega_{\text{DE},0} + \Omega_{K,0}) z^2 + \mathcal{O}(z^3) \right]. \quad (1.34)$$

Here the subscript 0 indicates the present day value and we have introduced the dimensionless curvature density parameter:

$$\Omega_K \equiv -\frac{K}{(aH)^2}. \quad (1.35)$$

As we can see in equation (1.34) and in figure 1.1, if DE is present ($\Omega_{\text{DE},0} > 0$ and $w_{\text{DE}} < 0$) $d_L(z)$ gets larger. Moreover, from figure 1.1, we can also see that $d_L(z)$ is sensitive to deviations from a flat Universe. The 2011 Nobel prize winners HST and SCP groups found that the distance luminosity of SN Ia at different redshift is consistent with a flat Universe and the presence of a DE fluid which drives the late-time accelerated cosmic expansion. After 1998 more SN Ia data have been collected by different surveys (e.g. the Hubble Space Telescope (HST)) and it has been possible to put some tighter boundaries on the values of $\Omega_{\text{DE},0}$ and w_{DE} . Some of the constraints coming from SN Ia observations, as well as from other probes, are grouped in figure 1.2.

Other Probes

The luminosity distance of SN Ia is not the only evidence supporting the presence of DE in our Universe, indeed other independent probes came in the last decades, some remarkable ones are:

- **Cosmic Microwave Background:** the angular power spectrum of the temperature anisotropies of the CMB is a gold mine for what concerns the information about the cosmological parameters. In particular the measurement of the angular scale of the first peak of such spectrum let us put solid constraints on the spatial flatness of the Universe. Since in the present day

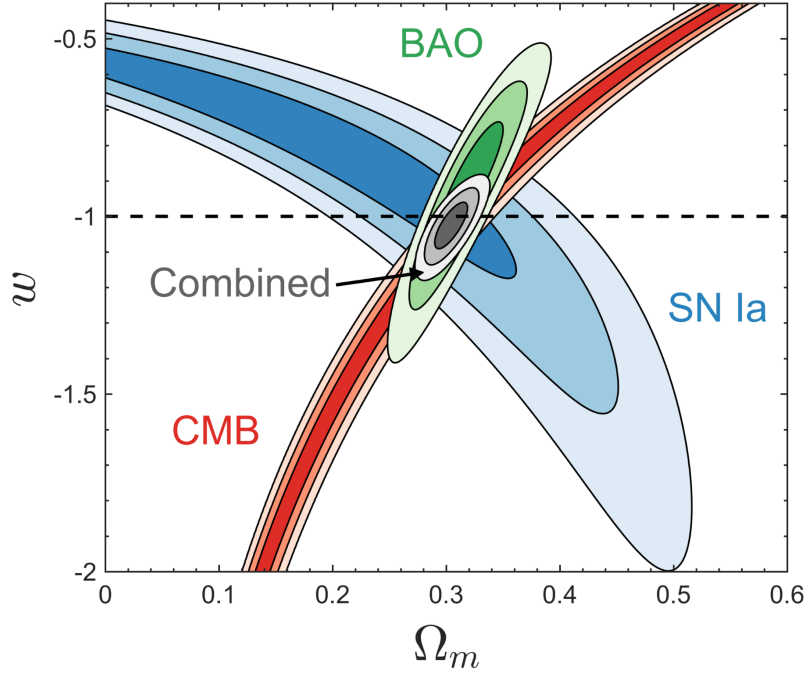


Figure 1.2: Constraints on the matter density parameter Ω_m and the DE equation of state w from the analysis made in [10] concerning three principal probes: SN Ia (JLA [11]; blue), BAO (BOSS DR12 [12]; green), and CMB (Planck 2015 [13]; red). The contours contain 68.3%, 95.4%, and 99.7% of the likelihood, and a flat universe is assumed. Figure taken from [10].

Universe we measure the matter density parameter to be $\Omega_{m,0} \approx 0.3$ and the one of the radiation to be $\Omega_{\gamma,0} \approx 10^{-5}$, an additional DE component is required to provide the remaining $\Omega_{DE,0} \approx 0.7$ as expected in a practically flat Universe.

- **Baryonic Acoustic Oscillations (BAO):** these are the oscillations in the matter power spectrum due to the coherent oscillations in the baryon-photon fluid that took place in the early Universe, before recombination. The result of this phenomenon is a greater probability of galaxies being separated by a characteristic distance called *sound horizon*. BAO are an excellent way to put constraints on DE since make us able to measure the angular diameter distance d_A to high redshift, as well as the Hubble parameter $H(z)$, using the sound horizon as a *standard ruler*, which, in analogy with the standard candle, is an object with known physical size.

The constraints that the probes mentioned above can put on w_{DE} and $\Omega_{DE,0}$ (or equivalently $\Omega_{m,0}$, since $\Omega_{m,0} + \Omega_{DE,0} \approx 1$) are shown in figure 1.2 according to the recent analysis made in [10].

1.1.5 Cosmological Constant and the Λ CDM Model

The cosmological constant, labeled Λ , was first introduced by Einstein in order to describe the Universe he had in mind: a static one, eternal and not expanding nor contracting. In presence of the cosmological constant the field equation (1.6) becomes:

$$R_{\mu\nu} - \frac{1}{2}g_{\mu\nu}R - \Lambda g_{\mu\nu} = 8\pi GT_{\nu}^{\mu}. \quad (1.36)$$

We have that this is not actually a *modification* of the field equations, but the most general form in which these can be written, remaining of the second order in the metric. Indeed (1.6) can be seen as a special case of (1.36) in which the constant term Λ has been explicitly set to zero. Another approach from which the field equations can be derived is the variational formalism. In this context, we obtain the equations by perturbing the action S , and also in this case it can be shown that the most general expression of the action, that involves derivatives of the metric that are not beyond the second order is comprehensive of the simplest scalar that is possible to construct from the metric (besides the Ricci scalar), namely a constant. The action takes thus the following form:

$$S = \frac{1}{16\pi G} \int d^4x \sqrt{-g} (R - 2\Lambda) + S_m, \quad (1.37)$$

where g is the trace of the metric tensor and S_m is the matter action. We can notice that Λ has two possible interpretations:

- An alternative theory of gravity in which the Einstein tensor is:

$$\tilde{G}_{\mu\nu} = G_{\mu\nu} + \Lambda g_{\mu\nu}. \quad (1.38)$$

- An additional component of the energy budget our Universe, so that the energy-momentum tensor becomes:

$$\tilde{T}_{\mu\nu} = T_{\mu\nu} - \frac{\Lambda}{8\pi G} g_{\mu\nu}. \quad (1.39)$$

Assuming the latter scenario we can rewrite the Friedmann equations in the case of a Universe with a cosmological constant:

$$H^2 = \frac{8\pi G}{3}\rho - \frac{K}{a^2} + \frac{\Lambda}{3}, \quad (1.40)$$

$$\frac{\ddot{a}}{a} = -\frac{4\pi G}{3}(\rho + 3P) + \frac{\Lambda}{3}, \quad (1.41)$$

and find the exact values required to ρ and Λ in order to obtain a static Universe:

$$\rho = \frac{\Lambda}{4\pi G}, \quad \Lambda = \frac{K}{a^2}. \quad (1.42)$$

Since we want ρ to be a positive quantity, this kind of Universe is forced to have $K > 0$ and thus a spherical geometry. In general, we can model Λ as a perfect fluid, then its pressure and density will be:

$$P_\Lambda = -\frac{\Lambda}{8\pi G}, \quad \rho_\Lambda = \frac{\Lambda}{8\pi G}. \quad (1.43)$$

We can see that it is characterized by negative pressure and constant density. Moreover, as seen previously, we can state that the cosmological constant is a form of DE, as it allows for accelerating solution of the Friedmann's equations, since:

$$w_\Lambda = -1. \quad (1.44)$$

Shortly after the introduction of the cosmological constant, the hypothesis of a static Universe, and so the need for Λ , had to be discarded due to Hubble's discovery of the expansion of the Universe [2]. However at the end of the past century, Λ came back in action as the most probable culprit of the late-time positive acceleration introduced in the previous section. Nowadays the Standard Model of cosmology relies mainly on three elements:

- A *Cosmological Constant* Λ , which is responsible for the accelerated expansion of the present day Universe.
- A form of *Cold Dark Matter* (CDM), which is collisionless, non baryonic and dissipationless. CDM particles were able to clump efficiently in the early universe, and their gravitational effects are the main driver of the evolution of the large-scale structure (LSS) (see e.g. [4]).
- A brief epoch in the very early Universe, called *Inflation*, during which the slow rolling⁵ of a scalar field drove the exponential expansion of the Universe, which also justifies its flatness. The oscillations of this scalar field at the end of inflation gave rise to the particles populating our Universe. Inflation is also responsible for the very initial perturbations that grew into the structures observed today. It is indeed possible to predict from Quantum Field Theory (QFT) the statistical properties of the small fluctuations of the scalar field during inflation, which generated perturbations of the metric that in turn imprinted the primordial perturbations of radiation and matter after inflation (see e.g. [5]).

It will not be a surprise that we refer to this model as Λ CDM.

⁵It can be shown [15] that if a scalar field is rolling down a potential energy hill slowly enough compared to the expansion rate of the Universe, this can give rise to an exponential cosmic expansion.

1.2 Problems of the Λ CDM Model

Even if the Λ CDM model is in very good agreement with observational data coming from different fields, it is definitely not free from problems and tensions. In this chapter we are going to give an overview of the two most notorious problems of this model, the coincidence and fine-tuning problem, as well as tensions that have arisen in more recent years, the σ_8 and the Hubble tension.

1.2.1 The Fine Tuning Problem

As we said previously, in the Λ CDM model, the cosmological constant is responsible for the actual cosmic acceleration. From eq. (1.40) we can see that in order to make this happen we require Λ to be of the same order of magnitude of the squared present day Hubble parameter H_0 [14]:

$$\Lambda \approx H_0^2 = (2.0504h \times 10^{-42} \text{ GeV})^2, \quad (1.45)$$

where we have used $h \approx 0.7$. From eq. (1.43) this leads to the following approximate value for the energy density of the cosmological constant:

$$\rho_\Lambda \approx 10^{-47} \text{ GeV}^4. \quad (1.46)$$

Λ is not a perfect stranger in the world of particle physics, indeed there could be a natural candidate coming from QFT which is the vacuum energy of an empty space. We can calculate its predicted value starting from the zero-point energy of some field of mass m and momentum k , which is given by $E = \sqrt{k^2 + m^2}/2$ (in units of $\hbar = 1$), and summing it over all the energy/momentum scales k up to the Planck scale k_{pl} . This lead us to the following estimate for the vacuum energy:

$$\rho_{vac} \approx 10^{74} \text{ GeV}^4. \quad (1.47)$$

We thus find a strong inconsistency: the predicted energy density of the vacuum is 121 orders of magnitude larger than the observed energy density of the cosmological constant. Therefore, from this perspective, there must be some mechanism (e.g. an additional fundamental symmetry that is presently unknown) responsible for an extra contribution, able to cancel the vacuum energy, but not completely. Nevertheless this contribution should be extremely fine tuned: a perfect symmetry would indeed lead to an exactly null vacuum energy, in this case we would need to find another explanation for DE; on the other hand, in order to leave the tiny observed DE density not vanish at all, we need an almost, but not quite, perfect cancellation. Despite interesting attempts to solve it (see e.g. [29, 30, 31]), as well as arguments in favour of an anthropic interpretation (see e.g. [32]), this problem remains still open, and is regarded as one of the major puzzles of fundamental physics.

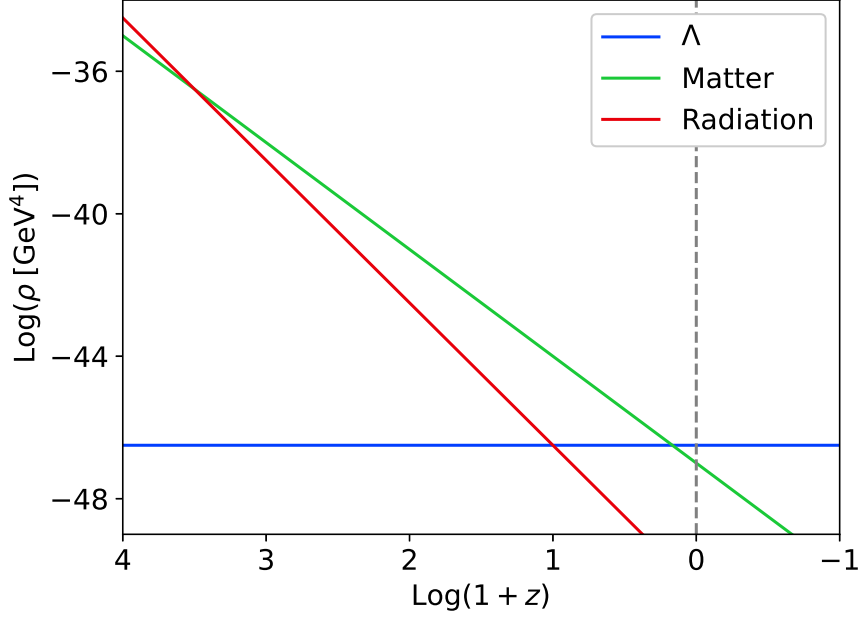


Figure 1.3: Evolution of the energy density of the different components of the Universe as a function of redshift. The dashed line indicates the present time. Matter (green line) and radiation (red line) scale as $(1+z)^3$ and $(1+z)^4$ respectively, while the density of the cosmological constant (blue line) remains unaltered at different times.

1.2.2 The Coincidence Problem

There is another major problem which affects the cosmological constant, this is the so-called coincidence problem. Let us start from eq. (1.19), we see that the evolution as a function of a (or equivalently of redshift z) of the energy density of every component of the universe is described by a power law:

$$\rho = \rho_0(1+z)^{3(1+w)}, \quad (1.48)$$

where we used the relation $a = 1/(1+z)$ and ρ_0 is the present day energy density of the referred component. So, considering the three main ingredients of the Universe, we have:

$$\rho_\gamma \propto (1+z)^4, \quad \rho_m \propto (1+z)^3, \quad \rho_\Lambda = const, \quad (1.49)$$

where we used the subscripts γ , m and Λ for radiation, matter and cosmological constant respectively. It follows that in the history of our Universe, for the vast majority of the time, there has been only a dominant component at a time. This can be seen more clearly by taking a look at figure 1.3. We can also notice that we are living in one of the very rare, and relatively short, periods in which the density of two components (in this case matter and Λ) are comparable. To persuade of that coincidence we can calculate the redshift at which matter and Λ

had the same density:

$$1 + z_{eq,m,\Lambda} = \left(\frac{\rho_{\Lambda,0}}{\rho_{m,0}} \right)^{1/3} \approx 0.3, \quad (1.50)$$

which is quite a recent time.

1.2.3 The Hubble and the σ_8 Tension

In recent years, the improved measurements of H_0 at low redshifts, as well as the steps forward in the CMB observation, suggested a tension arising on the estimated value of H_0 . The current most precise local method to measure H_0 relies essentially on two steps: the calibration of luminosity and distance to nearby galaxies (typically by means of Cepheid⁶ variables) followed by the calibration of larger distances on the more luminous SN Ia (up to $z \approx 0.15$). The value of H_0 measured with this method is in significant tension (about 3σ) with the lower one measured by Planck, which on the other hand is in good concordance with the value obtained from measurements of baryon acoustic oscillations in combination with SNe Ia. It has to be noted that the Planck data give an indirect and highly model-dependent estimate of H_0 , based on the angle subtended by the sound horizon as observed in CMB temperature power spectrum. This model-dependence is a crucial fact that opens the door to the exploration of alternative cosmologies. Possibilities include early dark energy [27], decaying dark matter, evolving dark energy, dark radiation, modified gravity or deviations from flatness [28]. One basic example of evolving dark energy approach which could be used to address this problem consists in assuming a time dependent equation of state for dark energy [33, 34], given by $w(a) = w_0 + w_a(1 - a)$, where w_0 and w_a are two free parameters that could be set in order to alleviate the tension.

Moreover there's (at least) another significant tension: it concerns the amplitude of the power spectrum of density perturbations (usually referred as σ_8). The value of σ_8 measured by different LSS indicators at low redshift including clusters, lensing and redshift-space distortions turns out to be significantly lower than the one predicted by CMB measurements in combination with the assumption of the Λ CDM model [26]. This tension could be alleviated, but still not solved, allowing a massive active neutrino, to be part of the Cosmological Model, thus invoking again the need to study models which are different from Λ CDM.

1.3 Cosmological Perturbation Theory

Until now we have treated the Universe as homogeneous, the first step toward a more accurate and realistic description is represented by the linear perturbation

⁶A Cepheid is a variable star characterized by radial pulsations. Its variation in diameter and temperature produces oscillations in brightness which have a well defined period and amplitude. The tight relationship between the luminosity and the pulsation period makes the Cepheids very reliable standard candles.

theory. We are going to consider solutions of the Einstein equation which are made up of a homogeneous background Universe with a FLRW metric plus some deviations from this background that are small enough to be modeled by a first order Taylor expansion.

1.3.1 Perturbing the Einstein Equation

We start by perturbing the metric, which, as mentioned above, we assume to be described by the sum of two terms: a background metric tensor $g_{\mu\nu}^{(0)}$ and a small perturbation $\delta g_{\mu\nu}$:

$$g_{\mu\nu} = g_{\mu\nu}^{(0)} + \delta g_{\mu\nu}. \quad (1.51)$$

Let us introduce two useful quantities: the conformal time η and the conformal Hubble function \mathcal{H} . These are given by simply rescaling t and H by the scale factor a :

$$\eta \equiv \int \frac{dt}{a}, \quad \mathcal{H} \equiv \frac{1}{a} \frac{da}{d\eta} = aH. \quad (1.52)$$

To describe the FLRW background metric we can rewrite eq (1.1) as:

$$ds^2 = g_{\mu\nu}^{(0)} dx^\mu dx^\nu = a^2(-d\eta^2 + \delta_{ij} dx^i dx^j). \quad (1.53)$$

At this point we have freedom of choice for what concerns the coordinates to use for the perturbed quantities: in fact the so-called *gauge transformations* have the property to leave unaltered background metric while changing the perturbed metric. We will use the *Newtonian gauge*, in which the observer is fixed to the unperturbed background frame. Moreover, in the most general case, we would have to consider not only *scalar*, but *vector* and *tensor* perturbations as well. However, since we are dealing with perturbations of density, which is a scalar quantity, it can be shown that vector and tensor perturbation terms can be fairly neglected [36], leading to the following:

$$\delta g_{\mu\nu} = a^2 \begin{pmatrix} -2\Psi & 0 \\ 0 & -2\Phi\delta_{ij} \end{pmatrix}, \quad (1.54)$$

where Ψ and Φ are two spatial scalars. We can now write the perturbed metric in the Newtonian gauge:

$$ds^2 = a^2(\eta) [-(1 + 2\Psi) d\eta^2 + (1 - 2\Phi)\delta_{ij} dx^i dx^j]. \quad (1.55)$$

It is now possible to calculate the perturbed version of the Einstein equation passing through the Christoffel symbols in the same fashion we did in 1.1.1. This time we are going to deal with two (tensor) equations:

$$G_\nu^{\mu(0)} = 8\pi G T_\nu^{\mu(0)}, \quad \delta G_\nu^\mu = 8\pi G \delta T_\nu^\mu. \quad (1.56)$$

The first gives the Friedmann equations for the background evolution, while the second is the first order perturbed equation we are interested in. After some calculations, we obtain the perturbed Einstein tensor:

$$\delta G_0^0 = 2a^{-2} [3\mathcal{H}(\mathcal{H}\Psi + \Phi') - \nabla^2\Phi], \quad (1.57)$$

$$\delta G_i^0 = -2a^{-2}(\Phi' + \mathcal{H}\Psi)_{|i}, \quad (1.58)$$

$$\begin{aligned} \delta G_j^i &= 2a^{-2} [(\mathcal{H}^2 + 2\mathcal{H}')\Psi + \mathcal{H}\Psi' + \Phi'' + 2\mathcal{H}\Phi'] \\ &\quad + a^{-2} [\nabla^2(\Psi - \Phi)\delta_j^i - (\Psi - \Phi)_{|j}^i], \end{aligned} \quad (1.59)$$

where the subscript $|$ indicates the covariant derivative with the spatial 3-metric, and $\nabla^2 f \equiv f_{; \mu}^{\mu}$. At this point, we need to calculate δT_ν^μ in order to complete the equation (1.56), to do so, we have to specify the matter source. In the next section we are going to calculate δT_ν^μ for the simple case of one non-relativistic component. Since we are going to perturb the energy-momentum tensor, we must introduce the four-velocity $u^\mu \equiv \frac{dx^\mu}{d\tau}$, with $\tau \equiv \sqrt{-ds^2}$, and its first order perturbation:

$$u^\mu = \left[\frac{1}{a}(1 - \Psi), \frac{v^i}{a} \right]. \quad (1.60)$$

In the last equation we have introduced the peculiar velocity $v^i = \frac{dx^i}{d\eta} = a \frac{dx^i}{dt}$.

1.3.2 Equations for a Single Fluid

The energy-momentum tensor of a perfect fluid is given by:

$$T_{\mu\nu} = (\rho + P)u_\mu u_\nu + P g_{\mu\nu}. \quad (1.61)$$

We are going to assume that also the perturbed fluid is still a perfect fluid, which means that $\delta T_j^i = 0$ when $i \neq j$. Let us now introduce our two perturbed quantities: the density contrast and the velocity divergence:

$$\delta \equiv \frac{\delta\rho}{\rho} \equiv \frac{\rho - \bar{\rho}}{\bar{\rho}}, \quad \theta \equiv \nabla_i v^i, \quad (1.62)$$

with $\bar{\rho}$ being the spatial average of the density field. Keeping in mind that our fluid has equation of state $w = P/\rho$, we can write its perturbed energy momentum tensor:

$$\delta T_\nu^\mu = \rho [\delta(1 + c_s^2)u_\nu u^\mu + (1 + w)(\delta u_\nu u^\mu + u_\nu \delta u^\mu) + c_s^2 \delta \delta_\nu^\mu], \quad (1.63)$$

where we have introduced the sound speed c_s , defined through $c_s^2 \equiv \delta P/\delta\rho$. At this point we are ready to write our set of first order perturbation equations:

$$3\mathcal{H}(\mathcal{H}\Psi + \Phi') - \nabla^2\Phi = -4\pi G a^2 \rho \delta, \quad (1.64)$$

$$\nabla^2(\Phi' + \mathcal{H}\Psi) = -4\pi G a^2 (1 + w) \rho \theta, \quad (1.65)$$

$$\Psi = \Phi, \quad (1.66)$$

$$\Phi'' + 2\mathcal{H}\Phi' + \mathcal{H}\Psi' + (\mathcal{H}^2 + 2\mathcal{H}')\Psi = 4\pi G a^2 c_s^2 \delta \rho, \quad (1.67)$$

where the prime represents the derivative with respect conformal time η . Finally, we move to the *Fourier space*, and use the continuity equation (1.15) in combination with the four above, to obtain the cosmological equivalent of the classical *continuity* and *Euler* equations:

$$\delta' = -3\mathcal{H}(c_s^2 - w)\delta + (1 + w)(3\Phi' - \theta), \quad (1.68)$$

$$\theta' = - \left[\mathcal{H}(1 - 3w) + \frac{w'}{1 + w} \right] \theta + k^2 \left[\frac{c_s^2}{1 + w} \delta + \Psi \right], \quad (1.69)$$

where δ , θ , Φ and Ψ are implicitly referred to the specific wavenumber k associated to a Fourier mode. It is important to note that these equation become linear in the Fourier space, this means that each mode is decoupled from the others, and thus evolves independently.

1.3.3 Evolution of Perturbations

We now consider a relevant limit in which these equations can be solved, thus giving some important physical insights on the evolution of perturbations. Before doing so, we introduce a fundamental length scale in cosmology, the *cosmological horizon*, defined as:

$$R_H(t) = a(t) \int_0^t \frac{c dt'}{a(t')}. \quad (1.70)$$

This is the maximum distance that is possible to cover (i.e. traveling at the speed of light) in an expanding Universe at a given cosmic time t . The importance of this scale lies in the fact that it defines the portion of the Universe that can be causally connected with the observer. At scales larger then the horizon, gravity is the only acting force. R_H is often approximated with the *Hubble radius*, defined as follows:

$$\tilde{R}_H(t) = \frac{c}{H}. \quad (1.71)$$

Sub-Horizon Limit

Let us consider scales that are smaller than the horizon, i.e. we take the limit $k \gg \mathcal{H}$, and focus on a dust component, i.e. a pressureless fluid with $w = 0$ (this holds for matter), and we take $c_s \ll 1$. With these assumptions, eq. (1.64) becomes the well known Poisson equation in Fourier space:

$$k^2\Phi = -4\pi G\rho\delta. \quad (1.72)$$

It is also easy to show that eq (1.68) and (1.69) become:

$$\delta' = -\theta, \quad (1.73)$$

$$\theta' = -\mathcal{H}\theta + k^2 c_s^2 \delta + k^2 \Phi. \quad (1.74)$$

We now differentiate eq (1.73) and plug it into eq (1.74) to obtain the following second order differential equation:

$$\delta'' + \mathcal{H}\delta' + \left(c_s^2 - \frac{3}{2}\mathcal{H}\right)\delta = 0. \quad (1.75)$$

From the equation above we have that the perturbation will not grow under the condition:

$$c_s^2 k^2 - \frac{3}{2}\mathcal{H}^2 > 0. \quad (1.76)$$

This can be translated in physical space, finding that all the perturbations with a wavelength $\lambda < \lambda_J$ will be characterized by an oscillating solution, meaning that they are not able to grow in time. Here λ_J is the Jeans scale:

$$\lambda_J = c_s \sqrt{\frac{\pi}{G\rho}}. \quad (1.77)$$

On the other hand, the perturbations with $\lambda > \lambda_J$ are not damped. In the limit $c_s k \ll \mathcal{H}$ gravity dominates over the pressure and eq. (1.75) becomes:

$$\delta'' + \mathcal{H}\delta' - \frac{3}{2}\mathcal{H}^2\delta = 0. \quad (1.78)$$

We can solve this equation, finding the growing and decaying solutions:

$$\delta_+ = Aa, \quad \delta_- = Ba^{-\frac{3}{2}}. \quad (1.79)$$

In particular we are interested in the first one, while the second becomes rapidly negligible. We note that the pre-factor depends on the initial conditions, these are fixed during inflation, as briefly mentioned earlier. Let us consider the so-called *matter era*, which began at the time of equivalence t_{eq} ($z \approx 10^3 - 10^4$) when radiation was replaced by matter as the dominant component of the Universe, and ended recently, as we saw in section 1.2.2. It can be shown, by means of eq. (1.19) and the assumption of a flat Universe, that during this era the perturbations had grown as $\delta_+ \propto t^{2/3}$, as long as linear theory holds.

An Overview

The linear perturbation equations derived in this section can be successfully used under different assumptions to describe the behaviour of the various components of the Universe during the different epochs at different scales. Before exposing the main results we introduce the time of *decoupling* t_{dec} ($z \approx 1100$) after which the baryonic matter ceased to be coupled to radiation. We indicate with δ_c , δ_b and δ_γ density perturbations of CDM, baryons and radiation respectively.

- Super-horizon scales: all the component follow the dominant one, so that before t_{eq} radiation dominates and one has $\delta_\gamma \propto \delta_c \propto \delta_b \propto a^2$, after t_{eq} matter dominates so that $\delta_c \propto \delta_b \propto \delta_\gamma \propto a$.

- Sub-horizon scales: for $\lambda < \lambda_J$, as seen previously, every perturbation undergoes to an oscillating solution which is therefore not able to grow. For $\lambda > \lambda_J$ we have that CDM perturbations remain approximately constant before t_{eq} (this phenomenon is known as *Meszaros effect* [35]) and then grow like $\delta_c \propto a$. On the other hand the perturbations of baryonic matter, as long as $t < t_{\text{dec}}$, will follow the ones of radiation which are found to be oscillating; after t_{dec} baryons decouple from radiation and are free to follow the perturbations of CDM that had grown in the meantime (this phenomenon is known as *baryon catch-up*), in this case one finds: $\delta_b \propto \delta_c(1 - \frac{a_{\text{dec}}}{a})$.

Chapter 2

Cosmological Observables

In this chapter we are going to give an overview of three important cosmological observable quantities that are commonly used to study the properties of the Universe and to connect the results of numerical simulations with the observations as well as with theoretical predictions. In the present work we will make use of these observables to test the effects of DE-baryon scattering.

2.1 Power Spectrum

Let us define the density contrast at a point in space with position \mathbf{x} as follows:

$$\delta(\mathbf{x}) \equiv \frac{\rho(\mathbf{x}) - \bar{\rho}}{\bar{\rho}} \quad (2.1)$$

where $\bar{\rho}$ is the spatial mean of the density field over a sufficiently large volume V . Since we have only one Universe at our disposal, we take advantage of the *ergodic hypothesis*, so that we can consider the average of a quantity over different, sufficiently large, volumes (dubbed *fair samples*) equivalent to the average over different realizations of the Universe. As mentioned in section 1.3, as long as linear theory holds, the orthonormal modes of the fluctuations evolve independently. It is therefore useful to expand the density contrast in Fourier series:

$$\delta(\mathbf{x}) = \sum_{\mathbf{k}} \delta_{\mathbf{k}} \exp(i\mathbf{k} \cdot \mathbf{x}) = \sum_{\mathbf{k}} \delta_{\mathbf{k}}^* \exp(-i\mathbf{k} \cdot \mathbf{x}), \quad (2.2)$$

where $\delta_{\mathbf{k}}$ are the Fourier coefficients, given by:

$$\delta_{\mathbf{k}} = \frac{1}{V} \int_V \delta(\mathbf{x}) \exp(-i\mathbf{k} \cdot \mathbf{x}) d^3\mathbf{x}. \quad (2.3)$$

From the conservation of mass in V , we have that $\delta_{\mathbf{k}=0} = 0$, and since $\delta(\mathbf{x})$ must assume real values, we have that $\delta_{\mathbf{k}}^* = \delta_{-\mathbf{k}}$.

From the inflation theory it follows that the primordial density fluctuations, which were generated by oscillations of the metric, are characterized by a completely random phase distribution. A consequence of this is that the density contrast can

be described in terms of a Gaussian distribution. From eq (2.1) we see that, by definition, the first moment (i.e. the mean) of the distribution is zero, however this is not true for what concerns the variance σ^2 , in fact we have:

$$\sigma^2 \equiv \langle \delta^2 \rangle = \sum_{\mathbf{k}} \langle |\delta_{\mathbf{k}}|^2 \rangle = \frac{1}{V} \sum_{\mathbf{k}} \delta_k^2, \quad (2.4)$$

where we are averaging over different realizations (or equivalently, different fair sample volumes). From eq. (2.4) one can see that $\langle |\delta_{\mathbf{k}}|^2 \rangle$ tells us how much the wavenumber \mathbf{k} contributes to the variance σ . Following the cosmological principle, we now assume the density field to be statistically homogeneous and isotropic, so that we will be interested only in $k = |\mathbf{k}|$. In the limit $V \rightarrow \infty$, we obtain:

$$\sigma^2 = \frac{1}{V} \sum_{\mathbf{k}} \delta_k^2 \rightarrow \frac{1}{2\pi^2} \int_0^\infty P(k) k^2 dk. \quad (2.5)$$

We have introduced the *power spectrum* $P(k) \equiv \delta_k^2$. This is a fundamental tool in cosmology since it represents the main way to express how much the density fluctuations at each scale k contribute to the total power. The power spectrum, whose domain is the Fourier space, always comes with its physical space alter ego, the *Two-Point Correlation Function* $\xi(r)$, defined as follows:

$$\xi(r) \equiv \langle \delta(\mathbf{x})\delta(\mathbf{x} + \mathbf{r}) \rangle. \quad (2.6)$$

In the above equation we are averaging over all the positions \mathbf{x} and over all the directions \mathbf{r} . We can see that $\xi(r)$ describes the excess of probability of two points being separated by a distance r , and it can be shown that $\xi(r)$ is the anti-Fourier transform of $P(k)$:

$$\xi(r) = \frac{1}{2\pi^2} \int_0^\infty P(k) k^2 \frac{\sin(kr)}{kr} dk. \quad (2.7)$$

A typical assumption for the functional form of the power spectrum is a power law, characterized by the *spectral index* n and the *normalization* A :

$$P = Ak^n, \quad (2.8)$$

and in particular, most inflationary theories provide a primordial spectrum with index $n \approx 1$. Moreover, since we do not want the variance to diverge, from eq. (2.5) we require the spectral index to be $n > -3$ for $k \rightarrow 0$ and $n < -3$ for $k \rightarrow \infty$. The evolution of the primordial power spectrum $P_i(k)$ up to the time of equivalence t_{eq} is usually embedded in the *transfer function* $T(k)$, so that:

$$P_{\text{eq}}(k) = P_i(k)T^2(k) \quad (2.9)$$

As we saw in section 1.3.3, before t_{eq} , dark matter perturbations have different behaviour depending on the scale one considers: for the smaller k (scales larger than the horizon) perturbations grow as $\delta_c \propto a^2$, on the other hand, for larger k

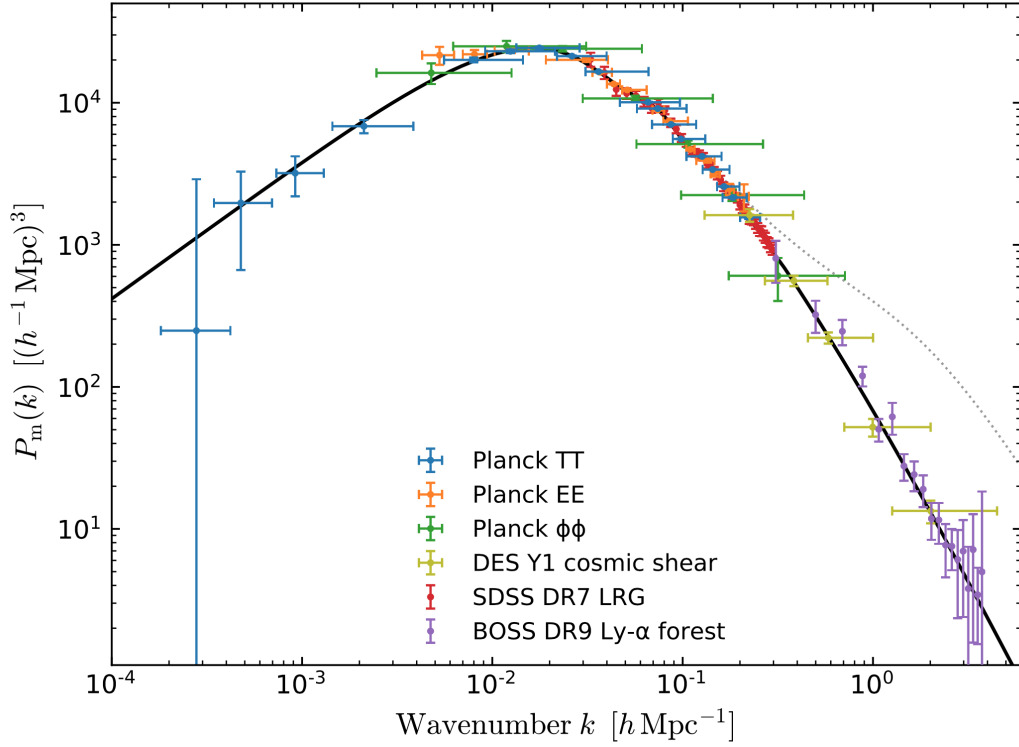


Figure 2.1: Linear-theory matter power spectrum at $z = 0$ (solid line) inferred from different cosmological probes (the dotted line shows the impact of nonlinear clustering at $z = 0$). This figure is taken from [14].

(scales smaller than the horizon), perturbations do not grow in time, so $\delta_c \approx \text{const}$. Since the cosmological horizon grows with time, scales with progressively lower k will enter inside the horizon thus ceasing to grow. This happens up to the scale k_{eq} which is equal to the horizon scale at t_{eq} . It can be shown that the effects explained above lead to the following form for the transfer function:

$$T(k) \propto \begin{cases} \text{const} & \text{for } k < k_{\text{eq}} \\ k^{-2} & \text{for } k > k_{\text{eq}} \end{cases}. \quad (2.10)$$

It is worth to say that, in analogy with λ_J for baryonic matter, also DM has a length scale under which all the perturbations are destined to vanish. This phenomenon is known in literature as *free-streaming*, and the associated threshold wavelength λ_{FS} is significantly dependent on the mass of DM particles. Coming back to the power spectrum, from linear theory we have that after t_{eq} , DM perturbations will grow as $\delta_c \propto a$ without distinction between scales that are larger or smaller than the horizon. The overall shape of $P(k)$ is thus preserved, while the total power grows with time. The matter spectrum at $z = 0$ predicted from linear theory and constrained by the most recent cosmological probes, is visible in figure 2.1. As times passes, the smallest scale for which linear theory ceases to hold becomes progressively larger, so that the effective growth of perturbations at

smaller scales results larger than the one predicted from linear theory, this effects are driven by the so-called *clustering* of matter. The approximate prediction of the deviation from the linear spectrum is also visible in figure 2.1, where it is represented by a dotted curve.

2.2 Mass Function

The *mass function* $n(M)$ is a statistical distribution that tells us the expected number of objects (e.g. galaxies, halos etc..) with mass between M and $M + dM$ per unit volume:

$$dN = n(M) dM. \quad (2.11)$$

In the case the mass-to-light ratio M/L is known, this can be directly converted into the luminosity function:

$$\phi(L) = n(M) \frac{dM}{dL}. \quad (2.12)$$

However, this ratio is not known with certainty, and moreover is very different for different objects: it goes from the order of 10 for galaxies to the order of 400 for clusters of galaxies. The mass function is a powerful tool that frequently comes into play in many cosmological problems, it is therefore very important to have analytic formulae that describe it. It is conventional to introduce the quantity σ^2 , which is the variance of the density field smoothed with a top-hat filter with a radius that encloses a mass M at the mean cosmic matter density:

$$\sigma^2(M) \propto \int_0^\infty k^2 P(k) W^2(k, M) dk. \quad (2.13)$$

We have that $\ln \sigma^{-1}$ can be considered as a mass-like variable, since for a fixed redshift and power spectrum, we see that higher masses translates in higher values of $\ln \sigma^{-1}$. With this introduction, we can express $n(M)$ as follows:

$$\frac{dn}{dM} = \frac{\rho_0}{M} \frac{d \ln \sigma^{-1}}{dM} f(\sigma), \quad (2.14)$$

where ρ_0 is the mean mass density of the universe. We now have that all the characteristics of a particular mass function model are embedded in $f(\sigma)$, which is defined as the fraction of mass in collapsed objects per unit interval in $\ln \sigma^{-1}$. The first remarkable example of analytical model is the *spherical collapse* formalism by Press & Schechter [16], which gives the following formula for $n(M)$:

$$f_{P-S}(\sigma) = \sqrt{\frac{2}{\pi}} \frac{\delta_c}{\sigma} \exp \left[-\frac{\delta_c^2}{2\sigma^2} \right], \quad (2.15)$$

where δ_c is a parameter extrapolated from linear theory, indicating the critical threshold from which a density perturbation can grow further. This model had

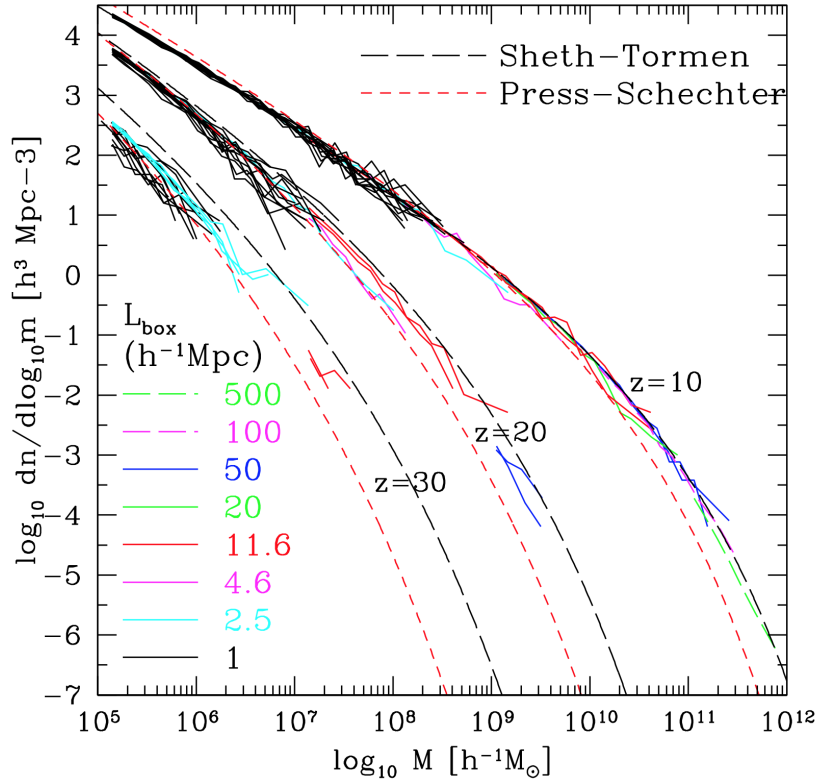


Figure 2.2: Comparison at different redshifts between Press & Schechter model (red dashed line), Sheth & Tormen (black dashed line) model and the mass function computed by numerical simulations of Λ CDM cosmology with different box sizes, in which the halos were detected by means of the FoF algorithm. This figure is taken from [25].

been improved by Sheth & Tormen [17], which proposed the *ellipsoidal collapse* formalism. This gives:

$$f_{S-T}(\sigma) = A \sqrt{\frac{2a}{\pi}} \left[1 + \left(\frac{\sigma^2}{a\delta_c^2} \right)^p \right] \frac{\delta_c}{\sigma} \exp \left[-\frac{a\delta_c^2}{2\sigma^2} \right]. \quad (2.16)$$

A plot of these two models at different redshifts, in comparison with the halo mass function as computed by means of numerical Λ CDM simulations is visible in figure 2.2. Another option to find an expression for $n(M)$ is to calibrate an analytical function on the basis of N-body simulations. A successful formula is the one found by Jenkins et al. [18]:

$$f_J(\sigma) = 0.315 \exp(-[\ln \sigma^{-1} + 0.61]^{3.8}). \quad (2.17)$$

Usually one also considers the cumulative mass function $N(> M)$, which gives the probability of an object to have mass greater than M :

$$N(> M) = \int_M^\infty n(M) dM. \quad (2.18)$$

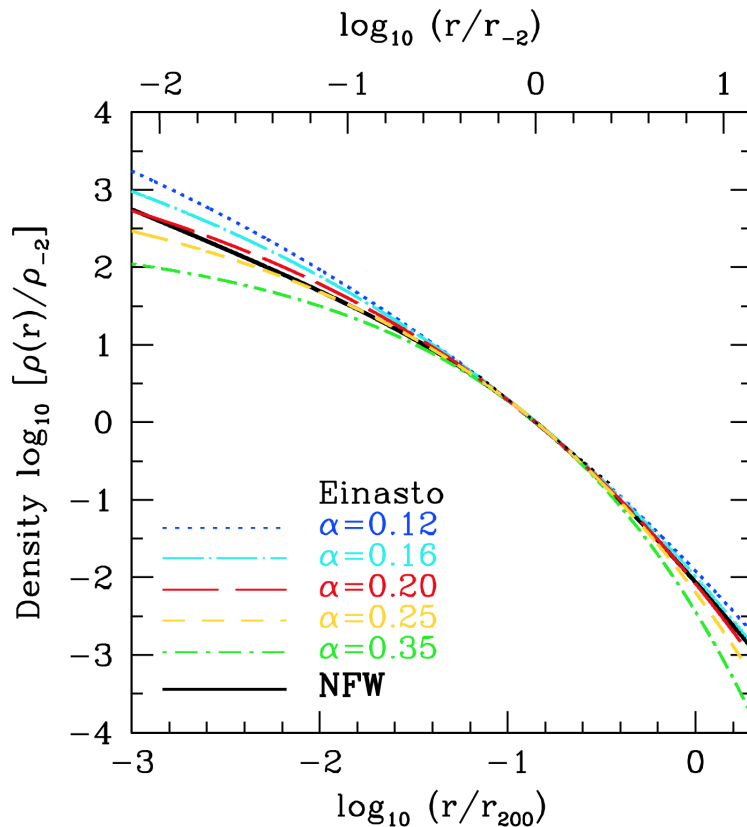


Figure 2.3: Comparison between the NFW and Einasto density profile for different values of the Einasto parameter α . This figure is taken from [24].

2.3 Halo Profiles

CDM Halos can be seen as the fundamental unit of cosmological structure. Even if we are not able to directly observe these objects, there are several probes of their existence (these include gravitational lensing, stellar dynamics etc.), which makes us able to put constraints on their structural features. The first evidence came from the observation of the velocity dispersion of galaxies in clusters [19]. Another strong evidence concerns the rotational curves of disk galaxies [20]: these show a constant trend at large radii, against the prediction of a Keplerian fall, proportional to $r^{1/2}$, predicted from the visible matter density distribution. In order to explain the observed rotational curves, the presence of underlying DM density distribution can be assumed. It is of particular interest therefore to investigate on the radial density distribution of such halos. A first simple model is the so called *Singular Isothermal Sphere* (SIS):

$$\rho_{\text{SIS}}(r) = \rho_0 \left(\frac{r}{r_0} \right)^{-2} = \frac{v_c^2}{4\pi G r^2}. \quad (2.19)$$

This density profile is the one derived in gasdynamics under the assumption of hydrostatic equilibrium and uniform temperature. We see that this profile is

characterised by a constant circular velocity $v_c = 2(\pi G \rho_0)^{1/2} r_0$, in agreement with the flat rotational curves at large radii observed in disk galaxies. The next profile we introduce is the *Universal Profile* of cold dark matter halos, that comes from studies on numerical simulations of the Λ CDM cosmology, this is the *Navarro, Frenk & White* (NFW) profile [22]:

$$\rho_{\text{NFW}}(r) = \frac{\rho_0}{(r/r_s)(1 + r/r_s)^2}, \quad (2.20)$$

where ρ_0 is the matter density of the Universe at the time of the collapse of the halo and r_s is the scale radius. A distinctive feature of this profile, and of profiles observed in numerical Λ CDM simulation, is the "cusp" trend at small radii, where $\rho \propto r^{-1}$, which is different from less steep "core" trend of the SIS profile, more supported by observations of rotation curves. Another remarkable profile is the *Einasto* profile [23]:

$$\rho_{\text{Ein}}(r) = \rho_s \exp \left\{ -\frac{2}{\alpha} \left[\left(\frac{r}{r_s} \right)^\alpha - 1 \right] \right\}, \quad (2.21)$$

where ρ_s is the value of the density at r_s . In this case the shape is further dependent on the *Einasto Parameter* α , which modulates the slope of the profile. A comparison between NFW and Einasto profile is visible in figure 2.3.

Halo Detection in Numerical Simulations

The task of detecting DM halos in N-Body simulations is not a trivial one. A typical way of proceeding is by means of the so-called *Friends-of-Friends* (FoF) algorithm (see e.g. [21]): once a linking length l is set, one requests that any particle that finds another particle within a distance l is linked to it in a group. In this way every particle is connected directly with its friends (particles distant no more than l) and indirectly to the friends of its friends. At this point the groups with a number of particles under a fixed threshold are discarded. Moreover, there is another algorithm, named SUBFIND, implemented in [69] for the first time, which is used to identify overdense, self-bound particle groups within a larger parent group by means of gravitational unbinding. The basic idea is the following: first, a local estimate of the density at the position of each particle is computed; second a local overdensity inside a group (e.g. a group identified with FoF) is considered a candidate for a **subgroup** structure; third the boundaries of the candidates are defined by progressively lowering the density threshold until different isodensity surfaces meet each other in a saddle point. Both FoF and SUBFIND are included in the code we are going to use for our numerical simulations (described in section 4.1): this means that for each snapshot, files containing the catalogues of the halos found with FoF and the groups and subgroups found with SUBFIND will be produced.

Once a halo or a subhalo is detected, in first place one wants to compute its mass. Since, by construction, in a simulation a halo is an ensemble of particles, one could take the mass contained in all particles that are found with a certain algorithm

as the mass of the halo, however this method is not so accurate and uneasy to link with observations. A more convenient way is to consider the mass enclosed within a sphere around the center of the halo with radius R_Δ , at which the halo density is Δ times the mean matter density or alternatively the critical density of the Universe:

$$\frac{M_\Delta}{4\pi R_\Delta^3/3} = \Delta \times \bar{\rho}_M, \quad \frac{M_{\Delta,\text{crit}}}{4\pi R_{\Delta,\text{crit}}^3} = \Delta \times \rho_c. \quad (2.22)$$

In most cases, if Δ is sufficiently large, almost all of the mass taken into account is also bound to the halo. A typical choice is $\Delta = 200$. An important quantity one can define is the *concentration* of the halo $c_\Delta \equiv R_\Delta/r_s$, which has been found to depend only weakly on halo mass.

Chapter 3

Dark Energy

We have seen so far that the tempting hypothesis of the vacuum energy being the driver of the late-time accelerated expansion of the Universe suffers of various theoretical and observational problems. This motivates to extend further our investigation on the intrinsic nature of dark energy. One possible, and very reasonable, way that we can undertake is to think of dark energy as an additive component of our Universe described by a scalar field ϕ , associated with a self-interaction potential $V(\phi)$. In this chapter we are going to describe the main features of such component with a particular interest to the (not only gravitational) interactions that may take place between DE and matter.

3.1 Quintessence

A form of dark energy described by a scalar field ϕ with a self-interaction potential $V(\phi)$ that interacts with the other species only through gravity is typically referred to as *Quintessence* [37, 38]. This kind of model is described by the following action, which is a revisited version of the eq. (1.37):

$$S = \int d^4x \sqrt{-g} \left[\frac{1}{2\kappa^2} R + \mathcal{L}_\phi \right] + S_m, \quad (3.1)$$

where $\kappa^2 = 8\pi G$ and we have replaced the cosmological constant with the quintessence scalar field, described by the following Lagrangian:

$$\mathcal{L}_\phi = -\frac{1}{2} g^{\mu\nu} \partial_\mu \phi \partial_\nu \phi - V(\phi). \quad (3.2)$$

From which it follows that, if we consider a FLRW background, the energy density and the pressure of this new fluid will be:

$$\rho_\phi = \frac{1}{2} \dot{\phi}^2 + V(\phi), \quad P_\phi = \frac{1}{2} \dot{\phi}^2 - V(\phi). \quad (3.3)$$

Consequently its equation of state will be given by:

$$w_\phi = \frac{\dot{\phi}^2 - 2V(\phi)}{\dot{\phi}^2 + 2V(\phi)}. \quad (3.4)$$

Unlike for the cosmological constant, the e.o.s. will be $w_\phi \geq -1$ and in general not constant. The evolution of the quintessence scalar field is given by the variation of the action (3.1) with respect to ϕ . This leads to the Klein-Gordon equation:

$$\ddot{\phi} + 3H\dot{\phi} + V_{,\phi} = 0. \quad (3.5)$$

Since we want this field to drive the late-time cosmic acceleration, we must require that, in recent times, $w_\phi < -1/3$, which means that $\dot{\phi}^2 < V(\phi)$. In other words we want the potential shallow enough for the field to evolve slowly along the potential [36]. This mechanism is formally very similar to the one that is thought to have driven the cosmic acceleration during the inflationary period in the very early Universe. So far, several forms for the potential have been proposed in the literature (see e.g. [39, 40, 41, 42, 43]).

Phantom Energy

As it is possible to see in figure 1.2, a DE with equation of state smaller than -1 is not ruled out by the most recent cosmological observations. This kind of DE is usually referred to as *phantom* or *ghost*. The simplest model which realizes $w_\phi < -1$ is a scalar field with a negative kinetic energy [44]. The energy density and pressure in this case will be given by:

$$\rho_\phi = -\frac{1}{2}\dot{\phi}^2 + V(\phi), \quad P_\phi = -\frac{1}{2}\dot{\phi}^2 - V(\phi). \quad (3.6)$$

And the equation of state of the phantom will be given by:

$$w_\phi = \frac{\dot{\phi}^2/2 + V(\phi)}{\dot{\phi}^2/2 - V(\phi)}, \quad (3.7)$$

where we see that one has $w_\phi < -1$ for $\dot{\phi}^2/2 < V(\phi)$. The dynamics of phantom energy has further been studied in works such as [45, 46, 47]. One peculiar feature of this model is that the phantom field rolls *up* the potential because of the negative kinetic energy. Another feature of the phantom is that, for certain choices of the potential (e.g. an exponential function), w_ϕ tends to settle to a constant and < -1 value which results in one of the most extreme scenarios concerning the ultimate fate of our Universe, the so called *Big Rip* [49]. Last but not least, it can be shown, through the study of the phantom Lagrangian, that this model leads to an unstable vacuum state [45, 48]. In order to avoid the catastrophic instability of the vacuum, it is usual to consider theories in which the interaction between ghosts and normal fields is as weak as possible.

3.2 Coupled Quintessence

Unless some symmetry prevents it, the scalar field we have introduced in the previous section is expected to explicitly couple with the ordinary matter present in our Universe, with a strength that could be comparable to gravity [50]. This strong coupling, would have such an impact on the nature of the Universe, that if it had been present we would have already directly detected it. However, we can not exclude, and therefore we must investigate, the presence of a (possibly weaker) non-minimal coupling between DE and matter. Moreover, if DE couples differently with baryons than with DM, as first proposed in [51], the constraints we can put on the strength of the latter coupling become looser [53]. Before we start introducing coupled quintessence models it is important to note that from a mathematical point of view, this coupling is equivalent, via a conformal transformation, to a coupling between quintessence and gravity [52, 55], that leads to modified gravity theories.

We consider a general model in which DE has the same coupling with baryons and DM [53]. Our starting point is the following: since we want the Bianchi identities to hold for the Einstein tensor, the covariant derivative of the total energy momentum tensor must be zero even if we introduce a coupling term (which in general implies $T_{(I)\nu;\mu}^\mu \neq 0$ for a specific component I). Therefore the equations that describe the coupling in our model are the following:

$$T_{(m)\nu;\mu}^\mu = -C(\phi)T_{(m)}\phi_{;\nu}, \quad (3.8)$$

$$T_{(\phi)\nu;\mu}^\mu = C(\phi)T_{(m)}\phi_{;\nu}, \quad (3.9)$$

where the subscripts m and ϕ indicate respectively matter (baryons and DM) and DE, while $C(\phi)$ is the coupling function.

3.2.1 Background Evolution

Using the two equations above, we can now calculate the background equations in a FLRW metric, obtaining:

$$\ddot{\phi} + 3H\dot{\phi} + V_{,\phi} = \sqrt{2/3}\kappa\beta\rho_m, \quad (3.10)$$

$$\dot{\rho}_m + 3H\rho_m = -\sqrt{2/3}\kappa\beta\rho_m\dot{\phi}, \quad (3.11)$$

$$\dot{\rho}_\gamma + 4H\rho_\gamma = 0, \quad (3.12)$$

$$3H^2 = \kappa^2(\rho_\gamma + \rho_m + \rho_\phi), \quad (3.13)$$

where we have also taken into account the radiation with subscript γ and we have introduced $\beta = C\sqrt{\frac{3}{2\kappa^2}}$. Integrating the matter continuity equation we get

$$\rho_m = \rho_{m,0}a^{-3}e^{-\sqrt{\frac{2}{3}}\kappa\int\beta(\phi)d\phi}, \quad (3.14)$$

which is one of the fundamental characteristics of the coupled DE models: matter density is no more conserved since an energy exchange is taking place between matter and DE. Moreover, if we assume that the number density of matter particles is conserved in time, from the previous equation we obtain that the mass of the coupled matter particles evolves in time depending on the scalar field:

$$M(a) = M(a_0)e^{-\sqrt{\frac{2}{3}}\kappa \int \beta(\phi) d\phi}. \quad (3.15)$$

For what concerns the potential of the scalar field we have that a possible, and extensively studied, choice is a generic exponential function:

$$V(\phi) = Ae^{-\kappa\sqrt{2/3}\alpha\phi}. \quad (3.16)$$

From now on we will make the above assumption. For convenience, let us define the following dimensionless variables:

$$x \equiv \frac{\kappa}{\mathcal{H}} \frac{\phi'}{\sqrt{6}}, \quad y \equiv \frac{\kappa}{H} \sqrt{\frac{V(\phi)}{3}}. \quad (3.17)$$

3.2.2 Linear Perturbations

Before computing the linear perturbation equations, let us define the dimensionless scalar mass as:

$$\hat{m}_\phi^2 \equiv \frac{m_\phi^2}{H^2} = \frac{1}{H} \frac{d^2V(\phi)}{d\phi^2}, \quad (3.18)$$

then, after having defined the perturbation of the scalar field as $\varphi = \kappa\delta\phi\sqrt{6}$, we can write the perturbed matter and scalar field equations (see [54, 57, 58] for a complete derivation):

$$\delta' = -\theta + 3\Phi' - 2\beta\varphi' - 2\varphi\beta', \quad (3.19)$$

$$\theta' = -(1 - 2\beta x)\mathcal{H}\theta + k^2(\Phi - 2\beta\varphi), \quad (3.20)$$

$$\begin{aligned} \varphi' + 2\mathcal{H}\varphi' + \left(k^2 + \mathcal{H}^2\hat{m}_\phi^2 - \frac{\mathcal{H}\Omega_m\beta'}{x} \right) \varphi \\ - 4\mathcal{H}x\Phi' - 2\mathcal{H}^2y^2\alpha\Phi = \mathcal{H}^2\beta\Omega_m(\delta + 2\Phi). \end{aligned} \quad (3.21)$$

It is interesting to observe that in case the coupling is not constant, there is an additional term in eq (3.21) that contributes for the scalar field fluctuations, this can be interpreted as an effective coupling mass:

$$\hat{m}_\beta^2 \equiv \frac{\Omega_m\beta'(\phi)}{\mathcal{H}x}. \quad (3.22)$$

In this way we can introduce the effective mass that will be useful in a moment.

$$\hat{m}^2 \equiv \frac{m^2}{H^2} = \hat{m}_\phi^2 + \hat{m}_\beta^2. \quad (3.23)$$

We now consider the Newtonian limit (small scales $\lambda \ll 1$, where $\lambda \equiv \mathcal{H}/k$), which is the one relevant for N-body simulations. Furthermore we assume that λ^2 is not much larger than \hat{m}^2 . With the above assumptions, it can be shown that:

$$\varphi \approx Y(k)\lambda^2\beta\Omega_m\delta, \quad (3.24)$$

where:

$$Y(k) = \frac{k^2}{k^2 + a^2m^2}, \quad (3.25)$$

where $m = \hat{m}H$. We now substitute in eq. (3.20) to obtain the effective potential:

$$\hat{\Phi} = -\frac{3}{2}\lambda^2\Omega_m\delta \left[1 + \frac{4}{3}\beta^2Y(k) \right]. \quad (3.26)$$

From eq. (3.15) we can express the effective mass of a matter particle of mass $M_0 = M(a_0)$ as:

$$\tilde{M} = M_0 e^{-\sqrt{\frac{2}{3}}\kappa \int \beta d\phi}. \quad (3.27)$$

At this point it is possible to show that, anti-Fourier transforming eq. (3.26), the effective potential in real space at a distance r from an individual coupled massive particle can be written as:

$$\tilde{\Phi}(r) = -\frac{G\tilde{M}}{r} \left(1 + \frac{4\beta^2}{3}e^{-mr} \right), \quad (3.28)$$

where we see that, in the presence of a coupling, the gravitational potential takes the form of the Yukawa potential. We can also define the effective gravitational constant:

$$\tilde{G} = G \left[1 + \frac{4\beta^2}{3}(1 + mr)e^{-mr} \right], \quad (3.29)$$

and the parameter:

$$\tilde{H} = H(1 - 2\beta x), \quad (3.30)$$

so that we can finally write the Newtonian limit for the gravitational acceleration felt by the i -th particle in an ensemble of N particles:

$$\dot{v}_i = -\tilde{H}v_i - \frac{d\tilde{\Phi}}{dr_i} = -\tilde{H}v_i - \frac{\tilde{G}\tilde{M}}{r^2}. \quad (3.31)$$

From this equation we can clearly see that the well-known gravitational acceleration equation is modified by the coupling in three ways:

- The usual friction Hv is modified by an additional friction term $-2\beta x$. This effect does not depend only on the intensity of the coupling, but also on the term x , which is the kinetic energy of the scalar field. Thanks to the dependence on x , it can be shown that the usual friction is more strongly modified, the more the equation of state of dark energy w_ϕ differs from -1 .
- The mass M of a generic particle is modified by the factor $e^{-\sqrt{\frac{2}{3}}\kappa \int \beta d\phi}$. This effect impacts the gravitational potential, generated by the matter distribution, so that it not only changes in time according to the dynamics of the matter particles but also due to the evolution of the scalar field.
- The gravitational constant G is now modified by a term that takes into account the Yukawa correction for the potential. This term depends on the mass m associated with the scalar field plus the coupling. In the case m is negligible there is still a modification of G but the behavior this time is the one of an additional long-range fifth force.

3.2.3 Consequences of Coupling

The presence of coupling between DE and matter can significantly influence the evolution of the Universe. One of the most relevant features is the presence of an intermediate epoch, usually referred as field-matter-dominated-era (ϕ MDE), between the radiation era and the accelerated era during which the two coupled fluids maintain a constant ratio of energy densities (see figure 3.1). Indeed, it can be shown [58] that in the ideal case of a Universe made only of matter and DE, whose coupling strength is described by β , the energy density Ω_ϕ of the field during ϕ MDE is given by:

$$\Omega_\phi(\phi MDE) = \frac{4}{9}\beta^2. \quad (3.32)$$

During this era the fluctuations grow less than in the correspondent uncoupled model. The ϕ MDE has three effects on the CMB: a tilt of the spectrum at low multipoles, due to the ISW effect [56]; a shift to higher multipoles of the acoustic peaks, due to the change in the sound horizon; and a change in their amplitude. On the other hand the main effect on the power spectrum is a reduction of σ_8 for large couplings [53].

3.3 Dark Scattering

Dark Scattering is a particular type of coupled quintessence that was introduced in [60] and further studied in [61, 62]. This model assumes Cold Dark Matter to be the only component to have a non-minimal interaction with dark energy, furthermore this interaction can be described as a pure momentum exchange, i.e. with no transfer of rest-mass energy between the two components, modulated by its characteristic cross section. The basic idea is that, at energies that are sufficiently low,

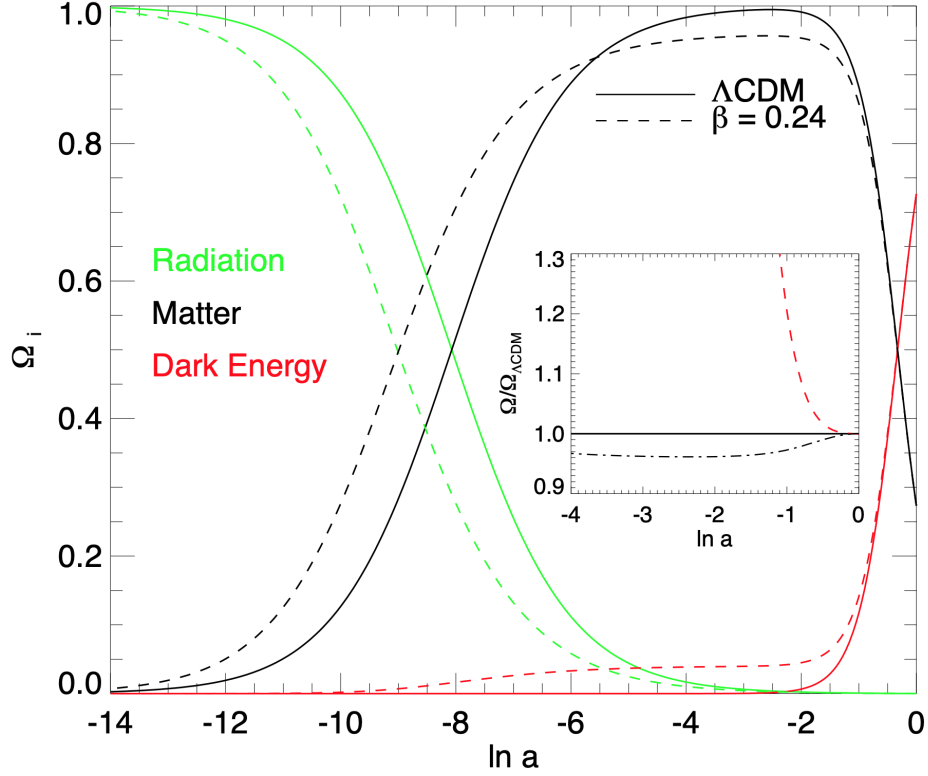


Figure 3.1: Background evolution of a standard Λ CDM model (solid lines) and a coupled model with $\beta = 0.24$ (dashed lines). In figure is shown the evolution of the dimensionless density in radiation (green), matter (black) and DE (red) as a function of $\ln a$ (known as *e-folding time*). The smaller plot shows the ratio of the same quantities to the Λ CDM case. We can see that the coupled case gives place to the ϕ MDE era, during which the two coupled fluids share a constant ratio of the total energy budget of the Universe. The figure is taken from [59].

the interactions between particles can be modeled as a process of elastic scattering. Two remarkable examples present in nature are Thomson scattering and Rayleigh scattering. Let us consider a CDM particle moving through the DE isotropic fluid with equation of state w_ϕ and stress tensor $T_{ab} = \text{diag}(\rho_\phi, w_\phi \rho_\phi, w_\phi \rho_\phi, w_\phi \rho_\phi)$. We have that, if $w_\phi \neq -1$, the particle experiences a momentum flux that imparts a force proportional to the cross section σ_c . It can be shown [61, 63] that the four-force is given by:

$$g^\mu = (\gamma \mathbf{f} \cdot \mathbf{v}, \gamma \mathbf{f}), \quad (3.33)$$

where γ is the Lorentz factor and:

$$\mathbf{f} = -(1 + w_\phi) \sigma_c \gamma^2 \rho_\phi \mathbf{v}. \quad (3.34)$$

As said previously, a classical example is the Thomson scattering which takes place between photons and non-relativistic electrons, described by the force:

$$F = -\frac{4}{3}\sigma_t v \rho_\gamma, \quad (3.35)$$

where σ_T is the well known Thomson cross section.

One distinctive feature of this models is that this kind of interaction does not affect the background evolution of the Universe due to the absence of any rest-energy transfer.

3.3.1 Linear Perturbations

The perturbed equations, in terms of the cosmic time t , for the DE and CDM fluids are the following:

$$\begin{aligned} \dot{\delta}_\phi = & - \left[(1 + w_\phi + 9\frac{H^2}{k^2}(1 - w_\phi^2)) \right] \theta_\phi \\ & + 3(1 + w_\phi)\dot{\Phi} - 3H(1 - w_\phi)\delta_\phi, \end{aligned} \quad (3.36)$$

$$\dot{\delta}_c = -\theta_c + 3\dot{\Phi}, \quad (3.37)$$

$$\dot{\theta}_\phi = 2H\theta_\phi - an_D\sigma_c\Delta\theta + k^2 \left(\Phi + \frac{\delta_\phi}{1 + w_\phi} \right), \quad (3.38)$$

$$\dot{\theta}_c = -H\theta_c + \frac{\rho_\phi}{\rho_c}(1 + w_\phi)an_D\sigma_c\Delta\theta + k^2\Phi. \quad (3.39)$$

Here $\Delta\theta = \theta_\phi - \theta_c$, n_D is the proper number density of CDM particles and we used the subscript c to indicate CDM. We see that with respect to the coupled quintessence models, we are left only with one distinctive feature: the extra Hubble-friction term. As done previously, let us write the acceleration felt by a CDM particle of mass M_c in the Newtonian limit. In doing so, we assume DE sound speed to be $c_s = 1$, this is provided by most of DE models based on light scalar fields. With this assumptions one has that DE perturbations at sub-horizon scales are damped, so that it is possible to take $\delta_\phi = \theta_\phi = 0$, as verified numerically in [61]. We get to the following equation:

$$\dot{v}_i = -[1 + A]Hv_i - \frac{d\Phi}{dr_i}, \quad (3.40)$$

where the additional scattering term is defined as follows:

$$A \equiv (1 + w_\phi)\sigma_c \frac{c}{M_c} \frac{3\Omega_{DE}}{8\pi G} H. \quad (3.41)$$

We see that the extra term depends on the CDM particle mass M_c , the DE equation of state parameter w_ϕ and the scattering cross section σ_c . It is evident that in the case $w_\phi = -1$ one has $A = 0$, in other words: the Cosmological Constant can not scatter off matter particles.

In [60], the author performed a linear analysis of the growth factor γ , defined as:

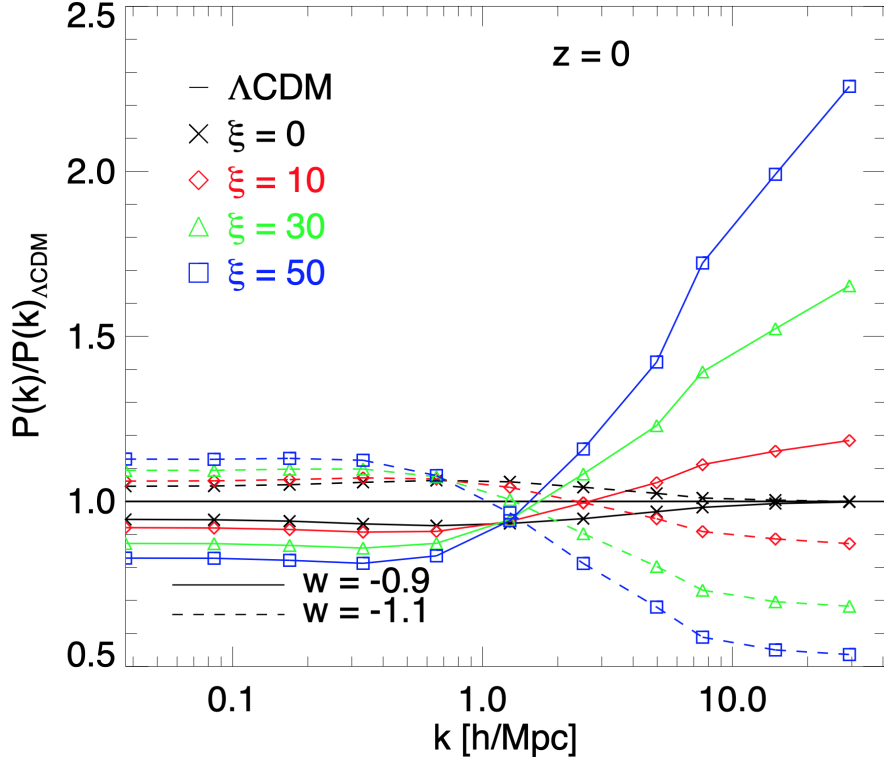


Figure 3.2: Matter power spectrum ratio of the different models versus the reference Λ CDM. model. The different line styles refer to $w_\phi = -0.9$ (solid) and $w_\phi = -1.1$ (dashed). The different colors refer to different intensities of the dark scattering, modulated by the parameter ξ . It is possible to see that for each model, the nonlinear effects of the scattering are opposite, and eventually stronger, with respect to the linear ones. The figure is taken from [61].

$$\gamma = \frac{d \ln f}{d \ln \Omega_m}, \quad (3.42)$$

with $f \equiv d \ln \delta / d \ln a$. Starting from equations (3.36-3.39), the results are the following: if $w_\phi > -1$, the extra velocity-dependent term has the effect of slightly suppressing the growth of structure, the contrary happens in the case $w_\phi < -1$, in which the growth of structure is slightly enhanced. We stress that this results hold as long as we are in the linear regime.

3.3.2 Dark Scattering Simulations

To study the effects of dark scattering in the nonlinear regime it is necessary to perform N-body simulations. In [61] the authors performed high resolution dark scattering CDM-only simulations using a modified version of the `GADGET-3` code [68, 70] (we are going to describe this code in the next section) which implements the extra velocity-dependent term (3.41). The equation (3.40) has been implemented in the code to describe the acceleration of the CDM particles in a system

of N particles. In this case, it can be written as:

$$\dot{v}_i = -[1 + A]Hv_i + \sum_{j \neq i} \frac{Gm_j \mathbf{r}_{ij}}{|\mathbf{r}_{ij}|^3}. \quad (3.43)$$

To modulate the intensity of the scattering, the parameter $\xi \equiv c \cdot \sigma_c / M_c$ has been introduced, so that the extra term (3.41) is:

$$A = (1 + w_\phi) \frac{3\Omega_{\text{DE}}}{8\pi G} H\xi. \quad (3.44)$$

The simulations have taken into account three possible constant values for w_ϕ : -1 (Cosmological Constant), -0.9 (quintessence-like) and -1.1 (phantom-like). For each of the cases with $w_\phi \neq -1$ four simulations had been performed, respectively with $\xi = [0, 10, 30, 50] \text{ bn} \cdot c^3/\text{GeV}$. The results of these simulations are of particular interest for us: at nonlinear scales the trend of the growth of structures is the opposite of the linear one. More precisely, in the case $w_\phi = -0.9$, the extra term acts as a friction which is in opposition to the formation of structures as long as the velocity of the particles is aligned with the gradient of the gravitational potential (as it is for the linear regime), but when this condition is no more satisfied (i.e. in the nonlinear regime) the same friction shall facilitate gravitational collapse since it results in the decrease of particles angular momentum. The exact opposite happens for $w_\phi = -1.1$: in this case dark scattering acts as an additional drag which helps the collapse of the particles onto the forming structures in the linear regime, but increases particles angular momentum in the nonlinear regime. What we said can be steadily visualized in figure 3.2, in which one can see the ratio of the power spectrum, at $z = 0$, of each simulation over the ΛCDM one. One can also notice that the nonlinear effects can be significantly larger than the linear ones.

3.4 DE-Baryon Scattering

More recently (see [64]), a new model has been introduced, motivated by the following: what if dark energy is exchanging momentum exclusively with baryonic matter? This question has been posed in order to assess whether it would be possible to investigate this interaction through cosmological observables, such as the CMB temperature anisotropy power spectrum or the matter power spectrum.

3.4.1 Linear Perturbations

In the case of scattering between DE and baryons, the linear perturbation equations are the same as the dark scattering ones, but referred to the baryonic matter,

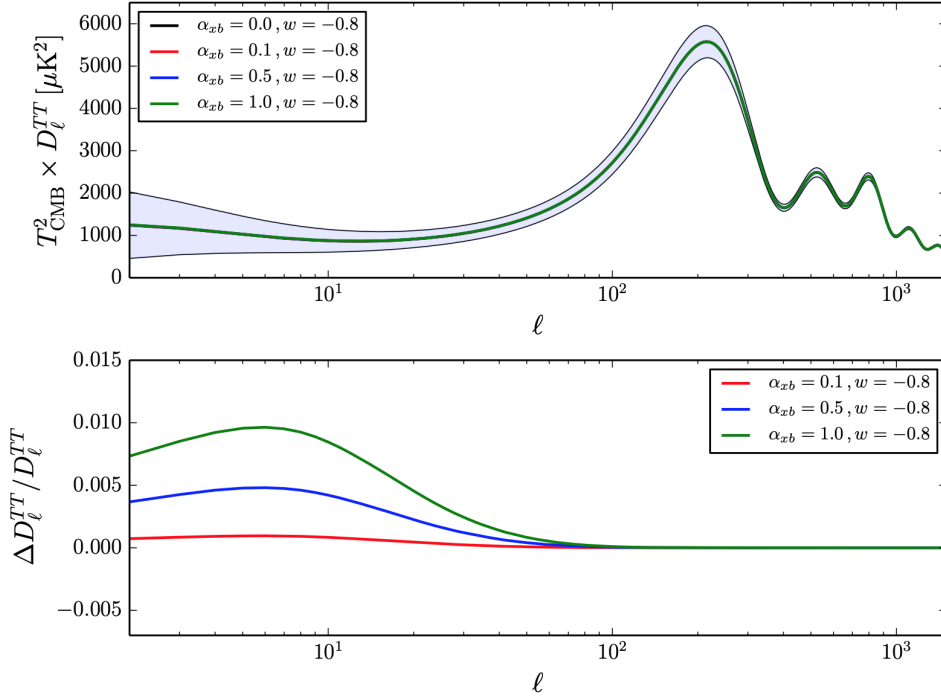


Figure 3.3: CMB temperature power spectrum for increasing α_{xb} (ratio between the DE-baryon scattering cross-section to the Thomson cross-section). Upper panel: CMB temperature anisotropy power spectra for $\alpha_{xb} = 0$ (black curve), 0.1 (red curve), 0.5 (blue curve), and 1.0 (green curve). Lower panel: relative change in power with respect to the model with $\alpha_{xb} = 0$. The light blue band indicates the uncertainty caused by the cosmic variance. The figure is taken from [64].

for which we use the subscript b :

$$\begin{aligned} \dot{\delta}_\phi = & - \left[(1 + w_\phi + 9 \frac{H^2}{k^2} (1 - w_\phi^2)) \right] \theta_\phi \\ & + 3(1 + w_\phi) \dot{\Phi} - 3H(1 - w_\phi) \delta_\phi, \end{aligned} \quad (3.45)$$

$$\dot{\delta}_b = -\theta_b + 3\dot{\Phi}, \quad (3.46)$$

$$\dot{\theta}_\phi = 2H\theta_\phi - an_e\sigma_c\Delta\theta + k^2 \left(\Phi + \frac{\delta_\phi}{1 + w_\phi} \right), \quad (3.47)$$

$$\dot{\theta}_b = -H\theta_b + \frac{\rho_\phi}{\rho_b} (1 + w_\phi) an_e\sigma_b\Delta\theta + k^2\Phi, \quad (3.48)$$

where this time $\Delta\theta = \theta_\phi - \theta_b$. Since we know that baryons are already involved in a remarkable scattering process with photons, that is the Thomson scattering, which is described by its related cross section¹ $\sigma_T \approx 6.7 \cdot 10^{-25} \text{ cm}^2 = 0.67 \text{ bn}$, it is useful to introduce the *Thomson Ratio*: $\alpha \equiv \sigma_b/\sigma_T$ to measure the intensity of

¹bn is the barn measurement unit: $1 \text{ bn} = 10^{-24} \text{ cm}^2$.

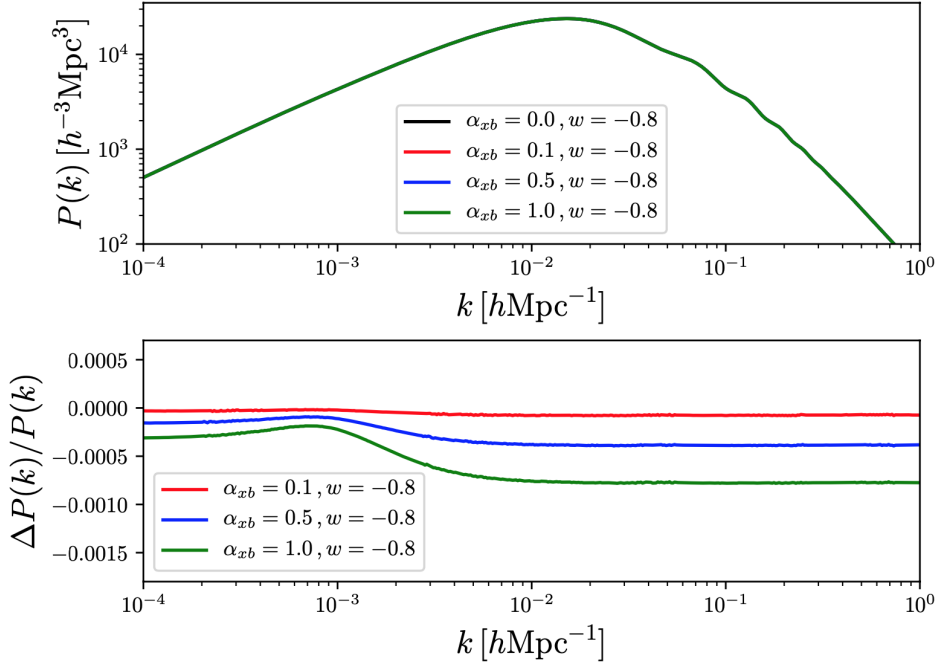


Figure 3.4: As in Fig. 3.3 but referring to the matter power spectrum at redshift $z = 0$. The small decrease in power at every scales is due to the effect of the extra velocity-dependent term brought by the DE-baryon scattering. The figure is taken from [64].

the scattering. We can rewrite eq (3.41) to describe the acceleration of a baryonic particle of mass M_b :

$$\dot{v}_i = -[1 + B]Hv_i - \frac{d\Phi}{dr_i}, \quad (3.49)$$

where the additional scattering term is now:

$$B \equiv (1 + w_\phi)\alpha \frac{c\sigma_T}{M_b} \frac{3\Omega_{DE}}{8\pi G} H. \quad (3.50)$$

This relation will be useful later, when we will describe the numerical implementation of DE-baryon scattering models.

In [64] the authors modified the CAMB code [67] in order to integrate the system of equations (3.45-3.48) and compute the linear prediction for the CMB Temperature power spectrum and the matter power spectrum. As one can see from eq (3.50), the more w_ϕ differs from -1 , the more the effects of the scattering become significant. So, to enhance the effects as much as possible, they investigated two models with a constant and "extreme" value for the DE equation of state: $w_\phi = -0.8$ and $w_\phi = -1.2$. Surprisingly, they found that, even for very large values of α (e.g. $\alpha \gtrsim 10$), both the cosmological observables mentioned above are essentially left unaltered, as one can see in fig. 3.3 and 3.4. It is important

to stress that this result holds for linear scales, and it is likely that the effects at nonlinear scales might be stronger than the linear ones, analogously with the findings of the dark scattering simulations performed in [61, 62]. For this reason, in this work, we are going to perform for the first time in the literature N-body, multi-particle, structure formation simulations in which DE-baryon scattering is implemented.

3.4.2 Screening the Interaction at Small Scales

Before we introduce the numerical implementation and the simulations in the next chapter, let us briefly comment the behaviour of the interaction on the smallest scales (see [65]). As mentioned in section 3.2, the constraint we can put on the coupling between DE and baryons is much tighter than the one we can put on DE-DM coupling. This is because of the high precision with which we are able to investigate the interactions of baryonic matter in solar system observations as well as in laboratory experiments. For this reason, models in which DE is coupled with baryons typically include a mechanism that makes the coupling vanish at small scales (see e.g. [66]). In this context, we can note that in eq. (3.48), the term related to DE-baryon scattering scales as ρ_b^{-1} , thus making the interaction decrease in regions where the baryonic density is higher. By the way we cannot use these argument to exhaustively solve the screening question: it is not correct to extrapolate this linear relation to highly nonlinear scales, also because some of our hypothesis (e.g. considering baryons as a perfect fluid) cease to be true at these scales. Therefore the only constraints we can put right now on DE-baryon scattering must come from the cosmological framework, this makes even clearer the motivation to perform cosmological simulations that include DE-baryon scattering. As a final note, we observe that in principle numerical simulations of DE-baryon scattering should also include the screening mechanism mentioned above. In the present work we are not including this feature for simplicity, but we leave such implementation for future work.

Chapter 4

Numerical Implementation

As we can conclude from the previous chapter, the nonlinear effects of DE-baryon scattering could be greater than the linear ones. It is therefore crucial to run dedicated N-body simulations to shed more light on the effects of this interaction on a broader range of spatial scales. In this chapter we are going to outline the framework and the details of our numerical experiments on DE-baryon scattering.

4.1 The GADGET Code

The code we used to perform our simulations is the `C-GADGET` code. This is a modified version of the `GADGET-3` code, which is in turn one of the latest updates of the `GADGET` code [68, 70], originally developed by Volker Springel. Even if there are clearly some differences between the various versions, the strategies used to solve the equations of gravity and hydrodynamics remain quite similar. In This section we are going to describe the main features of the `GADGET` code(s) and the modifications we have done in order to implement the effects of DE-baryon scattering.

4.1.1 Collisionless Dynamics

As long as we ignore the effects of hydrodynamics, we can model our system as a self-gravitating collisionless fluid, governed by the *collisionless Boltzmann equation* (CBE):

$$\frac{df}{dt} \equiv \frac{\partial f}{\partial t} + \mathbf{v} \frac{\partial f}{\partial \mathbf{x}} - \frac{\partial \Phi}{\partial \mathbf{r}} \frac{\partial f}{\partial \mathbf{v}} = 0, \quad (4.1)$$

where $f(\mathbf{r}, \mathbf{v}, t)$ is the mass density in the single-particle phase space and the potential is sourced by the well known Poisson equation:

$$\nabla^2 \Phi(\mathbf{r}, t) = 4\pi G \int f(\mathbf{r}, \mathbf{v}, t) d\mathbf{v}. \quad (4.2)$$

The N-body approach to this coupled system of equations models the fluid as made of a finite number of particles, which are integrated along the characteristic curves of the CBE. It is of primary importance to have a sufficiently high number of particles in order to obtain a reliable simulation. The N-body problem basically consists in solving Newton's equations of motion for a large number of particles under their own self gravity. At this point we stress that in our numerical treatment of such equations it is necessary to introduce a softening ϵ_g for the gravitational force in order to avoid large-angle scattering in two-body collisions. The equation of gravity then becomes:

$$\Phi(\mathbf{x}) = -G \sum_{j=1}^N \frac{m_j}{[(\mathbf{x} - \mathbf{x}_j)^2 + \epsilon_g^2]^{1/2}}, \quad (4.3)$$

so that we are actually introducing a lower cut-off in the spatial resolution. For what concerns the boundary conditions, the code offers the possibility to use periodic boundaries, this is a typical choice when performing cosmological simulations and is the one we will adopt, moreover we will use a comoving system of coordinates, so that the real dimension of our box will naturally follow the Hubble expansion. Finally we point out that the `GADGET` code also offers the possibility to include the gasdynamics for the baryonic particles, however we will not describe this in detail since in the present work we are limiting to treat baryons as a collisionless fluid. This choice of approximation is justified by the fact that in this work, where DE-baryon scattering is implemented numerically for the first time, we want to focus our attention on the effects of the interaction alone, without the complication of disentangling additional effects acting on baryons. In this context and with this purpose, baryons can be fairly included as a collisionless component. We leave for future work to run hydrodynamical simulations which are comprehensive of DE-baryon scattering.

4.1.2 The Tree Algorithm

The method used by the code to compute the gravitational force exerted on a specific particle by all the particles enclosed within a certain range with arbitrary spatial resolution is the so-called *Tree* algorithm, which is based on a hierarchical multipole expansion. The basic idea of this method is that a group of particles that is distant enough from the particle for which we are computing the force can be treated as one massive particle (its mass being the sum of the masses of the particles of the group) centered in the centre of mass of the group, in other words we are performing a monopole expansion on sufficiently distant groups. It is evident that in this way we will not need to do $N - 1$ partial force computations per particle (with N being the total number of particles), instead the force computation for a single particle will require $O(\log N)$ operations (see [71]). The total computational cost therefore scales from $O(N^2)$ to $O(N \log N)$. From a practical point of view we want a method to hierarchically pack up the particles, so that we start from the biggest groups and we can gradually unpack them until we

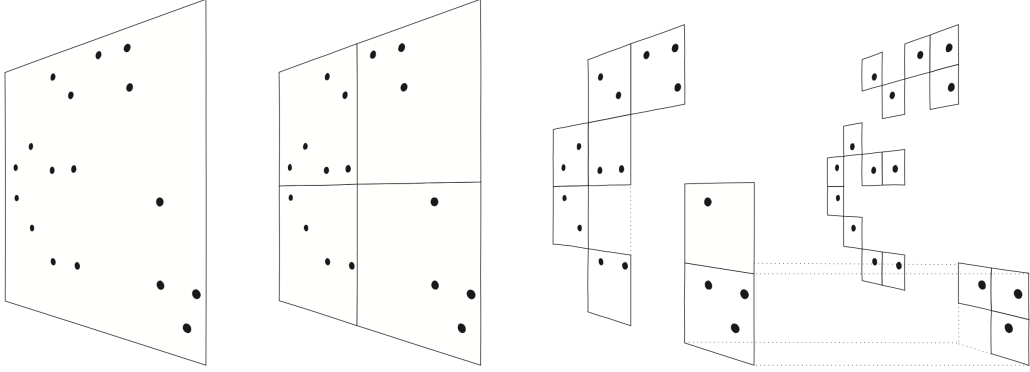


Figure 4.1: Scheme of 2-D version of the oct-tree algorithm proposed in [72]. We start (left) with a square node that encloses all the particles, this is then iteratively subdivided into 4 child until every child node contains at most one particle (right). Note that empty squares do not need to be stored. This figure is taken from [68].

reach the desired precision. This can be done in terms of a recursive subdivision of space [72]: one starts from a cubical root node which includes the totality of the particles, from this cube are then generated eight daughter nodes, and this process is repeated iteratively for each one of the generated nodes that contain two or more particles. For a better understanding, the 2-D version of a hierarchical tree can be visualized in fig. 4.1. Once the tree structure is created, the force can be computed by "walking" the tree: starting from the root node, every time one encounters a cube that, if considered as a whole, is not able to provide sufficient accuracy in the force computation, this is "opened" and each one of the daughter nodes is subject to the above accuracy test. The final result of the Tree algorithm will be an approximated version of the true gravitational force, however the accuracy of the method can be well modulated by the following node-opening criterion:

$$\frac{GM}{r^2} \left(\frac{l}{r} \right)^2 \leq \alpha |\mathbf{a}|, \quad (4.4)$$

where M , l and r are respectively the total mass, the extension and the distance of the node considered, $|\mathbf{a}|$ is the magnitude of the acceleration obtained in the last timestep and α is the tolerance parameter used to set the precision.

4.1.3 The Particle Mesh (PM) Method

An alternative way to solve the equations of gravity is represented by the so-called *Particle Mesh* (PM) method, which is even faster than the Tree algorithm, though less accurate on the computation of short range forces. We start pointing out that gravitational potential can be expressed as the convolution of the density field $\rho(\mathbf{x})$ with a Green's function $g(\mathbf{x})$:

$$\Phi(x) = \int g(\mathbf{x} - \mathbf{x}')\rho(\mathbf{x}) d\mathbf{x}'. \quad (4.5)$$

The usefulness of such expression of the gravitational potential becomes evident if we consider the same relation in the Fourier space:

$$\Phi_{\mathbf{k}} = g_{\mathbf{k}} \cdot \rho_{\mathbf{k}}. \quad (4.6)$$

So if we compute the Fourier transform of the density field, we just need to perform a multiplication, rather than an integration, with the Fourier transform of the Green's function. In practice we start by assigning a cubic Cartesian grid to the space, so that we can compute the density of each grid cell starting from the particles that this cell contains (possibly considering a more complex shape function for the particles rather than the Dirac's delta), we can then Fourier transform this continuous-like density field and multiply it with the Fourier transform of the Green's function to obtain the potential in the Fourier space. Last but not least we perform the inverse Fourier transform of the potential in order to come back to the real space; we can now compute the gradient of the potential at the particles position to obtain the force acting on each of them. It can be shown that the complexity of this method scales as $O(N)$. On the other hand, the main disadvantage is that, since we Fourier transform sampling on a mesh with finite resolution, we lose all the information on the scales that are smaller than the cells, in other words the spatial resolution of the method is limited to the mesh size.

4.1.4 The TreePM Algorithm

With the introduction of **GADGET-2**, a new algorithm for the computation of the gravitational force has been adopted instead of the pure Tree algorithm. This is the so-called *TreePM* algorithm [73], this hybrid method consists in a synthesis of the Particle Mesh method and the Tree algorithm explained above. We start from observing that the gravitational potential can be explicitly split in Fourier space into a long-range and a short-range term as follows:

$$\Phi_{\mathbf{k}} = \frac{4\pi G}{\mathbf{k}^2} \rho_{\mathbf{k}} = \Phi_{\mathbf{k}}^{\text{long}} + \Phi_{\mathbf{k}}^{\text{short}}, \quad (4.7)$$

with the two components of the potential being defined by the following:

$$\Phi_{\mathbf{k}}^{\text{long}} = \Phi_{\mathbf{k}} \exp(-\mathbf{k}^2 r_s^2), \quad \Phi_{\mathbf{k}}^{\text{short}} = \Phi_{\mathbf{k}} [1 - \exp(-\mathbf{k}^2 r_s^2)], \quad (4.8)$$

where r_s is the distance at which the force is split. The short range potential can be brought back to the real space anti-Fourier transforming the second of the above equations. We obtain:

$$\Phi^{\text{short}}(r) = -\frac{Gm}{r} \operatorname{erfc}\left(\frac{r}{2r_s}\right), \quad (4.9)$$

where erfc is the *complementary error function*, defined in terms of the *error function* erf as:

$$\operatorname{erfc}(z) = 1 - \operatorname{erf}(z) = 1 - \frac{2}{\sqrt{\pi}} \int_0^z e^{-t^2} dt. \quad (4.10)$$

Eq. (4.9) can be solved by means of the ordinary Tree algorithm except that the force law is modified by a short-range cut-off factor. For what concerns the long range potential, this can be computed in a very efficient way with the Particle Mesh (PM) method. To persuade the reader of the reliability of this method, we show in figure 4.2 the spatial decomposition of the force and the error of the TreePM method, which is found to remain under the 1 – 2%.

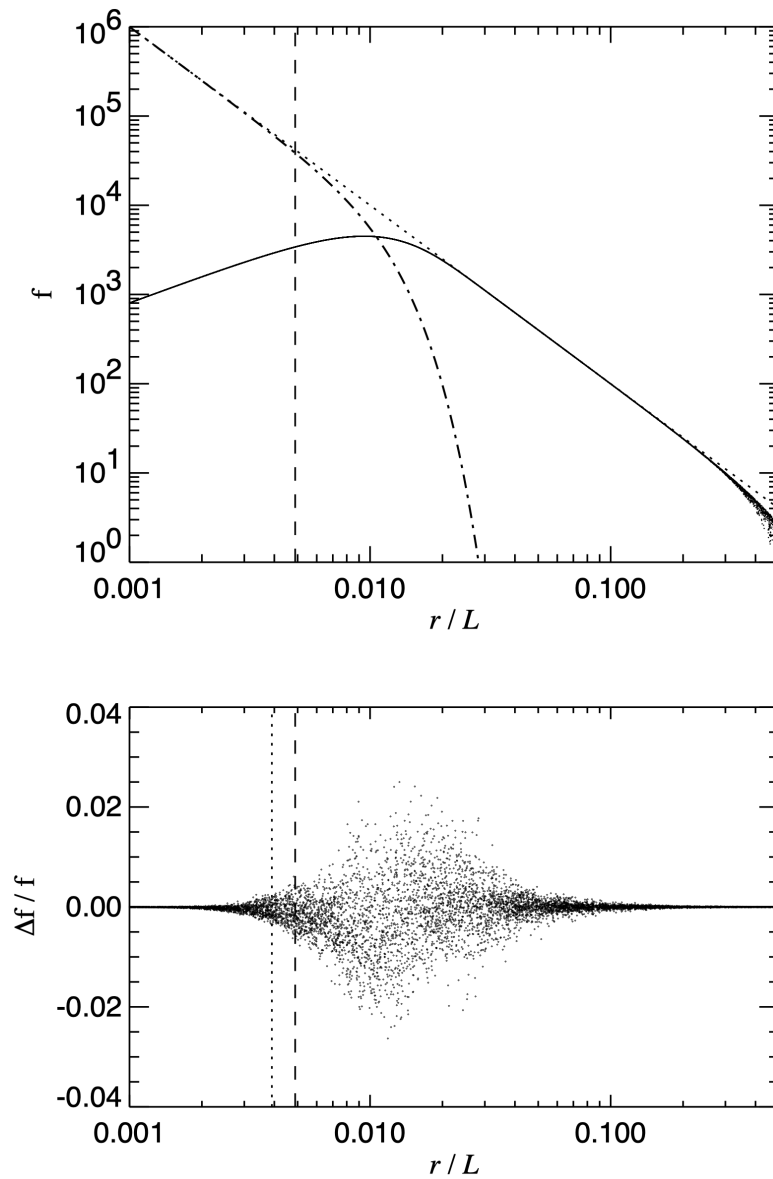


Figure 4.2: Force decomposition and force error of the TreePM scheme. In the upper panel is shown the size of the short-range (dot-dashed) and long-range force (solid) as a function of distance in a periodic box. The spatial scale r_s of the split is marked with a vertical dashed line. In the lower panel the TreePM force with the exact force expected in a periodic box are compared. For separations of order the mesh scale (vertical dotted line), maximum force errors of 1 – 2% due to the mesh anisotropy arise, but the rms force error is well below 1% even in this range, and the mean force tracks accurately the exact solution. This figure is taken from [70].

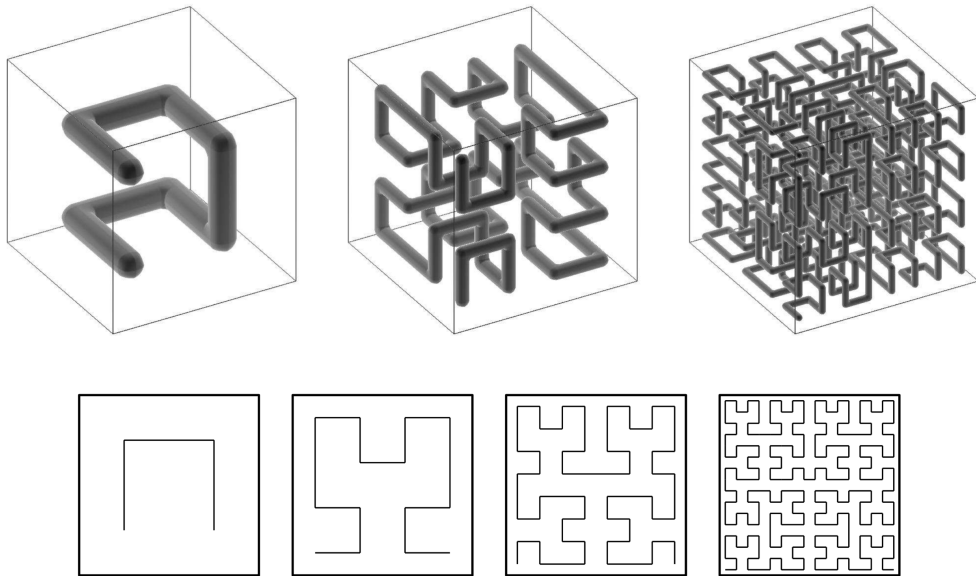


Figure 4.3: Space-filling Peano-Hilbert curve in two (bottom) and three (top) dimensions. This figure is taken from [70]

4.1.5 Parallelization strategies

The only way to perform high resolution N-body simulations efficiently is to leverage the power of parallel high performance computing. Indeed the `GADGET` code is equipped with a brilliant domain decomposition strategy: the 3D computational domain is mapped onto a 1D Peano-Hilbert space filling curve. This curve is visible in figure 4.3 in its 3D and 2D version. Once the curve is built for the domain, it is chopped in pieces of equal length which are distributed among the processors. For what concerns our domain decomposition, the most important property of the Peano-Hilbert mapping is the similarity preservation: points that are close in space, will be also close in the respective Peano-Hilbert curve. In this way one can be sure that the exchange of information between different processors is minimized. Furthermore the domain decomposition is not the only part of the code to employ parallel computing, in fact, the Fourier transform are operated by means of the parallel version of the FFTW library [74].

4.2 Implementation of DE-Baryon Scattering

We now describe the modification we have applied to the `GADGET-3` code in order to implement the scattering between DE and baryons. Let us start from the equation describing the gravitational acceleration of a matter particle in the Newtonian limit, which is the one implemented in the standard code:

$$\dot{v}_i = -Hv_i - \frac{d\Phi}{dr_i}. \quad (4.11)$$

As we have seen in the previous chapter, if we introduce scattering between DE and baryons, the only effect that arises from linear perturbation theory is a modification of the above equation, when referred to baryonic particles. Indeed we have:

$$\dot{v}_i = -[1 + B]Hv_i - \frac{d\Phi}{dr_i}, \quad (4.12)$$

where the extra term B is given by:

$$B = (1 + w_\phi)\alpha \frac{c\sigma_T}{M_b} \frac{3\Omega_{\text{DE}}}{8\pi G} H. \quad (4.13)$$

In practice, if we want to implement DE-baryon scattering, we have to compute B at every timestep and include it when calculating the gravitational acceleration of the baryonic particles. We see that B depends on many constant and non constant terms.

4.2.1 Constant Terms

The fundamental constants such as c or G are already included in `GADGET` and can be found in the `allvars.h` header file. Then there are the two terms M_b and $\alpha = \sigma_b/\sigma_T$, the former being a constant term indicating a characteristic mass for the baryonic particles and the latter being the intensity of the scattering which in the present modification is assumed to be constant (an implementation for time dependent σ_b could be developed in future works). These two terms are sourced from the parameter file of the `GADGET` code, in which we have introduced the two extra parameters `BaryonParticleMass` and `BaryonScatteringCrossSection` which indicate respectively M_b in GeV/c^2 and σ_b in bn .

4.2.2 Time dependent Terms

The last three terms we have to deal with are the time dependent ones: w_ϕ , Ω_{DE} and H . These are connected by the Friedmann equations, in fact, from equations (1.17) and (1.18), one obtains the evolution of the Hubble parameter as a function of redshift (or equivalently of the scale factor a), of the present day density parameters and of the DE equation of state. For a flat Universe we have:

$$H^2(z) = H_0^2 \left[\Omega_{\gamma,0}(1+z)^4 + \Omega_{m,0}(1+z)^3 + \Omega_{\text{DE},0} \exp \left\{ \int_0^z \frac{3(1+w_\phi)}{1+\tilde{z}} d\tilde{z} \right\} \right], \quad (4.14)$$

where the subscript 0 indicates the present day values as usual. Starting from this equation, we wrote a `python` script that produces a table which contains the values of H , Ω_{DE} and w_ϕ for different values of z , once the present day value as well as a

functional form for w_ϕ are given. For what concerns the modification of `GADGET`, we introduced in the parameter file the `DarkEnergyFile` parameter, which contains the path to the formatted text file including the table described above. Once the external table is loaded from the external file, this is converted into an internal table which has a precise (and sufficiently large) number of logarithmically spaced steps of the scale factor. The internal table is built by performing a linear interpolation on the external table and is used to read out the relevant values at all simulation timesteps.

4.2.3 Updating the Acceleration

At this point we have all we need to compute the B term as a function of time. At every timestep, after the computation of the potential, the gravitational acceleration is calculated in the `gravtree.c` file. We have introduced a modified version of this file, which also computes the additional scattering term. This is calculated by means of the constant and the time dependent terms, with the latter being computed at each timestep by performing a linear interpolation on the internal table. Then the extra term, dubbed `baryon_scattering_friction_factor`, is added exclusively to the baryonic particles, which in the `GADGET` code belong to the type 0, while the type 1 refers to CDM particles (it is possible to handle up to six different type of particles).

4.2.4 A Note on Efficiency

After the implementation of DE-baryon scattering, we performed several test runs with different particle numbers. These runs were of fundamental importance to verify that we have not introduced some bugs in the code as well as to ensure that our modified version is essentially as fast as the standard version.

4.3 The Simulations

In this section we describe the main characteristics of the simulations we performed using our modified version of the `GADGET-3` code.

4.3.1 Initial Conditions and Cosmological Setup

For an easier comparison between the different simulations, we use the same initial conditions for all of them. It is possible to do so without affecting the background cosmological parameters since, as we have seen, the scattering with DE is a particular kind of coupling which does not impact the background evolution. However, it has to be noted that this choice will result in different values of σ_8 at $z = 0$ for the different models. To generate the initial condition file we used the `N-GenIC` code [75], which, basing on the Zel'Dovich approximation [76], displaces the particles from a homogeneous Cartesian lattice so that their density distribution will

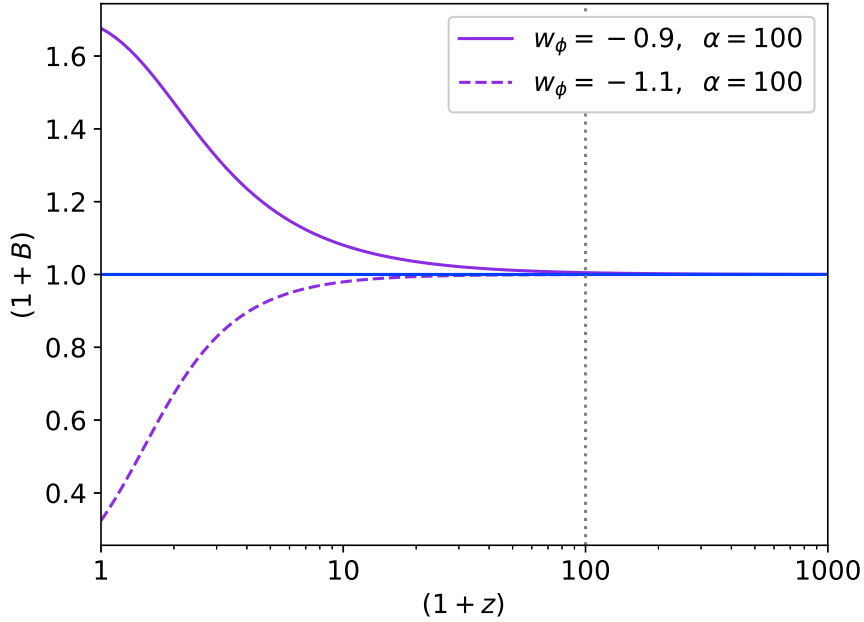


Figure 4.4: Evolution with redshift of the total friction term $(1 + B)$ in the two most extreme cases under study, with $\alpha = 100$. The solid line refers to the model with $w_\phi = -0.9$, while the dashed line refers to to one with $w_\phi = -1.1$. One can see that the effect of DE-baryon scattering rapidly becomes negligible with increasing redshift. In particular, at $z_i = 99$ (dotted vertical line) our assumption of $B \approx 0$ is well supported.

have a random phase and an amplitude following a tabulated power spectrum computed through the public Boltzmann code CAMB [67] and consistent with our cosmological parameters. We chose $z_i = 99$ as starting redshift. The Cosmological parameters chosen are visible in table 4.1, they are consistent with the latest results coming from the Planck satellite [14]. This way of generating the initial conditions excludes any possibility of scattering between DE and baryons before z_i . This assumption is however definitely reasonable in our case: the extra term is in fact proportional to Ω_{DE} , that drops quickly with redshift and soon becomes negligible. To remove all doubt, we show in fig. 4.4 the evolution of the total friction term $(1 + B)$ with redshift in the two most extreme cases: $w_\phi = -0.9$ and $w_\phi = -1.1$, with $\alpha = 100$.

4.3.2 Main Features

Every simulation of our suite has the following features:

- 512^3 CDM particles of mass $7.57 \times 10^9 M_\odot/h$.
- 512^3 collisionless baryonic particles of mass $1.42 \times 10^9 M_\odot/h$.
- Box size equal to 250 Mpc/h.

- Snapshots are taken from $z = 2$ to $z = 0$ every $\Delta z = 0.5$.
- Gravitational softening equal to $\epsilon_g = 12$ kpc/h (approximately 1/40th of the mean inter-particle separation).

All the models under investigations are characterised by a constant value for w_ϕ , moreover in the simulations where the scattering is present, we have set the baryon characteristic mass $M_b = 0.5 \text{ GeV}/c^2$ (this could be thought as an approximate average between the electron and the proton mass). We summarize the nine models under investigation in table 4.2.

4.3.3 Computational Resources

We run our suite of numerical simulations as well as the preliminary test runs on the **Matrix** cluster and performed the analysis of such simulations by means of the **BladeRunner** cluster, both are part of the OPH cluster of the Physics and Astronomy Department of the University of Bologna. In particular, the **Matrix** cluster has the following characteristics:

- 4 Dell PowerEdge C6420 servers hosting 8 multi-core Intel Xeon Gold 5120 processors with 14 physical multi-threaded cores.
- Infiniband Mellanox 100 Gb/s low-latency connection switch.
- 3.6 TB of RAM for an average of 8 GB/core.
- 20 disk nodes with 12 TB/disk.

For our final simulations we used 4 computing nodes, each one with 28 cores, for a total of 112 cores. For each node we allocated 250 GB of RAM.

Parameter	Value
H_0	67.3 km s ⁻¹ Mpc ⁻¹
$\Omega_{\text{DE},0}$	0.722
$\Omega_{m,0}$	0.278
$\Omega_{b,0}$	0.044
$\sigma_8 (z = 0, \Lambda\text{CDM})$	0.832

Table 4.1: Set of the cosmological parameters used in the simulations. These values are consistent with the latest results coming from the Planck satellite [14].

Run	w_ϕ	α
ΛCDM	-1	-
Q0	-0.9	0
Q1	-0.9	1
Q10	-0.9	10
Q100	-0.9	100
P0	-1.1	0
P1	-1.1	1
P10	-1.1	10
P100	-1.1	100

Table 4.2: Suite of the simulations performed with our modified version of the GADGET-3 code. Every simulation is characterized by the DE equation of state w_ϕ and the DE-baryon scattering σ_b in terms of the Thomson ratio $\alpha = \sigma_b/\sigma_T$.

Chapter 5

Analysis of the Simulations

In this chapter we will examine the suite of simulations by means of the cosmological observables introduced in chapter 2. Our focus will be on the impact of DE-baryon scattering on such observables, and on the comparison between the simulations with and without such scattering. One important question we want to address is "How large should the DE-baryon scattering interaction cross section be in order to produce significant effects on the cosmological observables?".

5.1 Large Scale Density Distribution

We start with a visual inspection of the density slices of our simulations. These were computed by means of the `Pylians3` library [77] through a Cloud-in-Cell¹ (CIC) scheme. In figure 5.1 we show the density slices at $z = 0$ of the baryonic matter and CDM distribution for three different cases: the reference Λ CDM simulation and the two simulations with the most extreme scattering interaction ($\alpha = 100$), namely Q100 and P100. Each density slice we show is $150 \times 150 \times 15$ Mpc/ h . We note that the overall shape of the cosmic web is the same for every simulation, this reflects the use of the same initial conditions. Comparing the CDM density distributions we see that no significant difference can be noticed, at least by naked eye. On the other hand if we compare the density distribution of the baryonic matter we observe that the simulation with $w_\phi = -0.9$ and $\alpha = 100$ features an overall less intense clustering of the highest density peaks with respect to the Λ CDM case; conversely we notice the opposite trend for the simulation with $w_\phi = -1.1$ and $\alpha = 100$, which features a stronger clustering on the highest density peaks. The effect can be seen more clearly in the zoomed region of each plot, centered on the highest density peak of the slice. This behaviour reflects our expectations on the linear effects of DE-baryon scattering: suppression or enhancement of the formation of structures whether one has $w_\phi > -1$ or $w_\phi < -1$ respectively.

¹The CIC mass assignment scheme works as follows: once a mesh is chosen, the mass of each particle is distributed over cubes which are of the same size of the mesh cubes but centered on the particles; the mass inside a certain mesh cube is then given by the sum of the intersections of this cube with the cubes around the other particles.

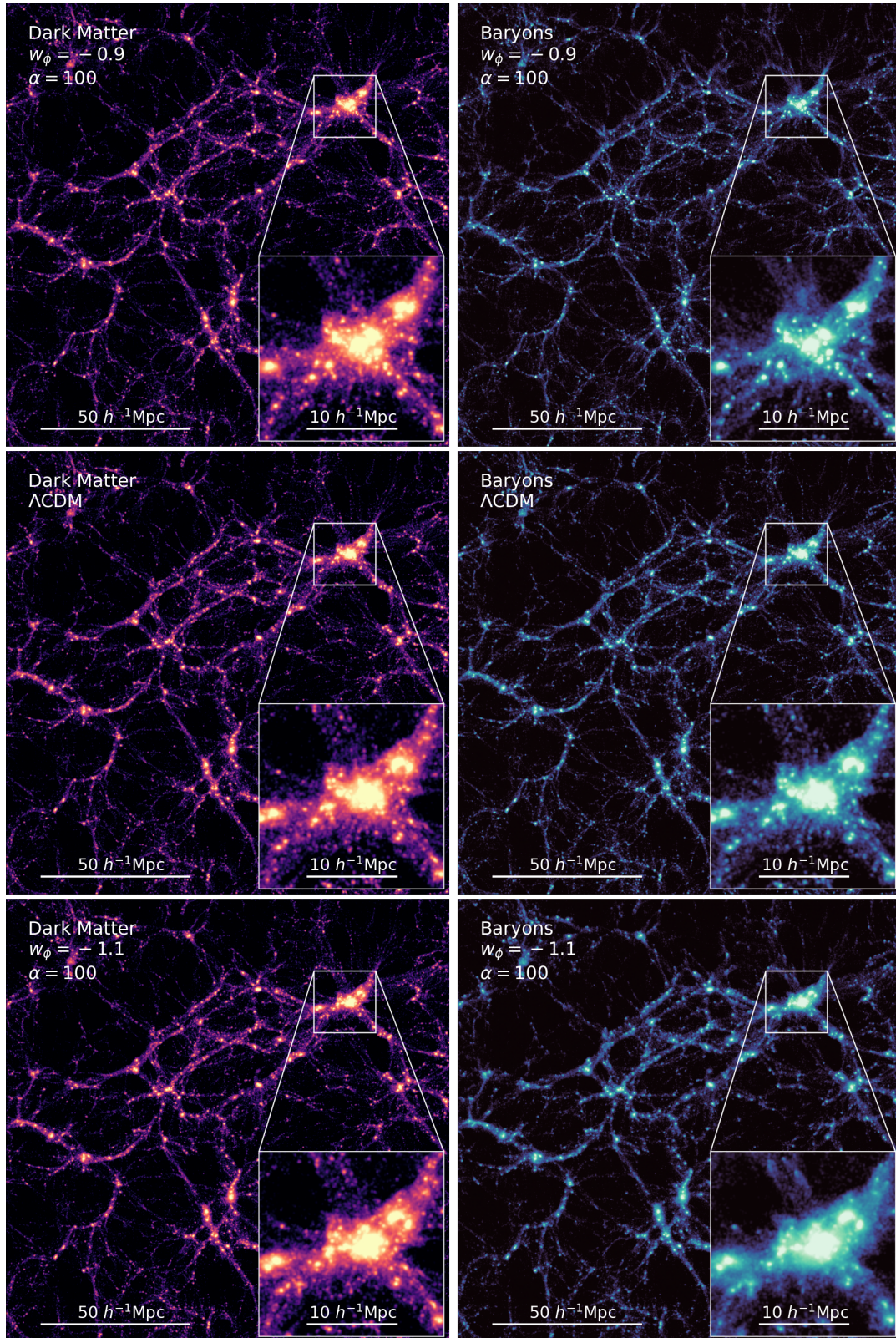


Figure 5.1: Density slices at $z = 0$ of DM (left) and baryons (right) for Λ CDM (middle) and the two $\alpha = 100$ models: $w_\phi = -0.9$ (top) and $w_\phi = -1.1$ (bottom).

5.2 Power Spectrum

We computed the power spectrum for baryons and CDM alone, as well as for total matter. We considered three different redshifts: $z = 0, 0.5, 1$. The spectra were computed by assigning the mass to a cubic Cartesian grid by means of the CIC scheme, to do so we again employed `Pylians3`. The grid chosen has half the spacing of the mesh used for the large-scale N-body integration, which means 1024^3 modes. This corresponds to a computation of the power spectrum up to the Nyquist frequency associated with the grid, given by $k_{\text{Ny}} = \pi N/L \approx 12.9 h/\text{Mpc}$. Once the spectra were computed, we considered the ratio between every case and the ΛCDM reference case. These results are visible, for each of the redshifts under consideration, in the left column of figures 5.2, 5.3 and 5.4 for baryons, CDM and total matter power spectra respectively. Moreover, for a more complete analysis, we wanted to isolate the effects of the scattering with respect to the ones caused by the background expansion for the $w_\phi \neq -1$ models. To do so, we also considered the ratio between every model with $w_\phi \neq -1$ and the corresponding case with the same w_ϕ but no scattering ($\alpha = 0$). The plots are visible in the right column of figures 5.2, 5.3 and 5.4. In first place, we notice that the effects of DE-baryon scattering become more significant as redshift approaches the present value $z = 0$, this is not unexpected: the effects at lower redshifts are indeed integrated over longer times; moreover, looking at figure 4.4, we can notice that the B term, describing the scattering intensity, significantly increases its absolute value in time. This is essentially due to the fact that $B \propto \Omega_{\text{DE}}$ and, in the models under investigation, dark energy became a non negligible component of the Universe in relatively recent times. In second place we observe that the effects are opposite when considering $w_\phi = -0.9$ and $w_\phi = -1.1$, this can be simply explained by the fact that the B term changes its sign according to whether w_ϕ is greater or lesser than -1 . We can now focus our analysis of the power spectra of the different components.

Baryonic matter

Let us start with the plots concerning the baryonic matter power spectrum. We see that the linear effects consist in the enhancement and suppression of the power respectively for $w_\phi = -1.1$ and $w_\phi = -0.9$, this is in concordance with the physical interpretation introduced in [61] and mentioned previously: in the linear regime, the peculiar velocity of the particles is aligned with the gradient of the potential, and so the DE-baryon scattering acts like a friction/drag term suppressing/enhancing the structure formation in the $w_\phi = -0.9$ and $w_\phi = -1.1$ cases respectively. We notice that this effect is non negligible only for the most extreme cases ($\alpha = 100$) in which we have a deviation from the non-scattering model of $\approx 15\%$ at $z = 0$, which slightly decreases as z increases in the $w_\phi = -0.9$ case, and more significantly in the $w_\phi = -1.1$ case. We see that the scale of the transition from the linear to the nonlinear regime takes place between $k \sim 0.6 h/\text{Mpc}$ and $k \sim 2 h/\text{Mpc}$. For what concerns the nonlinear effects, we observe the opposite

trend: an enhancement of the power when $w_\phi = -0.9$ and a suppression when $w_\phi = -1.1$. To interpret this behaviour we again recall [61]: in the nonlinear regime the velocity field is no more aligned with the gradient of the potential and the collapsing structures start to gain angular momentum; in this context, the presence of a friction/drag term supports/opposes the loss of angular momentum by the baryonic particles, and this translates in faster/slower collapse of nonlinear structures for $w_\phi = -0.9$ and $w_\phi = -1.1$ respectively. We notice that the nonlinear effects become significant also for the cases in which $\alpha = 10$, moreover the dependence from redshift is stronger than in the linear regime. At scales $k \sim 10 h/\text{Mpc}$ we find a deviation from the non-scattering model of $\approx 140\%$ at $z = 0$, $\approx 70\%$ at $z = 0.5$ and $\approx 35\%$ at $z = 1$ in the most extreme cases and a significantly lower deviation of $\approx 10\%$ at $z = 0$ in the cases with $\alpha = 10$.

CDM

Let us now consider the CDM power spectrum: we find that every effect is significantly damped with respect to the ones on the baryonic matter power spectrum, this is due to the fact that in our models CDM is not scattering with DE, and so the effects on the power spectrum are only indirectly transmitted via gravitational interaction with baryonic matter, which however is subdominant. At the linear scales the deviation from the non scattering case never exceeds $\approx 3\%$. On the other hand, in the nonlinear regime, we still found some significant deviation when $\alpha = 100$: considering scales $k \sim 10 h/\text{Mpc}$ it is $\approx 20\%$ at $z = 0$, $\approx 10\%$ at $z = 0.5$ and $\approx 6\%$ at $z = 1$.

Total matter

Last but not least, let us look at the results of DE-baryon scattering on the total matter power spectrum: as expected we see that the effects are milder than the baryons-only case. At the linear level, when $\alpha = 100$, we notice an enhancement/suppression with respect to the non-scattering model which goes from $\approx 10\%$ at $z = 0$ to $\approx 4\%$ at $z = 1$. Again, the nonlinear effects are more significant: at scales $k \sim 10 h/\text{Mpc}$ and for $\alpha = 100$, we find a deviation from the non-scattering model of $\approx 30\%$ at $z = 0$, $\approx 15\%$ at $z = 0.5$ and $\approx 10\%$ at $z = 1$. In the $\alpha = 10$ case, we only notice a deviation, at $z = 0$ and $k \sim 10 h/\text{Mpc}$, of $\approx 3\%$.

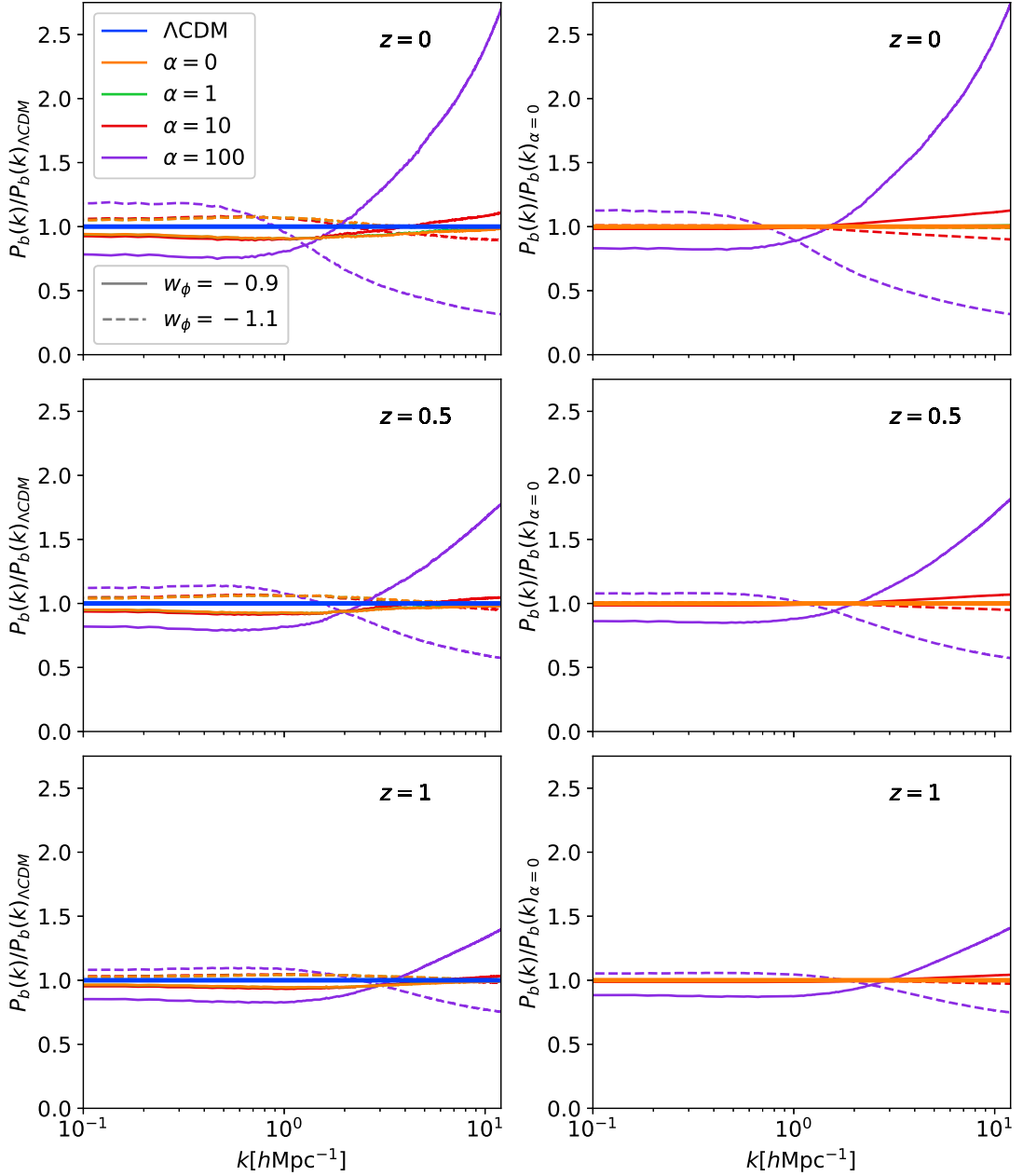


Figure 5.2: Ratio of the baryonic matter power spectrum to the ΛCDM reference model (right) and to the $\alpha = 0$ case (left). We consider both models with $w_\phi = -0.9$ (solid lines) and with $w_\phi = -1.1$ (dashed lines) and three redshifts $z = 0$ (up), $z = 0.5$ (middle), $z = 1$ (down). The intensity of DE-baryon scattering is described by the Thomson ratio $\alpha = \sigma_b/\sigma_T$. We see opposite effects depending on the value of w_ϕ , moreover if the power is enhanced at smaller scales, it is then suppressed at larger ones, and vice-versa.

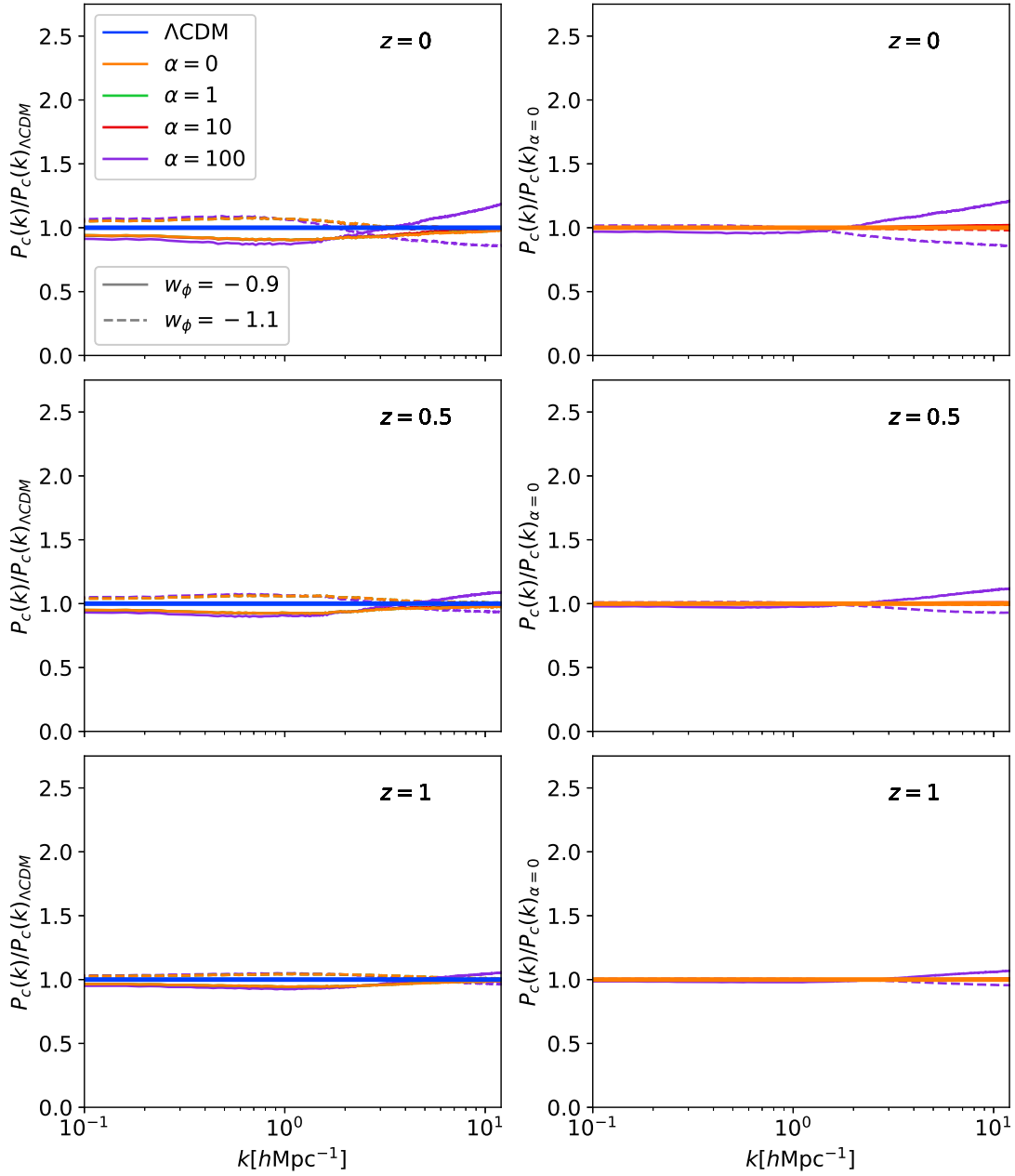


Figure 5.3: As figure 5.2 but for the cold dark matter. As expected the effects are significantly weaker with respect to the case of baryonic matter.

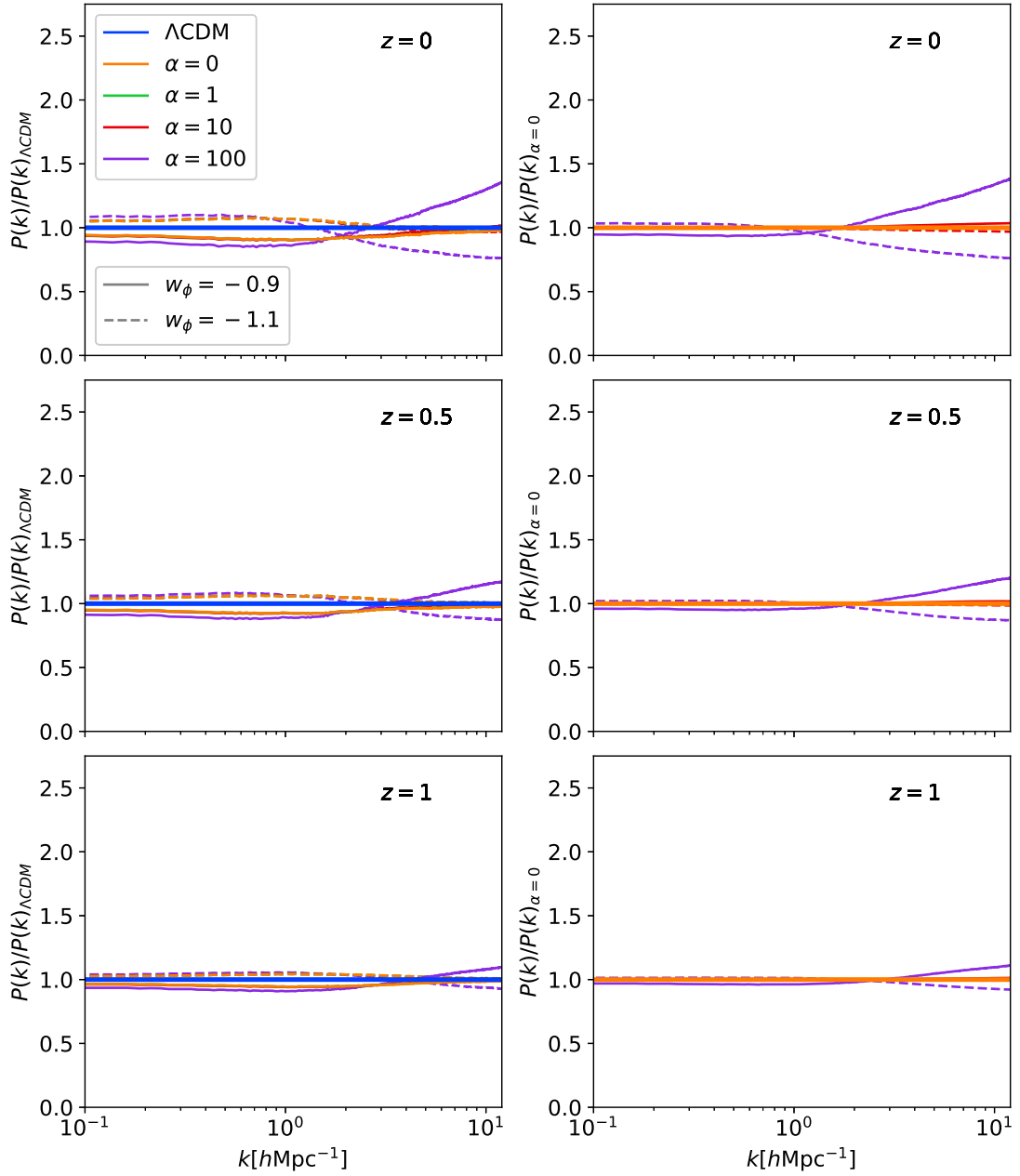


Figure 5.4: As figure 5.2 but for the total matter. In this case the effects are milder than in the case with only baryonic matter.

5.3 Halo Mass Function

We computed the halo mass function for every snapshot of each simulation as the number of halos with mass $M_{200,\text{crit}}$ lying within a certain number of logarithmic mass bins. To do so we started from the halo catalogues generated by the `SUBFIND` routine, included in the code. For a first consistency check, we compared the cumulative mass functions of our models with the one predicted by the Jenkins et al. formula [18] (see eq. 2.17) in the same Λ CDM cosmology as our reference model. We show the results of such comparison in figure 5.5. We observe a slight scale dependence when comparing each model to the Jenkins function, however we find good concordance between our reference Λ CDM model and the theoretical prediction: the deviation never goes beyond 3% in the range between 2×10^{11} and 10^{14} ; we also note that, for masses below $10^{14} M_{\odot}/h$, every model is below deviations of $\approx 10\%$. We now focus on the effects of DE-baryon scattering on the halo mass function. In figure 5.6 we show, in the same fashion of the power spectrum analysis, the ratio between every model and the reference Λ CDM model in the left column and the ratio between every case with $w_{\phi} \neq -1$ and its respective $\alpha = 0$ case in the right column. We again consider the three redshifts $z = 0, 0.5, 1$. To make these plots we considered 10 logarithmically equispaced mass bins in the range $10^{12} - 10^{14} M_{\odot}/h$. We notice that also in this case the effects of the scattering become more relevant as redshift approaches $z = 0$. For the most extreme cases, i.e. the two with $\alpha = 100$ we find a significant deviation both from the Λ CDM and from the respective non-scattering case. In particular one can see that in the $w_{\phi} = -0.9$ case there is an enhancement of the abundance of halos at all masses which is of $\approx 5\%$ at $z = 0.5$ and grows to $\approx 10 - 15\%$ at $z = 0$, where it shows a trend that slightly increases with the mass. On the other hand, for $w_{\phi} = -1.1$, we have a suppression of the abundance of $\approx 5\%$ at $z = 0.5$ and $\approx 13\%$ at $z = 0$. For what concerns the other scattering cases with lower cross section, we do not notice any significant effect, with the exception of a mild deviation at $z = 0$ in the $\alpha = 10$ cases, with an amplitude of $1 - 2\%$. The enhancement/suppression we observe in the cases $w_{\phi} = -0.9$ and $w_{\phi} = -1.1$ respectively is connected to the nonlinear effects of the DE-baryon scattering described in the previous section: the nonlinear collapse of structures is indeed enhanced/suppressed in the presence of a friction/drag term acting on baryons and supporting/opposing their loss of angular momentum.

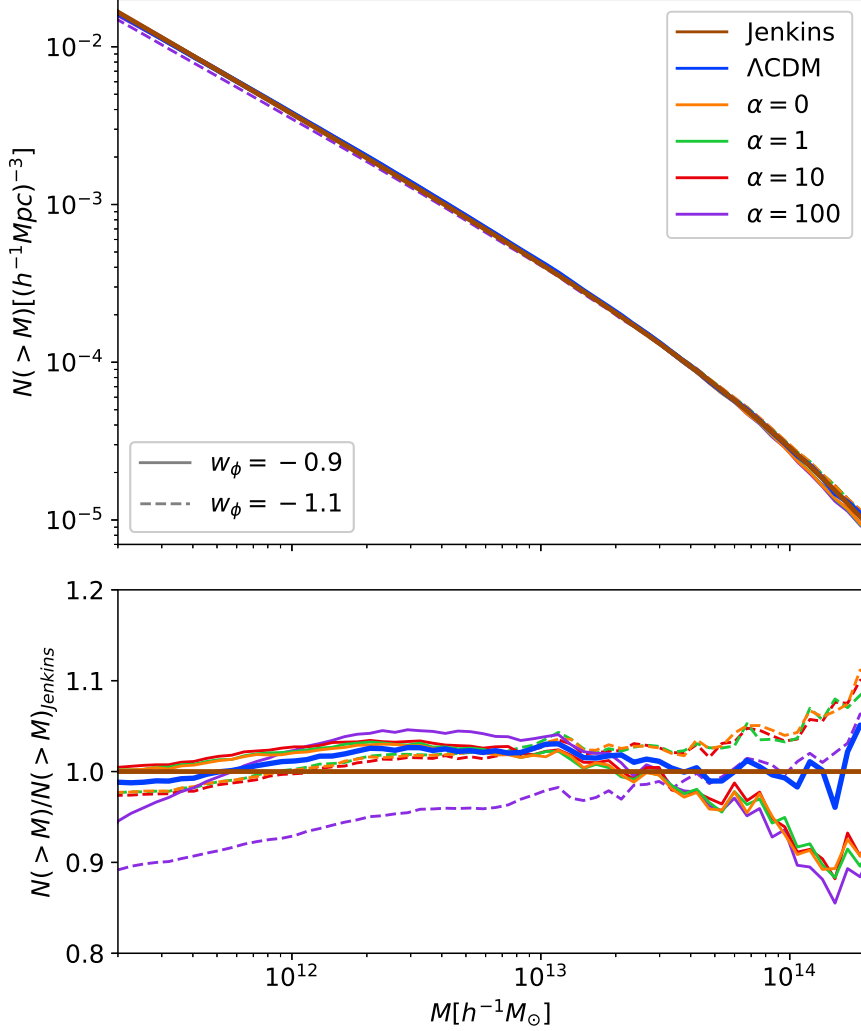


Figure 5.5: Upper panel: cumulative halo mass function at $z = 0$ as predicted by the Jenkins et al. [18] formula (brown) and as computed for the reference ΛCDM model (blue line) as well as for the models with $w_{\phi} = -0.9$ (solid lines) and with $w_{\phi} = -1.1$ (dashed lines). Lower panel: cumulative halo mass function ratio between our models and the Jenkins prediction. The halos were detected with the SUBFIND routine, included in our code. Our reference model is in good agreement with the predicted mass function: even if there is a slight scale dependence, the deviations remain under $\approx 3\%$

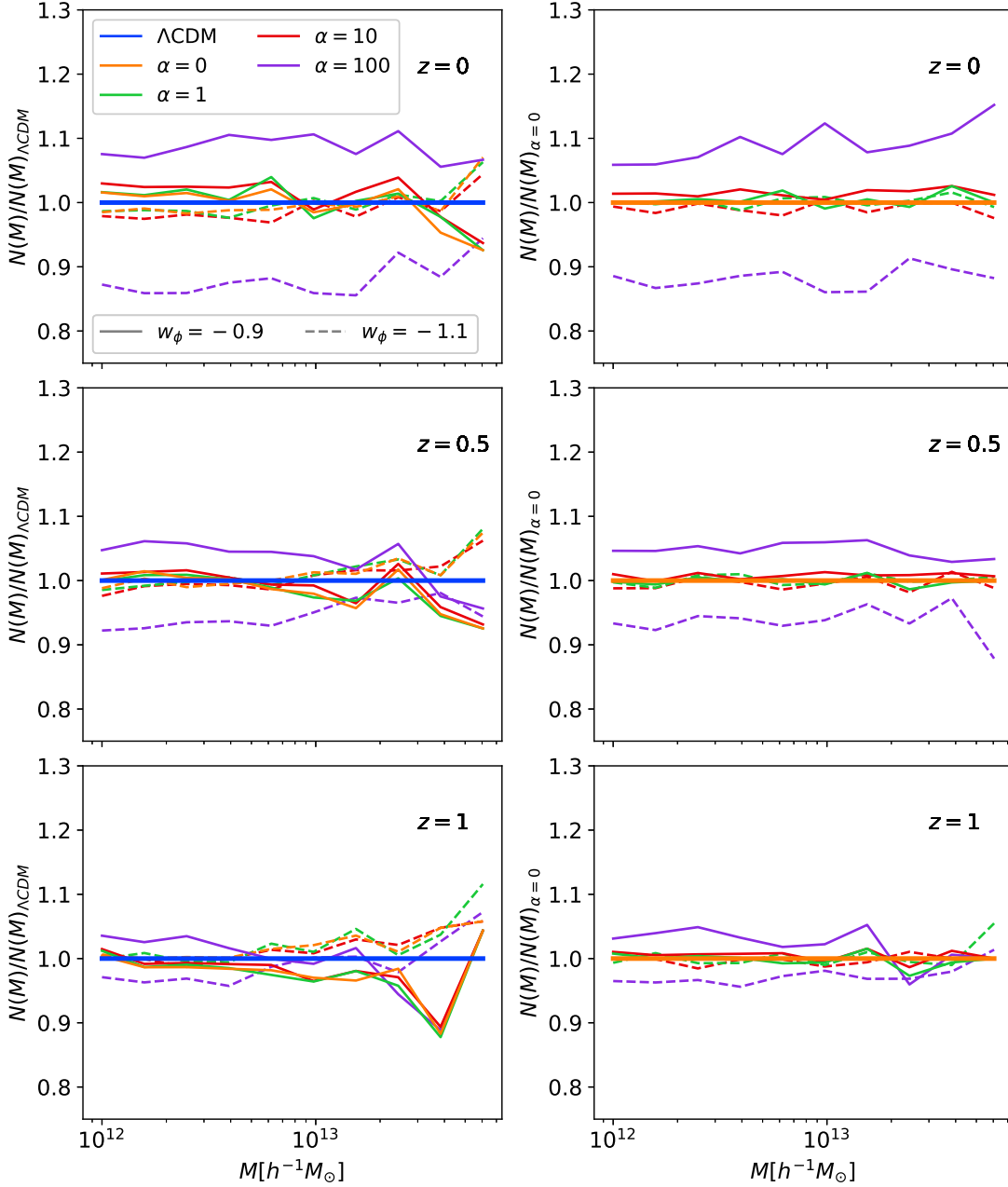


Figure 5.6: Ratio of the halo mass function to the ΛCDM reference model (left) and to the $\alpha = 0$ case (right). We consider both models with $w_{\phi} = -0.9$ (solid lines) and with $w_{\phi} = -1.1$ (dashed lines) and three redshifts $z = 0$ (up), $z = 0.5$ (middle), $z = 1$ (down). The different intensity of DE-baryon scattering is described by the Thomson ratio $\alpha = \sigma_b/\sigma_T$.

5.4 Halo Profiles

To produce the radial density profiles of the halos we used a specific C code which we are going to briefly describe. First, the user selects which snapshots of the simulation has to be considered, as well as the number of halos to consider and the mass interval in which the halos must lie. Once this parameters are given, the code starts looking through the catalogues produced by the SUBFIND routine, which contain M_{200} , R_{200} and the positions of the halos. If a suitable halo is found in the catalogue, the code opens the snapshot file(s) and looks for the particles that make up the halo. The radial profile is built at this point in the following way: the position of the particle with minimum potential is taken as the center of the halo, and a certain number, also set by the user, of spherical shells with logarithmically equispaced thickness is considered. The code computes the radial profile by counting how many particles lie in each shell and dividing by the shell volume. To make the comparison between different halos easier, the profiles are given as a function of R/R_{200} . This process is repeated for every particle type considered (DM and baryons in our case) and for the number of desired halos. By means of this code we computed, for every simulation, DM and baryonic matter profiles for 100 halos in each one of the following mass bins:

- Mass bin 1: $5 \times 10^{12} M_{\odot} < M_{200} < 10^{13} M_{\odot}$.
- Mass bin 2: $10^{13} M_{\odot} < M_{200} < 5 \times 10^{13} M_{\odot}$.
- Mass bin 3: $5 \times 10^{13} M_{\odot} < M_{200} < 10^{14} M_{\odot}$.
- Mass bin 4: $10^{14} M_{\odot} < M_{200} < 5 \times 10^{14} M_{\odot}$.

At this point we are ready to analyze the results. We chose two parallel ways that are described in the following.

Profiles of the same halo in different simulations

The first method we employed to analyze the effects of DE-baryon scattering on halo density profiles consists in the direct comparison of the profiles of objects in different simulation that can be considered as the same structure. To do so we wrote a python script which compares all the halos found in a certain mass range in every simulation. We consider objects in the various simulations to be indeed the same structure if all of the following conditions are satisfied:

- M_{200} and R_{200} deviations must not be greater than 10%.
- The centers of the structures must not be displaced of more than the 80% of the average R_{200} .

With this criterion we are able to detect 80 object in the range $5 \times 10^{12} M_{\odot}/h < M_{200} < 5 \times 10^{14} M_{\odot}/h$ which can be considered to be the same halo in different simulations. In figure 5.7 we show four radial density profiles at $z = 0$ of both DM and baryons from our sample. Each halo lies in one the four different mass bins considered. We note that, as the mass increases, the profile tends to have less noise in it, this is because more massive halos are composed by a larger number of particles. In first place, we notice that, as expected, the profiles of the reference Λ CDM model are consistent with the NFW profile. Second, despite the noise, we can observe that the effects of DE-baryon scattering have also in this case an opposite trend: we see an increase/decrease of the inner density in the baryonic matter profile respectively for the cases $w_{\phi} = -0.9$ and $w_{\phi} = -1.1$; this effect is significant only for the most extreme scattering cases, i.e. the two with $\alpha = 100$.

Stacked profiles

To reduce the noise and focus better on the effects of DE-baryon scattering, we considered a second approach: we produced four stacked profiles at $z = 0$, one for each mass bin. This is done by averaging the value of the density at each radius between 100 randomly picked halos from our catalogue. In this case we must consider the profile over R/R_{200} instead of the physical radius, in order to fairly compare halos with different R_{200} . The stacked profiles are visible in figure 5.8. By looking at the baryonic matter profiles we can confirm a strong increase/decrease of the inner density at every mass when $\alpha = 100$, moreover we note a tiny deviation for $\alpha = 10$. With the stacked profiles we are able to detect another interesting feature: at large radii the effect of the scattering has an opposite trend than the one at inner radii, at every mass range we have indeed a decrease/increase of the outer density when $\alpha = 100$ respectively for $w_{\phi} = -0.9$ and $w_{\phi} = -1.1$. The transition between the two effects takes place at $\approx 0.5R_{200}$ in every mass range under consideration. These two opposite effects could be possibly explained by means of the physical interpretation given in [61] for the dark scattering and mentioned in section 5.2. By means of the stacked profiles it is also possible to notice that the effects of the scattering are also present in the DM profiles, but with significantly lower intensity.

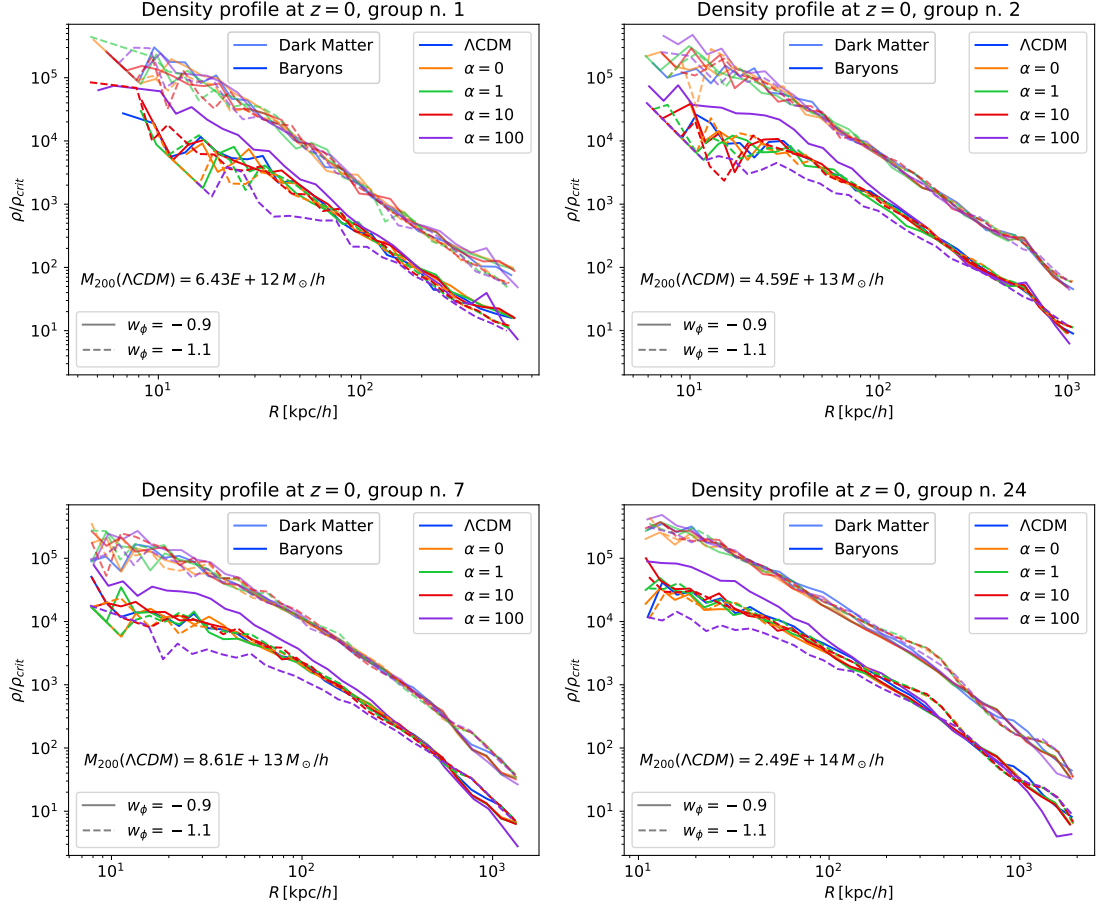


Figure 5.7: Radial density profiles at $z = 0$. We show the reference Λ CDM model (blue line) and the models with $w_\phi = -0.9$ (solid lines) and $w_\phi = -1.1$ (dashed lines). The different intensity of DE-baryon scattering is described by the Thomson ratio $\alpha = \sigma_b/\sigma_T$. We show both DM profiles (shaded) and baryonic matter profiles (bright).

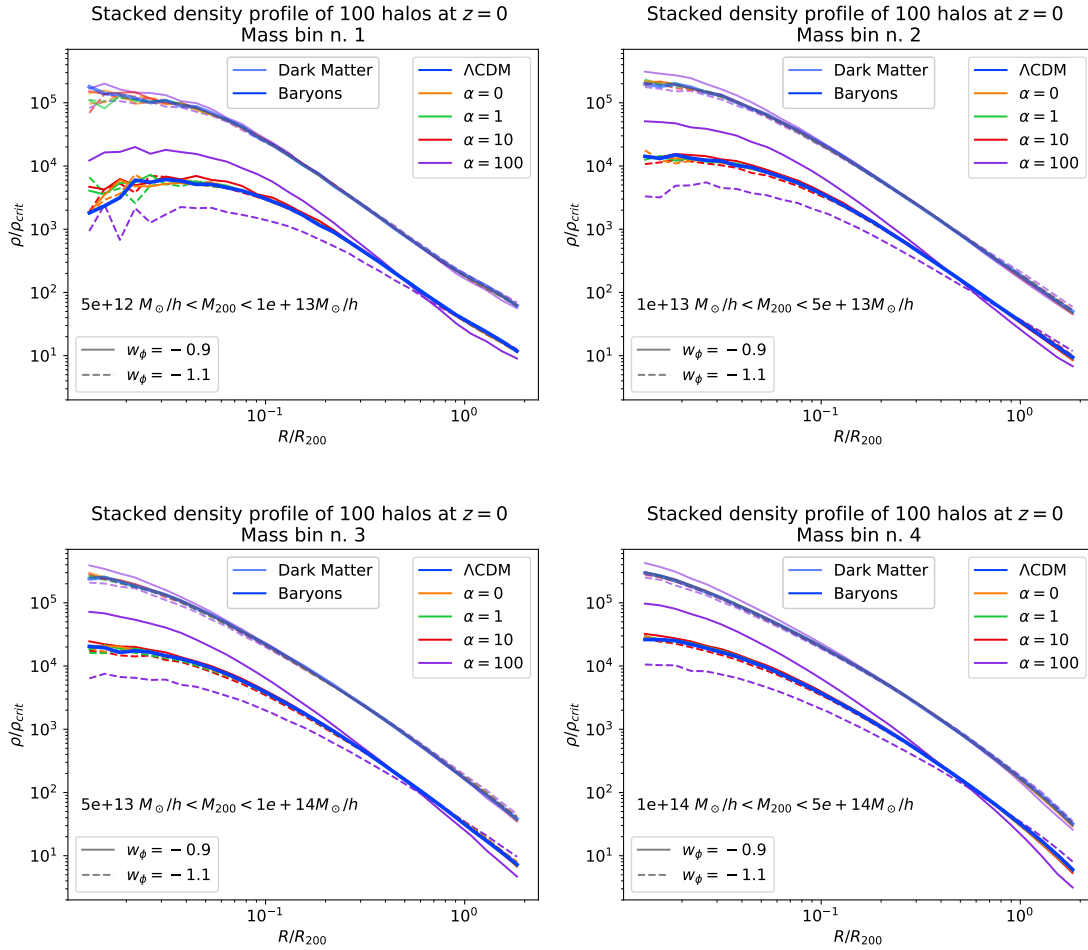


Figure 5.8: Stacked radial density profiles in different mass ranges at $z = 0$ of the reference ΛCDM model (blue line) and for the models with $w_{\phi} = -0.9$ (solid lines) and $w_{\phi} = -1.1$ (dashed lines). The different intensity of DE-baryon scattering is described by the Thomson ratio $\alpha = \sigma_b/\sigma_T$. We show both DM profiles (shaded) and baryonic matter profiles (bright). Each stacked profile is computed by averaging 100 halo profiles in each mass range.

5.5 Halo Baryon Fraction

Starting from the halo profiles, we computed the radial baryon fraction. In practice we first computed the cumulative mass profiles $M(R)$ of the two components by integrating the density profile. For a generic component x we have:

$$M_x(R) = 4\pi \int_0^R \rho_x(R') R'^2 dR'. \quad (5.1)$$

In our case the integral reduces to a discrete sum over a certain number of spherical shells. Once the cumulative mass of DM and baryons were computed, we took the ratio $M_b(R)/M_c(R)$. In figure 5.9 it is possible to see the baryon fraction stacked profiles obtained also in this case by averaging 100 halos in each one of the four mass bins. We choose a minimum radius for our plots as follows: we consider the smallest halo of each mass bin and we start plotting from the radial bin at which the physical radius exceeds 36 kpc, i.e. three times the softening length ε_g . In the Λ CDM reference case, as well as in the cases with $\alpha = 0$, we see that the radial profile of the baryon fraction has a similar trend in the different mass ranges: in the innermost region we have $M_b/M_c \approx 0.1$ for the less massive halos and ≈ 0.14 for the most massive ones; we then observe a growth of the fraction which tends to settle around $\approx 0.19 \approx \Omega_{b,0}/(\Omega_{m,0} - \Omega_{b,0})$, i.e the expected cosmic baryon fraction at $z = 0$ according to the cosmological parameters chosen in our simulations. We observe that the systematically lower baryon fraction in the inner regions could be connected to dynamical friction, acting on the CDM particles, which are more massive than the baryonic ones, and/or to numerical heating. Let us now consider the effects of DE-baryon scattering on the baryon fraction. For the $\alpha = 1$ case we do not notice any significant deviation from the reference case. When $\alpha = 10$ we observe a systematic $\approx 5\%$ enhancement/suppression respectively for the $w_\phi = -0.9$ and $w_\phi = -1.1$ cases. As R approaches R_{200} we observe that in both cases the effect is damped and the value converges to the reference case. The situation is different when we consider the most extreme scattering cases, i.e. $\alpha = 100$, in which it is possible to see that the baryon fraction profiles are significantly distorted. In the case $w_\phi = -0.9$ and $\alpha = 100$ we notice a strong enhancement at small radii which leads to deviations of $\approx 100\%$; we then have a relatively steep decrease that lets the baryon fraction reach $M_b/M_c \approx 0.19$ at $R \approx 1.5R_{200}$ and even lower values at larger radii. On the other hand, when $w_\phi = -1.1$ and $\alpha = 100$, we observe an overall suppression of $\approx 50\%$; in this case the profile features a regular growth of the baryon fraction, which is specular to the $w_\phi = -0.9$ case; we can see that even at $R \approx 2R_{200}$ the baryon fraction is lower than the reference case. These two opposite behaviours in the most extreme cases can be explained considering that the friction/drag term helps/opposes the loss of angular momentum, thus enhancing/suppressing the gravitational collapse of baryonic particles into the DM halos, respectively for $w_\phi = -0.9$ and $w_\phi = -1.1$. It is important to note that the significant modification of the baryon fraction brought by DE-baryon scattering in the most extreme cases is expected

to importantly impact on several astrophysical processes including star formation, galaxy formation, AGN feedback and so on. This scenarios could be properly studied by means of simulations which also include hydrodynamics, we leave this for future work.

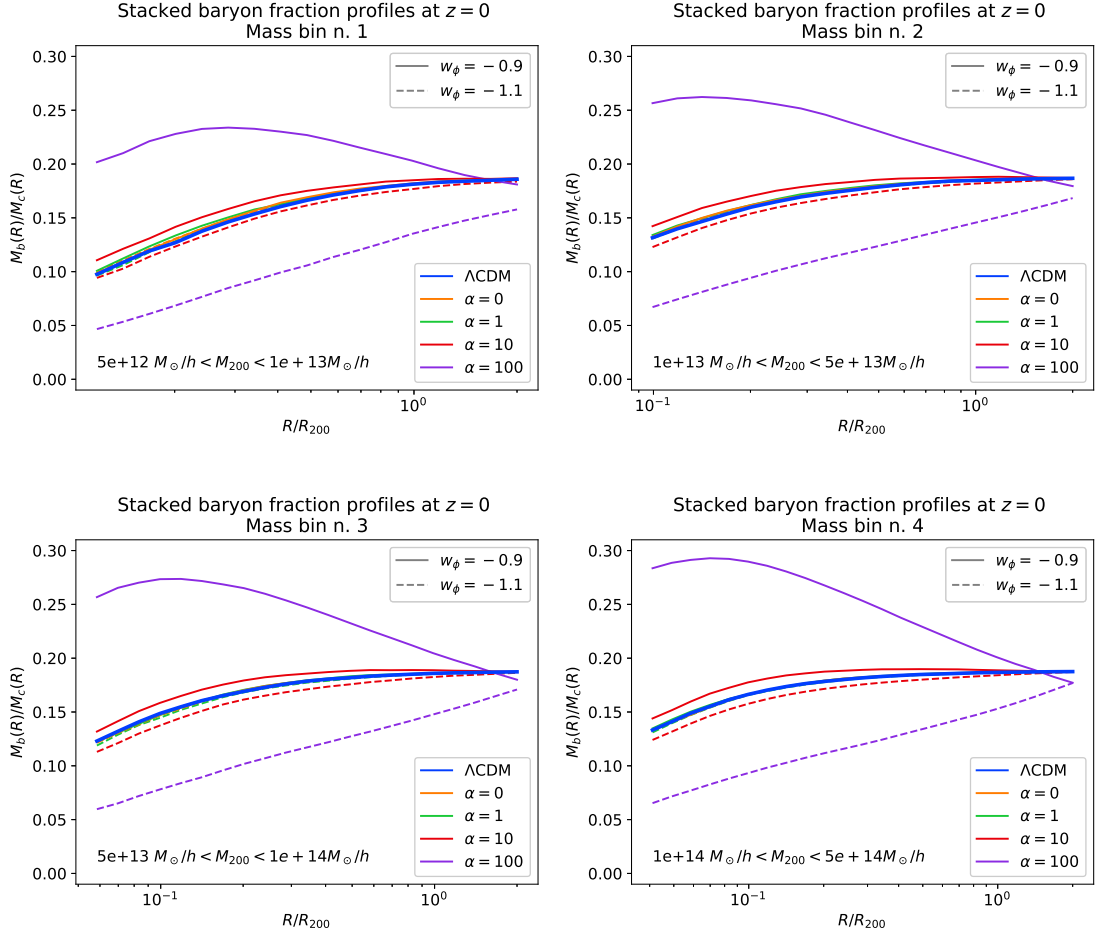


Figure 5.9: Stacked radial profiles of baryon fraction in different mass ranges at $z = 0$ of the reference Λ CDM model (blue line) and for the models with $w_\phi = -0.9$ (solid lines) and $w_\phi = -1.1$ (dashed lines). The different intensity of DE-baryon scattering is described by the Thomson ratio $\alpha = \sigma_b/\sigma_T$. Each stacked profile is computed by averaging 100 halo profiles in a certain mass range.

Chapter 6

Conclusions and Future Prospects

In this chapter we are going to summarize our work and results, before doing so we recall the cosmological background in which we operated. A final section is left for an overview of the possible future developments of this work.

6.1 Cosmological Background

The first chapter of this thesis is dedicated to the introduction of some fundamentals of cosmology. In section 1.1.1 we started by considering that modern cosmology relies on Einstein's theory of General Relativity, together with the assumption of the Cosmological Principle; this made us able to derive the Friedmann equations, which describe the background evolution of the Universe. In section 1.1.2 we used the Friedmann equations to describe the background evolution of a multi-component Universe. In section 1.1.3 we introduced some basic concepts like the redshift and different possible definitions of cosmological distances: the proper distance, the comoving distance, the luminosity distance and the angular diameter distance. In section 1.1.4 we exposed the main observational evidence of dark energy, a mysterious component which drives the late-time accelerated cosmic expansion. These include supernova observations, baryonic acoustic oscillations and CMB. In section 1.1.5 we introduced the Standard model of cosmology, namely Λ CDM. This is mainly based on the presence of cold dark matter, of the inflationary epoch in the early Universe and on the identification of DE as the Cosmological Constant Λ , which has an equation of state $w_\Lambda = -1$ and can be readily interpreted as the vacuum energy. In section 1.2 we exposed two long standing problems of the Λ CDM model, namely the *fine tuning* and the *coincidence* problems, as well as two tensions that appeared in more recent times, these concern the measure of the two cosmological parameters σ_8 and H_0 . We concluded the first introductory chapter with section 1.3, in which some basics of cosmological perturbation theory are provided.

In the second chapter we described three cosmological observables which are of primary interest in this work, since these were used in our analysis to test the

effects of scattering between DE and baryons. In particular, in section 2.1 we introduced the concepts of power spectrum and correlation function, and gave an overview of the evolution of density perturbations on different scale lengths during the history of our Universe. In section 2.2 we defined the mass function and mentioned the analytical formulae that can be obtained by means of two important theoretical models, the spherical collapse and the ellipsoidal collapse, as well as the simulation-calibrated formula provided by Jenkins et al. that we later used for a consistency check of our simulations. In section 2.3 we described some remarkable density profiles typically used to model the matter distribution inside halos, the most important being the universal NFW profile; we also introduced two widely used halo finding algorithms, namely FoF and SUBFIND, which were employed in the simulations of the present work.

As we saw, despite the Λ CDM model is in good agreement with most of the available observational datasets, it is not free from tensions and open questions. In this context several models concerning alternative cosmologies have been proposed and studied in the literature. The third chapter has been indeed devoted to a further investigation on dark energy beyond the cosmological constant. In section 3.1 we introduced the so-called quintessence and phantom models, based on a form of dynamical dark energy associated with a scalar field ϕ with an equation of state $w_\phi \geq -1$ and $w_\phi < -1$, respectively. In section 3.2 we saw how these models can be further extended to the interacting DE scenario, in which a nonminimal coupling with matter is assumed. We studied how the coupling between the DE scalar field and matter affects the evolution of the Universe both at the background level and at the level of linear perturbation theory (section 3.2.1 and 3.2.2); we observed in section 3.2.3 how one of the most significant effects introduced by the coupled DE scenario is the presence of an intermediate epoch, dubbed ϕ MDE, during which the two coupled fluids (i.e. matter and DE) maintain a constant ratio of energy densities. In section 3.3 we introduced a particular form of coupling between DE and DM, the so-called dark scattering (see [60]). In this case the interaction of the two components is described in terms of a pure momentum exchange, whose intensity is modulated by the scattering cross section; an interesting feature of the scattering with DE is that this interaction leaves the background evolution unaltered, thereby lacking the ϕ MDE epoch that characterises standard coupled DE models. In section 3.3.1 we studied dark scattering at the level of linear perturbation theory, we saw that, under the hypothesis that DE sound speed is equal to the speed of light (so that DE perturbations are damped at sub-horizon scales) this interaction translates mathematically into an additional velocity-dependent term in the Euler equation of the coupled matter particles; this extra friction/drag is dependent on the DE energy density, on the mass of the matter particle, on the scattering cross section and on the equation of state of DE. This last dependence sets the sign of the additional term, thus determining whether it behaves like a friction or a drag for $w_\phi > -1$ and $w_\phi < -1$ respectively. We then saw, in section 3.3.2, that dark scattering models have been implemented

in numerical simulations (see [61, 62]) in order to investigate the effects of such interaction also at nonlinear scales. Indeed, it has been found that the nonlinear effects can be significantly stronger than the linear ones. In section 3.4, we focused our attention on a recent work (see [64]) in which a similar scenario featuring a scattering between DE and baryon has been introduced and studied at the linear level in order to see if it was possible to put some constraints on such interaction by means of cosmological observations. This scenario has been the main target of the research work presented in this thesis. In this class of models the scattering can be described with the introduction of the Thomson ratio $\alpha = \sigma_b/\sigma_T$, i.e. the ratio between the DE-baryon scattering cross-section σ_b and the Thomson cross-section σ_T . The authors of [64] modified the **CAMB** code in order to solve the linear perturbations equations in the presence of DE-baryon scattering. Their analysis regarded the linear effects of such interaction on two important cosmological observables: the matter power spectrum and the CMB temperature power spectrum. Their conclusion was that, even for very large values of the DE-baryon scattering cross section, i.e. $\alpha \gg \mathcal{O}(1)$, no significant deviations were found; at least at the level of the linear theory. Therefore, the only yet unexplored field that leaves an opportunity to put cosmological constraints on such interaction remains the nonlinear regime of structure formation, in which, in analogy with the findings of [61, 62], the effects could be stronger than in the linear regime. The nonlinear regime can be properly studied only through N-body numerical simulations, this constitutes the main motivation of the present work. We concluded this section mentioning that DE-baryon scattering model should also come equipped with a proper screening mechanism, able to make the interaction vanish on solar system scales. However, to keep things easier, we did not include in this work such screening mechanism.

6.2 Our Work and Results

The DE-baryon scattering model and its linear analysis operated in [64] represent the starting points and the main motivation of the present thesis. In this work, for the first time in the literature, structure formation multi-particle simulations implementing DE-baryon scattering have been performed in order to investigate the nonlinear effects of this interaction on cosmological observables.

The fourth chapter was dedicated to the description of the code we used, i.e. **GADGET-3** [70], and of the way it has been modified in order to perform our numerical simulations, whose main features have also been described. In section 4.1.1 we introduced the equations of collisionless dynamics, which are implemented in the code. We underline that in the present work we modeled baryons as a collisionless fluid, i.e. we neglected hydrodynamics. This approximation is motivated by the fact that these are the first simulations ever performed for these models and we then want to focus exclusively on the effects of the scattering, without the complication to disentangle them from other effects acting on baryons. In

sections 4.1.2 and 4.1.3 we described the Tree algorithm and the Particle Mesh method in order to introduce, in section 4.1.4, the TreePM algorithm, which is the one implemented in the `GADGET-3` code to solve the equations of gravity. In section 4.1.5 we gave an overview of the parallelization strategies of the code. In section 4.2 we described our modification of `GADGET-3`: essentially, we acted on the code so that the extra friction/drag term could be computed and added to the gravitational acceleration of the baryonic particles. We have verified with several test runs that our implementation is perfectly working and as fast as the original version of `GADGET-3`. In section 4.3.1 we described how the initial conditions for our simulations have been generated by means of the `N-GenIC` code and the cosmological parameters used, consistent with the latest results of [14]. In section 4.3.2 we exposed the features of our suite of multi-particle numerical simulations: every simulation was characterized by a $250 \text{ Mpc}/h$ comoving box filled with 512^3 particles of collisionless baryons plus 512^3 CDM particles. The suite was comprehensive of: the reference Λ CDM model, four quintessence-like DE models with $w_\phi = -0.9$ and four phantom-like DE models with $w_\phi = -1.1$. The non standard models had increasing values of the Thomson ratio $\alpha = 0, 1, 10, 100$. In section 4.3.3 we exposed the technical specifications of the `Matrix` computing cluster, used to run all the simulations.

In the fifth chapter we performed the analysis of our simulations. We started considering the slices of the large scale density distribution in section 5.1. Then, in section 5.2 we investigated the effects of DE-baryon scattering by means of the nonlinear power spectrum. We computed the spectra for the baryonic matter, the CDM and the total matter at the redshifts $z = 0, 0.5, 1$. We found that the effects on the power spectrum induced by the DE-baryon scattering become larger as the redshift approaches $z = 0$. As expected, the effects on the baryonic matter power spectrum were significantly larger than the ones on the CDM spectrum. In agreement with the findings of [61, 62], in which however a DE-CDM scattering was considered, we found that DE-baryon scattering enhances or reduces the linear power with respect to the non-scattering case depending on whether one considers $w_\phi = -1.1$ or $w_\phi = -0.9$ but also that these effects are reversed at nonlinear scales. We noticed that the transition between the linear and the nonlinear effects occurs roughly at the same scale $k \sim 0.6 - 2 \text{ h}/\text{Mpc}$ for all the models. For what concerns the total matter power spectrum at $z = 0$, considering the deviation in the scattering cases with respect to the non-scattering case, we found that at linear scales there is a uniform suppression/enhancement of $\approx 10\%$ in the $\alpha = 100$ case with $w_\phi = -0.9$ and $w_\phi = -1.1$ respectively; on the other hand at nonlinear scales there is a enhancement/suppression, proportional to k , which turns to be, at scales $k \sim 10 \text{ h}/\text{Mpc}$, of $\approx 30\%$ in the $\alpha = 100$ case with $w_\phi = -0.9$ and $w_\phi = -1.1$ respectively. In the $\alpha = 10$ case we only found a deviation at nonlinear scales, which however is significantly lower: $\approx 3\%$ at $k \sim 10 \text{ h}/\text{Mpc}$. In the $\alpha = 1$ case no significant deviations are detected. We continued our analysis in section 5.2 by considering the halo mass function of our simulations in the range

$10^{12} - 10^{14} M_{\odot}/h$. Considering the ratio at $z = 0$ between the scattering cases and the non scattering case, we found an enhancement/suppression respectively for the cases $w_{\phi} = -0.9$ and $w_{\phi} = -1.1$; this is $\approx 10 - 15\%$ in the $\alpha = 100$ case and $\approx 1 - 2\%$ in the $\alpha = 10$ case; again, no significant deviations are found when $\alpha = 1$. In section 5.4 we inspected the radial density profiles of the halos at $z = 0$ by considering both profiles of single halos and stacked profiles. In this case we only found significant effects for $\alpha = 100$. We observed that DE-baryon scattering has opposite effects on the inner and outer regions of the halos: there is an increase/decrease of inner density and a decrease/increase of the outer density respectively in the $w_{\phi} = -0.9$ and $w_{\phi} = -1.1$ cases; the transition between the two effects take place at $\approx 0.5R_{200}$ in every mass range under consideration. We found that the deviations in the baryonic matter profiles were significantly larger than the ones in the CDM profiles. In section 5.5, we concluded our analysis by considering the baryon fraction radial profiles of the halos. We found that for $\alpha = 100$ there is a significant deviation from the non scattering case: when $w_{\phi} = -0.9$ the baryon fraction is enhanced with a deviation peak of $\approx 100\%$ and features a trend that decreases with radius; when $w_{\phi} = -1.1$ there is a maximum suppression of $\approx 50\%$ and a growing trend with radius. For $\alpha = 10$ the deviation is milder and more uniform: we saw a $\approx 5\%$ enhancement/suppression respectively for the $w_{\phi} = -0.9$ and $w_{\phi} = -1.1$ cases. For $\alpha = 0$ we did not notice any significant deviation.

The results of this work represent an important step toward the answer to the question posed in [64], namely: "Do we have any hope of detecting scattering between dark energy and baryons through cosmology?". This is indeed the first time in the literature in which the nonlinear effects of DE-baryon scattering are identified in some major cosmological observables. We have seen that the impact of the interaction on these observables becomes significant when $\alpha \approx 10$, i.e. when $\sigma_b \approx 10\sigma_T$. From this approximate value for the cross section, the nonlinear effects start to become stronger than the linear ones. Combined with future observations, these results, as well as the ones of our future works, will help us to put some solid constraints on the interaction cross section. Moreover we have seen that DE-baryon scattering can strongly impact the baryon fraction profile of the halos, this is expected to significantly alter processes like galaxy formation or AGN feedback, thus providing further means to constrain the interaction. The latter aspect deserves a proper exploration in future works.

6.3 Future Prospects

From the analysis of the cosmological observables performed in this work, the following general conclusion, which is valid both for $w_{\phi} = -0.9$ and $w_{\phi} = -1.1$, can be drawn: for $\alpha = 100$ DE-baryon scattering has a significant impact on the nonlinear matter power spectrum, the halo mass function, the radial density profiles of halos and on their baryon fraction profiles; for $\alpha = 10$ these effects are

remarkably milder, but not negligible; finally, for $\alpha = 1$ no significant effects are detected. This suggests that future works on DE-baryon scattering should focus on the effects in the range $10 \leq \alpha \leq 100$.

The present thesis constitutes a starting point in the investigation of the non-linear effects of DE-baryon scattering. As underlined throughout the text, we have made certain reasonable choices of approximation that simplify this first exploratory work. On the other hand these choices represent limitations that we can overcome in future works. First, we could perform zoom simulations by means of multi-scale initial conditions generated by specific codes (e.g. MUSIC [78]). This would lead us to focus with higher precision on the impact of DE-baryon scattering on the halos inner structure and dynamics. Second, we have seen that DE-baryon scattering models typically come equipped with a screening mechanism that prevents this interaction from being detected at the smallest scales. However this was not included in our modified version of GADGET-3; therefore it would be of particular interest a further development of the code in order to include such screening mechanism. Third, baryons were modeled in the present thesis as a collisionless fluid; this is justified by the fact that in this work we studied the nonlinear effects of DE-baryon scattering for the first time in the literature, so we wanted to put our focus on the effects of the interaction alone. The inclusion of hydrodynamics in the simulations, however, would pave the way to a more realistic treatment of the baryons. In this context it would be of particular interest to simulate and study more specific scenarios such as galaxy formation and mergers in the presence of DE-baryon scattering. Further examples of interest for future developments include the study of how DE-baryon scattering can influence: the cosmic voids and their properties, the observation of the intergalactic medium through the Lyman- α absorption line, the dynamics of bullet-like systems; and even more to come.

Acknowledgements

First of all, I want to thank Prof. Marco Baldi, for having patiently taught and guided me during this work.

I am deeply thankful to Dr. Sunny Vagnozzi and Prof. David Fonseca Mota, for the important contribution to this work and for the very useful conversations.



I thank my parents, among other things for having supported me in the choice of studying astrophysics.

I thank my sister Anna Maria, for having always been by my side, even during this thesis work.

I thank my little brother Flavio, for being born on the day I started writing this thesis, bringing enthusiasm and creativity.

I thank my relatives who passed away, for having inspired me and for having taught me to look at the stars.

I thank my grandparents, my uncles and my cousins-siblings for being of precious comfort for me.

I thank my science-friends: Leo, Antonio, Giuseppe, Matteo M., Matteo E., Gianfranco, Giulia L., Alina and Saverio, for the help during this work.

I thank my friends Alessandro C., Alessandro S., Carolina, Erika, Giorgia, Giulia R., Haydée, Maria Caterina, Nicolò, Roberta, Salvo, Sergio and all the others. Everyone of you has contributed to the success of this work.

Ringraziamenti

Ringrazio innanzitutto il Prof. Marco Baldi, per avermi pazientemente istruito e guidato in questo percorso.

Ringrazio sentitamente il Dr. Sunny Vagnozzi e il Prof. David Fonseca Mota, per il loro fondamentale contributo a questo lavoro e per le proficue conversazioni.



Ringrazio i miei genitori, tra le tante altre cose per avermi sostenuto nella scelta di intraprendere questo percorso di studi.

Ringrazio mia sorella Anna Maria, grande compagna di avventure, per supportarmi e sopportarmi, anche durante la preparazione di questa tesi.

Ringrazio il mio fratellino Flavio, per essere nato proprio nel giorno in cui ho scritto la prima pagina, portandomi entusiasmo e creatività.

Ringrazio i miei familiari che non ci sono più, per avermi ispirato e per avermi insegnato a guardare lontano.

Ringrazio i miei nonni, gli zii, e i miei cugini-fratelli per essermi stati di prezioso conforto.

Ringrazio gli amici fisici, astrofisici e ingegneri: Leo, Antonio, Giuseppe, Matteo M., Matteo E., Gianfranco, Giulia L., Alina e Saverio per avermi dato utilissimi consigli durante la scrittura.

Ringrazio gli amici Alessandro C., Alessandro S., Carolina, Erika, Giorgia, Giulia R., Haydée, Maria Caterina, Nicolò, Roberta, Salvo, Sergio e tutti gli altri. Ognuno di voi ha contribuito alla riuscita di questo lavoro.

Bibliography

- [1] A. Einstein, *Zur allgemeinen Relativitätstheorie*. Sitzungsberichte der Königlich Preußischen Akademie der Wissenschaften (Berlin), Seite 778-786, 1915.
- [2] E. Hubble, *A relation between distance and radial velocity among extra-galactic nebulae*. Proc. Nat. Acad. Sci. 15, 168-173, 1929.
- [3] I. M. H. Etherington, *On the definition of distance in general relativity*. Philosophical Magazine 7, 15, 761, 1933.
- [4] G. R. Blumenthal et al., *Formation of galaxies and large-scale structure with cold dark matter*. Nature, 311, 517-525, 1984.
- [5] A. R. Liddle, *Cosmological Inflation and Large-Scale Structure*. Cambridge University Press, 2000.
- [6] S. Perlmutter et al., *Measurements of Omega and Lambda from 42 High-Redshift Supernovae*. APJ 517, 565, 1999.
- [7] A. G. Riess et al., *Observational Evidence from Supernovae for an Accelerating Universe and a Cosmological Constant*. Astron. J. 116, 1009, 1998.
- [8] S. Chandrasekhar, *The maximum mass of ideal white dwarfs*. APJ 74, 81, 1931.
- [9] M. Hamuy et al., *The absolute luminosities of the Calan/Tololo Type Ia supernovae*. Astron. J. 112, 2391, 1996.
- [10] D. Huterer, D. L. Shafer, *Dark energy two decades after: Observables, probes, consistency tests*. Rep. Prog. Phys. 81 016901, 2018.
- [11] SDSS Collaboration, *Improved cosmological constraints from a joint analysis of the SDSS-II and SNLS supernova samples*. Astron. Astrophys. 568, A22, 2014.
- [12] BOSS collaboration, *The clustering of galaxies in the completed SDSS-III Baryon Oscillation Spectroscopic Survey: cosmological analysis of the DR12 galaxy sample*. MNRAS, 470:2617-2652, 2017.

- [13] Planck Collaboration, *Planck 2015 results*. *Astron. Astrophys.* 594, A13, 2016.
- [14] Planck Collaboration, *Planck 2018 results*. *Astron. Astrophys.* 641, A6, 2020.
- [15] A. D. Linde, *A new inflationary universe scenario: A possible solution of the horizon, flatness, homogeneity, isotropy and primordial monopole problems*. *Physics Letters B*, 108, 6, 389-393, 1982.
- [16] W. H. Press, P. Schechter, *Formation of Galaxies and Clusters of Galaxies by Self-Similar Gravitational Condensation*. *Astrophys. J.*, 187, 425-438, 1974.
- [17] R. K. Sheth, G. Tormen, *Large scale bias and the peak background split*. *MNRAS* 308:119, 1999.
- [18] A. Jenkins, *Mass function of dark matter halos*. *MNRAS* 321:372, 2001.
- [19] F. Zwicky, *On the Masses of Nebulae and of Clusters of Nebulae*. *APJ* 86, 217, 1937.
- [20] V. Rubin, W. Ford. *Rotation of the Andromeda Nebula from a Spectroscopic Survey of Emission Regions*. *APJ* 159, 379, 1970.
- [21] M. Davis et al., *The evolution of large-scale structure in a universe dominated by cold dark matter*. *APJ* 292, 371-394, 1985.
- [22] J. F. Navarro, C. Frenk, S. White, *A Universal Density Profile from Hierarchical Clustering*. *APJ* 490, 493-508, 1997.
- [23] J. Einasto, *On the Construction of a Composite Model for the Galaxy and on the Determination of the System of Galactic Parameters*. *Trudy Astrofizicheskogo Instituta Alma-Ata*, 5, 87:100, 1965.
- [24] A. Dutton, A. Macciò, *Cold dark matter haloes in the Planck era: evolution of structural parameters for Einasto and NFW profiles*. *MNRAS* 441:3359-3374, 2014.
- [25] S. D. Reed, *The halo mass function from the dark ages through the present day*. *MNRAS* 374:2-15, 2007.
- [26] N. MacCrann et al., *Cosmic Discordance: Are Planck CMB and CFHTLenS weak lensing measurements out of tune?*. arXiv:1408.4742, 2014.
- [27] V. Poulin et al., *Early Dark Energy Can Resolve The Hubble Tension*. *Phys. Rev. Lett.* 122, 221301, 2019.
- [28] W. L. Freedman, *Cosmology at Crossroads: Tension with the Hubble Constant*. *Nature Astronomy*, 1, 0169, 2017.

- [29] S. W. Hawking, *The cosmological constant is probably zero*. Phys. Lett. B 134, 403, 1984.
- [30] S. Kachru et al., *Self-tuning flat domain walls in 5d gravity and string theory*. Phys. Rev. D62:045021, 2000.
- [31] S.-H. H. Tye, I. Wasserman, *A Brane World Solution to the Cosmological Constant Problem*. Phys. Rev. Lett. 86, 1682-1685, 2001.
- [32] A. Linde, *A brief history of the multiverse*. Rep. Prog. Phys. 80 022001, 2017.
- [33] M. Chevallier, D. Polarski, *Accelerating Universes with Scaling Dark Matter*. Int. J. Mod. Phys. D10:213-224, 2001.
- [34] E. V. Linder, *Exploring the Expansion History of the Universe*. Phys. Rev. Lett. 90:091301, 2003.
- [35] P. Meszaros, *The behaviour of point masses in an expanding cosmological substratum*. Astron. Astrophys. 37, 2, 225:228., 1974.
- [36] L. Amendola, S. Tsujikawa, *Dark Energy: Theory and Observations*. Cambridge University Press, 2010.
- [37] P. Ratra, L. Peebles, *Cosmological consequences of a rolling homogeneous scalar field*. Phys. Rev. D 37, 3406, 1988.
- [38] C. Wetterich, *Cosmology and the Fate of Dilatation Symmetry*. Nucl. Phys., B302:668, 1988.
- [39] R. R. Caldwell, Eric V. Linder, *The Limits of Quintessence*. Phys. Rev. Lett. 95:141301, 2005.
- [40] P. Binetruy, *Models of dynamical supersymmetry breaking and quintessence*. Phys. Rev. D 60, 063502, 1999.
- [41] P. Brax, J. Martin, *Quintessence and Supergravity*. Phys. Lett. B468, 40-45, 1999.
- [42] A. Linde, *Inflation and quantum cosmology*, in *Three Hundred Years of Gravitation*. Eds. S. W. Hawking and W. Israel, Cambridge University Press, 604, 1987.
- [43] J. Frieman et al., *Cosmology with Ultra-light Pseudo-Nambu-Goldstone Bosons*. Phys. Rev. Lett. 75:2077-2080, 1995.
- [44] R. R. Caldwell, *A Phantom Menace? Cosmological consequences of a dark energy component with super-negative equation of state*. Phys. Lett. B545, 23-29, 2002.

- [45] S. M. Carroll et al., *Can the dark energy equation-of-state parameter w be less than -1 ?* Phys. Rev. D 68, 023509, 2003.
- [46] P. Singh et al., *Cosmological dynamics of a phantom field.* Phys. Rev. D 68, 023522, 2003.
- [47] M. Sami, A. Toporensky, *Phantom Field and the Fate of Universe.* Mod. Phys. Lett. A19:1509, 2004.
- [48] J. M. Cline et al., *The Phantom menaced: Constraints on low-energy effective ghosts.* Phys. Rev. D 70, 043543, 2004.
- [49] R. R. Caldwell et al., *Phantom Energy and Cosmic Doomsday.* Phys. Rev. Lett. 91, 071301 2003.
- [50] S. M. Carroll, *Quintessence and the Rest of the World: Suppressing Long-Range Interactions.* Phys. Rev. D 61, 3067, 1998.
- [51] T. Damour et al., *Dark matter, time-varying G , and a dilaton field.* Phys. Rev. Lett. 64, 123, 1990.
- [52] L. Amendola, *Scaling solutions in general nonminimal coupling theories.* Phys. Rev. D 60, 043501, 1999.
- [53] L. Amendola, *Coupled Quintessence.* Phys. Rev. D 62, 043511, 2000.
- [54] L. Amendola, *Linear and non-linear perturbations in dark energy models.* Phys. Rev. D 69, 103524, 2004.
- [55] C. Wetterich, *The cosmon model for an asymptotically vanishing time-dependent cosmological constant.* Astron. Astrophys. 301, 321-328, 1995.
- [56] R. K. Sachs; A. M. Wolfe, *Perturbations of a Cosmological Model and Angular Variations of the Microwave Background.* APJ 147, 73, 1967.
- [57] M. Baldi, *Hydrodynamical N -body simulations of coupled dark energy cosmologies.* MNRAS 403:1684-1702, 2010
- [58] M. Baldi, *Time dependent couplings in the dark sector: from background evolution to nonlinear structure formation.* MNRAS 411:1077, 2011.
- [59] M. Baldi, *Clarifying the effects of interacting dark energy on linear and non-linear structure formation processes.* MNRAS 414:116, 2011.
- [60] F. Simpson, *Scattering of Dark Matter and Dark Energy.* Phys. Rev. D 82, 083505, 2010.
- [61] M. Baldi, F. Simpson, *Simulating Momentum Exchange in the Dark Sector.* MNRAS 449, 2239–2249, 2015.

- [62] M. Baldi, F. Simpson, *Structure formation simulations with momentum exchange: alleviating tensions between high-redshift and low-redshift cosmological probes*. MNRAS 465, 653–666, 2017.
- [63] T. Padmanaban, *Inverse Compton scattering – revisited*. J Astrophys Astron 18, 87–90, 1997.
- [64] S. Vagnozzi et al., *Do we have any hope of detecting scattering between dark energy and baryons through cosmology?*. MNRAS 493 1139, 2020.
- [65] J. B. Jimenez et al., *On cosmological signatures of baryons-dark energy elastic couplings*. JCAP 08 020, 2020.
- [66] J. Khoury, *Theories of Dark Energy with Screening Mechanisms*. arXiv:1011.5909, 2010.
- [67] A. Lewis et al., *Efficient Computation of Cosmic Microwave Background Anisotropies in Closed Friedmann-Robertson-Walker Models*. APJ 538, 473, 2000.
- [68] V. Springel et al., *GADGET: A code for collisionless and gasdynamical cosmological simulations*. New Astron. 6:79, 2001.
- [69] V. Springel et al., *Populating a cluster of galaxies - I. Results at $z=0$* . MNRAS 328:726, 2001.
- [70] V. Springel, *The cosmological simulation code GADGET-2*. MNRAS 364 1105-1134, 2005.
- [71] A. W. Appel, *An Efficient Program for Many-Body Simulation*. SIAM, J. Sci. Stat. Comp, 6, 85, 1985.
- [72] J. Barnes, P. Hut, *A hierarchical $O(N \log N)$ force-calculation algorithm*. Nature 324, 446–449, 1986.
- [73] G. Xu, *A New Parallel N -Body Gravity Solver: TPM*. APJ 98, 355, 1985.
- [74] M. Frigo, S. G. Johnson, *FFTW: an adaptive software architecture for the FFT*. ICASSP, 3, 1381–1384, 1998.
- [75] V. Springel, *N -GenIC: Cosmological structure initial conditions*. Astrophysics Source Code Library 1502.003, 2015.
- [76] Y. B. Zel'Dovich, *Gravitational instability: An approximate theory for large density perturbations*. Astron. Astrophys., 5, 84, 1970.
- [77] F. Villaescusa-Navarro, *Pylians: Python libraries for the analysis of numerical simulations*. Astrophysics Source Code Library, 1811.008, 2018.
- [78] O. Hahn, T. Abel, *Multi-scale initial conditions for cosmological simulations*. MNRAS 415 2101-2121, 2011.